The OctoWalker

Design and evaluation of a closed-chain
electric powered walking wheelchair for
low- and middle-income countries

Anne Marianne Brinkman
Master Thesis
January 2023

TUDelft

The OctoWalker

Design and evaluation of a closed-chain electric powered walking wheelchair for low- and middle-income countries

Master Graduation Thesis

BioMechanical Design, Bio Inspired Technology

Department of Biomechanical Engineering

Delft University of Technology

Thesis committee

Dr.ir. G. Smit (supervisor)

Prof.dr. H. Vallery

Dr.ir. T. Horeman

Dr.ing. L. Marchal Crespo

Author

Anne Marianne Brinkman

Student number: 4679237

January 17, 2023

TUDelft Delft University of Technology

Preface

This thesis "The OctoWalker - Design and evaluation of a closed-chain electric powered walking wheelchair for low- and middle-income countries." represents the end of my master studies in Mechanical Engineering at Delft University of Technology. From an early age I have always dreamed of becoming an engineer. One of my first primary school projects I still remember were a gearbox made of cardboard and a carousal made of marbles and little toys. Now, 15 years later, I am finalizing my master thesis and starting to get a bit emotional, thinking about how much I have learned and grown in these past years. It has not always been an easy journey with many ups and downs, but without the support of all my family and friends it would not have been possible. I would like to thank my supervisor, Dr.ir. Gerwin Smit, for his guidance and support during the process. Thank you Mark for being my daily proofreader and always made sure I did not overwork myself. Finally, a special thanks to my parents, Thum Yen Loo and Gianfranco Giuliano Brinkman. Thank you mama for always mentally supporting me, advising me and making sure I always ate and slept enough. Thank you papa for assisting me during the designing and building phase of my prototype, even when you were still recovering from your surgery. Thank you both for always supporting me in everything I do, you are my biggest inspirations in life ♥.

Anne Brinkman
The Hague, January 2023

Contents

The OctoWalker - Design and evaluation of a closed-chain electric powered walking wheelchair for low- and middle-income countries

Anne Marianne Brinkman

Abstract

Background: The lack of access to electric powered wheelchairs for disabled people in low- and middle-income countries, that suit their rural environments, still remains an issue. Current available electric powered wheelchairs that do adapt to these rural environments are expensive and require complex control algorithms.

Objective: The aim of this research is to analyze the feasibility of an electric powered walking wheelchair with an one-degree-of-freedom closed-chain leg mechanism. The electric powered walking wheelchair should provide a solution for low-cost transportation for human adults with lower and upper extremity impairments in the poor road conditions of low- and middle-income countries. A scaled prototype will be designed, build and evaluated with the purpose that it lays the groundwork for future renditions in a true-scaled electric powered walking wheelchair.

Methods: Design requirements were formulated according to the ISO-7176 standards for wheelchairs and conceptual designs were generated, in which a final concept was selected according to the performance criteria. A final design was build and different tests were executed to evaluate the technical specifications and feasibility of the walking wheelchair.

Results: This resulted in the OctoWalker, an 1:3 scaled eight-legged walking wheelchair with a modified Trotbot leg mechanism, two DC motors, timing belt transmission, joystick control and electronic differential. The OctoWalker was able to walk on flat surfaces; steer to the left and right; climb over curb heights of 50 mm; and climb slopes up to 28° without the need of additional sensors and control features to maintain its stability.

Conclusion: The evaluation showed that a true-scaled OctoWalker would have a larger payload (135 kg), step length (675 mm) and speed (4.75 km/h) than currently existing leg-based electric powered wheelchairs. In future studies, improvements for a true-scaled OctoWalker are required in terms of travel range (2.5 km), wheelchair width (789 mm) and weight (140 kg), in order to achieve similar specifications as current stair-climbing and obstacle avoidance electric powered wheelchairs. Nonetheless, the OctoWalker opens up future opportunities for providing low-cost transportation for disabled people in low- and middle-income countries.

1   Introduction
1.1   Background
1.1.1   Disability and poverty

Globally, more than one billion people are living with some form of disability, of which 131.8 million people require a wheelchair [1-3]. According to the United Nations (UN), 92% of these persons with disabilities live below the poverty line in low- and middle-income countries (LMICs), such as Sierra Leone, Kenya and India; while only 10% of disabled people have access to a wheelchair [2, 4, 5]. The lack of appropriate wheelchairs remains a frequent reason for a disabled person to not participate in society (e.g. work and education) [4, 6]. This especially occurs in LMICs, in which basic infrastructure is limited; and the majority of the population live in rural areas with uneven roads, hills, muddy tracks and sand [7, 8]. UNESCO estimated that 90% of children with disabilities in LMICs do not attend school as a result of these environmental barriers [4]. Additionally, factors including inadequate policies and standards, negative attitudes and discrimination towards disabled people, lack of health care services and lack of economical means; also create barriers to participation and inclusion [3]. This does not only affect persons with disabilities, but also their families and the community. It is therefore commonly understood that people with disabilities are more likely to become poor and living in poverty will more likely increase the risk of disability [9, 10], which is described as the vicious circle of poverty and disability (Figure 1.1).

1.1.2   Electric powered wheelchairs

Electric powered wheelchairs (EPWs) provide mobility for people with both lower and upper extremity impairments [11]. In the 1950s the first commercially produced EPW had twin internal motors, four wheels and a joystick to control the vehicle. From the 1970s further development of controllers allowed to improve the drivability and safety of EPWs, in which different control techniques and algorithms were researched and applied [12]. However, until this day the use of EPWs in outdoor environments still remains an issue (e.g. uneven or sloping terrains), especially if people are severely physically or mentally impaired [13]. Therefore, different EPWs have been developed with additional stair climbing and obstacle avoidance features, such as track

Figure 1.1: The vicious circle of poverty and disability. An impairment can result in discrimination and disability, which causes exclusion of the community, poverty, further exclusion and subsequently the risk of further impairment [9,10].

based, wheel-cluster based, leg based and hybrid EPWs (Figure 1.2) [11, 13].

Track-based EPWs use caterpillar tracks with teeth to climb up or down the stairs at constant speed, which is the most applied stair climbing EPW. The TopChair-S is an example of a typical track-based EPW and is known for its comfort and maneuverability (Figure 1.2a) [14]. Wheel cluster-based EPWs consist of multiple wheels that are distributed in the same plane around a common center. Wheel clusters typically have two to four wheels in a cluster, for example the iBOT, which has two wheels per cluster (Figure 1.2b) [15]. Leg-based EPWs imitate the stair-climbing techniques of humans and animals by using legs and feet; for example the Toyota I-foot, which has two legs and an additional feedback controller to achieve stable walking (Figure 1.2c) [16]. Hybrid stair-climbing EPWs use a combination of wheels and a deformation mechanism at the chassis, allowing it to surpass obstacles with different geometries (Figure 1.2d) [17].

1.1.3 Closed-chain mechanisms

A Kinematic chain is a combination of links with nodes that are connected as joints to supply an input motion, which results in a controlled output motion response [18]. Examples of different types of links include binary links with two nodes, ternary links with three nodes and quaternary links with four nodes. Kinematic chains are either closed or open. A closed-chain mechanism is a connection of multiple links in a closed-loop with revolute joints, which results in one degree-of-freedom (1DOF) (Figure 1.3a). On the contrary, an open chain mechanism will always have more than 1DOF (Figure 1.3b). The mobility of a kinematic chain can be determined with Grübler's equation [19]:

$$M = 3L - 2J - 3G,$$ (1.1)

where M, L, J and G represent the degree of freedom or

(a) Track-based   (b) Wheel cluster-based

(c) Leg-based   (d) Hybrid

Figure 1.2: Examples of stair-climbing electric powered wheelchairs (EPWs) include (a) the track-based EPW of TopChair-S [14]; (b) the wheel cluster-based EPW of iBOT [15]; (c) the leg-based EPW of Toyota I-foot [16]; and (d) the hybrid EPW of Chocoteco et al. (2015) [17].
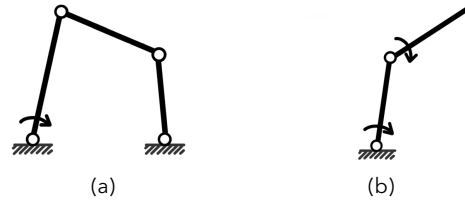
Figure 1.3: Kinematic mechanisms are divided into (a) closed-chain mechanisms and (b) open-chain mechanisms. A closed-chain mechanism always results in one degree-of-freedom (1DOF), while open-chain mechanisms can have multiple degrees-of-freedom [18].

mobility, number of links, number of joints and the number of grounded links, respectively. When considering a single closed-chain mechanism with planar linkages, each joint should have one degree of freedom ($M = 1$, $G = 1$) [20]. This results in the equation:

$$J = \frac{3}{2}L - 2,$$ (1.2)

in which the number of joints of a planar closed-chain mechanism can be determined, with the condition that the number of links (L) must always be an even number. The number synthesis determines the number and type of link sets that are required to produce a motion of a particular DOF (e.g., binary, ternary, quaternary, etc.). In Table 1.1 an overview is shown of the possible link sets for an 1DOF planar mechanism with revolute joints up to eight links [18]. Furthermore, the connection order of each link set determines the motion properties of a kinematic chain, which is defined as linkage isomer. In Table 1.2 an overview is shown of the number of valid isomers found for 1DOF mechanisms with revolute joints up to 12 links. This means that there are many possible closed-chain mechanisms with different motion properties, in which the exact number is still unknown [21, 22].

Table 1.1: Overview of the possible link sets for an 1DOF planar mechanism with revolute joints up to eight links [18]. The four-bar mechanism has only one possible configuration, six-bar mechanisms have two configurations and eight-bar mechanisms have five possible configurations.

# Links	4	6	6	8	8	8	8	8
Binary	4	4	5	7	4	5	6	6
Ternary	0	2	0	0	4	2	0	1
Quaternary	0	0	1	0	0	1	2	0
Pentagonal	0	0	0	0	0	0	0	1
Hexagonal	0	0	0	1	0	0	0	0

Table 1.2: Overview of the number of valid isomers found for 1DOF mechanisms with revolute joints for four-, six-, eight-, ten- and 12-bar mechanisms.

# Links	4	6	8	10	12
Valid isomers	1	2	16	230	6856

1.2 Problem definition

The lack of access to transportation for disabled people still remains an issue in LMICs, which can cause decreased activity levels and social participation [23, 24]. A large number of wheelchairs in these countries, donated by the international community, are rejected since they do not suit the user and their rural environments, such as sandy areas, muddy tracks, gravel, pot-holed roads, high curbs, narrow streets and hills [3, 7, 25-27]. Current commercially available EPWs, that do include these stair-climbing and

obstacle avoidance abilities, require complex control algorithms in order to maintain its balance and being able to adapt to its environment [28, 29]. These EPWs are expensive, with a starting price of € 15,000 for the TopChair-S [14] and € 30,000 for the iBOT [30], making it not suitable for LMICs. The solution of using a closed-chain leg-based EPW, in order to reduce its control complexity and costs, has already been proposed by de Britto et al. (2012) [31]. However, to the author's knowledge, limited research has been conducted on the specific design guidelines of closed-chain leg-based EPWs; and no closed-chain leg-based EPW prototype has been designed and build so far, to analyze its feasibility, stability and adaptability.

1.3 Research objective
The aim of this research is to analyze the feasibility of an electric powered walking wheelchair (EPWW) with a closed-chain leg mechanism for human adults with lower and upper extremity impairments in low- and middle-income countries (LMICs). The EPWW should provide transportation in the poor road conditions of rural areas in LMICs, in order to minimize the control complexity and costs with respect to state of the art electric powered wheelchairs (EPWs). A low-cost scaled prototype will be designed and build according to the ISO-7176 standards for wheelchairs [32], with the purpose that it lays the groundwork for future renditions in a real world scaled EPWW. The performance and viability of the prototype will be evaluated, in order to conduct specific design guidelines for a true-scaled EPWW.

1.4 Research approach
This research will focus on designing and evaluating a scaled EPWW. In the next section (2), the design requirements are formulated, which are categorized in functional requirements, specifications, constraints and performance criteria. The conceptual design process is explained in section 3, which discusses the concept generation and concept selection of the leg mechanism, steering mechanism, differential mechanism, transmission mechanism and actuators, resulting in a final concept. Section 4 and 5 will cover the final design and explain in detail the building process of the prototype; and section 6 describes different evaluation methods and results of the EPWW. A discussion of the EPWW will be given about the scalability and limitations of the EPWW in section 7. Finally, recommendations and a conclusion will be provided in section 8 and 9.

2 Design requirements
2.1 Functional requirements
The functional requirements are the basic requirements in which an EPWW must meet [33]. These requirements are solution independent, which are the core requirements of this project and the future true-scaled EPWW. In Table 2.1 an overview of the general functional requirements are defined.

2.2 Specifications
The specifications describe the design decisions, which have been made at the start of this research, before the concepts were generated (section 3). Since only the

Table 2.1: Overview of the general functional requirements of an EPWW. Each requirement includes a requirement identification (ID) and the requirement itself.

ID	Functional requirement
FR1	The EPWW must provide transportation for human adults with lower extremity, upper extremity and/or sensory-motor impairments in LMICs, for example due to a stroke, cerebral palsy, polio or spinal cord injury [7, 28, 34].
FR2	The EPWW must be able to walk forward and backward.
FR3	The EPWW must be able to accelerate and decelerate.
FR4	The EPWW must be able to steer to the left and right.
FR5	The EPWW must be able to walk outdoors over unstructured surfaces, including high curbs, hills, grass, gravel, stones and pot-holed roads, which fits within the context of rural areas in LMICs [27-29].

feasibility will be analyzed and no user testing will be done, the EPWW will be a scaled model. A large scale (e.g. 1:2) would require more expensive components, while a smaller scale (e.g. 1:4) would require more advanced attachment principles, therefore an 1:3 scale was chosen. For stability purposes a minimum of eight legs is recommended, such that there will always be a minimum of four feet on the ground [35]. However, increasing the number of legs will increase the size and costs of the EPWW, therefore the EPWW must consist of only eight legs. In Table 2.2 an overview of all the specifications are defined.

Table 2.2: Overview of the specifications of an EPWW. Each requirement includes a requirement identification (ID) and the requirement itself.

ID	Specifications
S1	In order to analyze the feasibility of an EPWW, the prototype will be scaled to an 1:3 model.
S2	For stability purposes, while still minimizing the size and costs, the EPWW must consist of eight legs [35].
S3	The legs of the EPWW must consist of an 1DOF closed-chain walking mechanism, which limits the amount of actuators per leg to a maximum of one; and therefore also minimizes the costs and control complexity [36, 37].
S4	The EPWW must be controlled, such that the user can steer to all four directions (FR2, FR3) by a single hand.
S5	The EPWW must be made of existing, easily available components and/or manufacturing techniques, such as additive manufacturing and laser cutting [38].
S6	The EPWW must consist of components that are easily assembled and replaced when necessary.
S7	Protection shields must be placed for a safe and secure system for the user, which also prevents fast corrosion for outdoor use [39].

2.3 Constraints
The constraints describe the quantitative limitations of the 1:3 scaled design (S1), which are divided into general constraints (2.3.1), dimensional constraints (2.3.2) and leg constraints (2.3.3). In Appendix A an overview of the constraints and scaling factors of a true-scaled EPWW are defined.

2.3.1 General constraints
In order to prevent the user from tripping over unstructured surfaces, the EPWW is not allowed to run. The maximum speed of electric powered wheelchairs (EPW) for indoor and/or outdoor mobility allowed for the ISO-7176-1 norms is 4.2 m/s (15 km/h) [40]; while a walking speed between 0.9-1.2 m/s (3.2-4.3 km/h) is preferred among human adults [41]. Geyer et al. (2006) explains that humans walk up

to 1.8 m/s, and spontaneously start running at 2.3 m/s [42]. Therefore, the maximum speed of a full scaled EPWW cannot exceed 1.8 m/s (6.5 km/h); and an 1:3 scaled EPWW cannot exceed 0.6 m/s (2.2 km/h). The average weight of human adults varies by nations, from 57.7 kg in Asia and Africa to about 80.7 kg in North America [43]. This corresponds with a maximum allowed payload of 100 kg for a full scaled EPWW for the ISO-7176-11 norms; and a 3.7 kg payload for an 1:3 scaled EPWW [44]. According to the ISO-7176-5 norms the turning radius of an EPW cannot be larger than 2800 mm, which allows for a smaller maneuvering space in small, narrow and crowded places [45, 46]. Therefore, the 1:3 scaled turning radius cannot be larger than 933 mm. The EPWW should use a lead acid battery with a maximum output voltage of 36 V (ISO-7176-25 norm) [40, 47]. The use of other batteries, such as nickel and lithium based batteries, are also possible. However, lead acid batteries are preferred, due to its safety advantages for the end-user [48]. This also limits the use of actuators to only DC motors, since batteries only provide DC currents [49]. In Table 2.3 an overview of the general constraints for an 1:3 scaled EPWW are defined.

Table 2.3: Overview of the general constraints for an 1:3 scaled EPWW. Each requirement includes a requirement identification (ID) and the requirement itself.

ID	General constraints
C1	The maximum **speed** of the EPWW cannot exceed 0.6 m/s (2.2 km/h) [42].
C2	The EPWW must transport **payloads** up to 3.7 kg (ISO-7176-11).
C3	The **turning radius** cannot be larger than 933 mm (ISO-7176-5).
C4	The EPWW must use a lead acid **battery** with a nominal **voltage** not greater than 36 V (ISO-7176-25).
C4-1	The EPWW must use DC motors, since lead acid batteries provide only a DC current [49].

2.3.2   Dimensional constraints
The dimensional constraints of the overall EPWW and wheelchair seat were defined according to the ISO-7176-5 standards for wheelchairs (Figure 2.1) [45, 46]. The dimensional constraints allow for easy access in building entrances, enough maneuvering space for the EPWW and
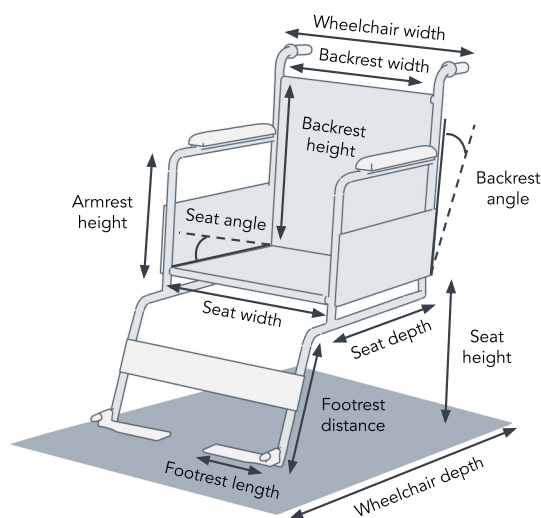
Figure 2.1: Overview of the different components of a wheelchair seat, consisting of a seat, a backrest, armrests and footrests. The dimensions of the different components are constrained by the dimensional constraints in Table 2.4.

comfortable seating according to the average anatomical dimensions of human adults [40, 50, 51]. In Table 2.4 an overview of the dimensional constraints for an 1:3 scaled EPWW are defined.

Table 2.4: Overview of the dimensional constraints for an 1:3 scaled EPWW. Each requirement includes a requirement identification (ID) and the requirement itself. All the dimensional constraints are according to the ISO-7176-5 standards, determination of dimensions, mass and maneuvering space [40, 45, 46, 50, 51].

ID	Dimensional constraints
C5	The maximum **wheelchair width** must be 233 mm.
C6	The maximum **wheelchair depth** must be 433 mm.
C7	The maximum **seat height** must be 173 mm.
C8	The maximum **seat depth** must be 150 mm.
C9	The maximum **seat width** must be 150 mm.
C10	The maximum inclination of the **seat angle** must be 4°.
C11	The maximum **armrest height** must be 67 mm.
C12	The maximum **backrest height** must be 140 mm.
C13	The maximum **backrest width** must be 150 mm
C14	The **backrest angle** must be between 100°-110°.
C15	The minimum **distance** of the **footrest to seat** must be 13 mm.
C16	The maximum **distance** of the **footrest to seat** must be 150 mm.
C17	The maximum **footrest length** must be 83 mm.

2.3.3   Leg constraints
In order to determine the leg constraints (Table 2.5), the dimensions of curbs and shallow stairs were analyzed. Normal sized curbs can range between 40 mm up to 150 mm [52-55]; while shallow stairs have a riser height between 127 mm to 150 mm (Figure 2.2) [56-59]. When considering the highest curb height and riser height of shallow stairs, the minimum step height of a full scaled leg must be 150 mm. Therefore, an 1:3 scaled leg must have a minimum step height of 50 mm. Furthermore, shallow stairs can have a run length ranging from 280 mm up to 419 mm, which results in scaled run lengths from 92 mm to 140 mm (Figure 2.2) [56-59]. A larger step is considered more efficient for a faster walking speed. When looking at the smallest climbing slope, the step length must be 140 mm, which results in a minimum slope of 20°. When looking at the largest climbing slope, the step length must be 93 mm, which results in a maximum slope of 28°.

Table 2.5: Overview of the leg constraints for an 1:3 scaled EPWW. Each requirement includes a requirement identification (ID) and the requirement itself.

ID	Leg constraints
C18	The minimum **step height** must be 50 mm.
C19	The minimum **step length** must be 93 mm.
C20	The minimum **climbing slope** must be 20°.
C21	The maximum **climbing slope** must be 28°.

2.4   Performance criteria
The performance criteria were used to grade the concepts of the EPWW, as described in section 3. The different criteria are divided into general criteria (2.4.1), leg mechanism criteria (2.4.2) and steering and control criteria (2.4.3).

2.4.1   General criteria
In order to fit within the context of LMICs, the total costs of the EPWW should also be minimized. This includes the costs of the materials, manufacturing and maintenance. The
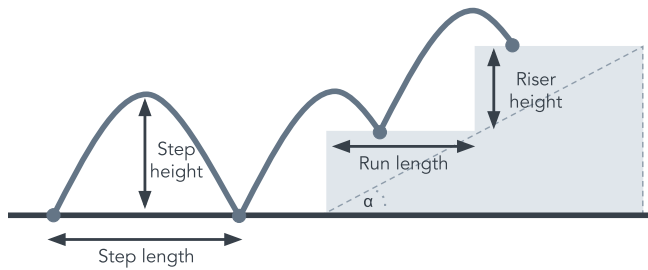
Figure 2.2: The run length and riser height of a shallow stair influences the maximum step length and minimum step height of the EPWW.

total stability of the EPWW should be maximized, which means that the center of gravity should be as close to the ground as possible; and the vertical fluctuations experienced by the user should also be minimized. Furthermore, the total size of the EPWW should be minimized. This includes the space that would be occupied by the different mechanisms, such that the dimensional constraints are satisfied (2.3.2).

2.4.2 Leg mechanism criteria
The leg mechanism should be as simple as possible, this means that the number of links and joints should be minimized. This decrease of the number of components results in a decrease of the material, manufacturing and maintenance costs of the leg mechanism. The stability should be maximized, this means that the speed should be as uniform as possible to avoid bouncing and consuming power from constantly accelerating and decelerating the wheelchair [60]. The space that would be occupied by the leg mechanism should be minimized by minimizing the wheelchair width and depth. The seat height should be maximized, however with the center of gravity as close to the ground as possible for a higher climbing slope and stability. The overall footpath design should be maximized for avoiding large obstacles and allowing for faster travel speed. For avoiding large obstacles and walking on unstructured surfaces and hills, a larger maximum climbing slope is preferred. Therefore, the maximum climbing slope should be maximized. Additionally, the leg mechanism should be able to perform the same in different environments, such that it fits within the context of LMICs (FR5). In Table 2.6 an overview of the leg mechanism criteria are defined.

2.4.3 Steering and control criteria
The costs of the steering mechanism, including the actuators and the number of components, should be minimized in order to fit within the context of LMICs [9, 10]. The mass and size of the chassis should be minimized, which relates to the steering mechanism and actuators that are placed on it. This reduces the required motor torque, and therefore also the costs for the actuators. The number of actuators per leg should also be minimized. This would also minimize the design complexity and costs. The maneuverability while steering should be maximized, which is important for walking in narrow streets and avoiding unexpected obstacles. This means that the minimum turning radius of the EPWW should be minimized. The number of steps performed by the user for controlling the EPWW should be minimized, such that the user can change

the direction and speed of the EPWW as fast as possible in case of an emergency. In Table 2.7 an overview of the steering and control criteria are defined.

Table 2.6: Overview of the leg mechanism criteria for the EPWW. Each criteria includes a criteria identification (ID) and the criteria itself, which were used to grade different concepts (section 3).

ID	Criteria
PC1-1	The costs of the leg mechanism should be minimized by decreasing the **design complexity** (number of components).
PC2	The stability of the leg mechanism should be maximized by minimizing the **speed fluctuations** in the foot trajectory [60].
PC3-1	The **space** that will be occupied by the leg mechanism should be minimized.
PC4	The maximum **step height-to-crank radius ratio** should be maximized for obstacle avoidance.
PC5	The maximum **step length-to-crank radius ratio** should be maximized for faster travel speed.
PC6	The **footpath design** should be maximized, which is the step height-to-step length ratio.
PC7	The maximum **climbing slope** should be maximized.
PC8	The **adaptability** of the leg mechanism in different environments should be maximized.

Table 2.7: Overview of the steering and control criteria for the EPWW. Each criteria includes a criteria identification (ID) and the criteria itself, which were used to grade different concepts (section 3).

ID	Criteria
PC1-2	The **costs** of the steering and control mechanism should be minimized.
PC3-2	The **space and mass** of the chassis should be minimized with respect to the other components of the EPWW, such that the required actuator torque and costs will be minimized.
PC9	The actuator-to-leg-ratio (**AL-ratio**) of the EPWW should be minimized.
PC10	The minimum **turning radius** of the EPWW should be minimized.
PC11	The number of steps performed to **control** the EPWW by the **user** should be minimized.

3 Conceptual design
3.1 Concept generation
3.1.1 Leg mechanism
1DOF closed-chain planar mechanisms can be categorized by the number of links. A four-bar mechanism always has four joints and one isomer. Examples of four-bar mechanisms, include the straight-line mechanisms of Evans [61], Chebyshev [20] and Hoecken [18], which all have similar half circular foot trajectories (Figure 3.1). According to Grübler's equation, six-bar mechanisms have seven joints and two isomers, which are Watt's and Stephenson's chain [18, 19, 20]. The Klann's linkage is a spider inspired walking mechanism derived from the Stephenson's chain [62]. Eight-bar mechanisms consist of ten joints and 16 isomers (e.g. Jansen's linkage [63]); and ten-bar mechanisms consist of 13 joints and 230 isomers (e.g. Strider's [64] and Trotbot's linkage [65]). Strider's linkage is actually a combination of two four-bar mechanisms, in which the front and hind legs are connected by a single main crank. Trotbot's linkage consist of two "feet" per leg, the toe and heel, which extends the foot trajectory. Other walking mechanisms (e.g. Ghassei's linkage) are derivations of these main leg mechanisms [66].

In Figure 3.2 an overview of the main six- , eight- and ten-bar leg mechanisms is shown. The locus or foot trajectory of the foot should ideally have a straight stride, moving at a constant velocity [67]. This will result in a stable EPWW, in which the vertical fluctuations are minimized (PC2). Therefore, the four-bar mechanisms with a half circular locus were eliminated first. In Table 3.1 an overview is shown of the properties of the remaining leg mechanisms.

3.1.2 Steering mechanism

In robotics, an electronic differential is usually applied as steering mechanism, which requires two continuous rotational motors that can rotate at different speeds with respect to each other [69]. In order to steer to the left or right, the motor has to rotate at a different speed with respect to the other motor. Additionally, the electronic differential also allows the EPWW to spin around its own axis (Figure 3.3). Since the steering mechanism is purely electronic, the use of an electronic steering control method is the most suitable combination. Therefore, a two-axis joystick was used for this concept, such that the user can steer to all four directions by a single hand (FR2, FR3). In the automotive industry, different mechanical steering mechanisms are used, which can be applied as front- or four-wheel steering [70]. Similarly, these principles

(a) Evans   (b) Chebyshev   (c) Hoecken

Figure 3.1: Examples of four-bar straight-line mechanisms include (a) Evans' linkage [61], (b) Chebyshev's linkage [20] and (c) Hoecken's linkage [18]. All three mechanisms have similar foot trajectories, since there is only one isomer possible with a four-bar mechanism.

(a) Klann   (b) Jansen

(c) Trotbot   (d) Strider

Figure 3.2: Overview of the main leg mechanisms with (a) Klann's six-bar mechanism [62], (b) Jansen's eight-bar mechanism [63], (c) Trotbot's ten-bar mechanism [65] and (d) Strider's ten-bar mechanism [64], in which Strider's mechanism directly combines the front and hind legs.

can be applied to the legs of the EPWW. In Figure 3.4 an overview is shown of the different main mechanical steering mechanisms.

The Ackermann mechanism is the simplest mechanical steering mechanism, in which a four-bar mechanism is used to rotate the front or rear legs around two fixed pivot joints [71]. The Bell-crank mechanism uses a six-bar mechanism to change the direction of the front or rear legs with an additional fixed pivot joint [70]. A steering gearbox uses different types of gears, cams or rollers to change the direction of the legs. The simplest gearbox steering mechanism is the rack and pinion steering mechanism, in which the rotation of a gear results in a linear translation of a rack and therefore a change in direction of the legs [70]. If the EPWW with a mechanical steering mechanism is steered manually with a handle or steering wheel, no additional actuators will be used for the steering. This limits the number actuators to one or two actuators to regulate the speed of the legs. The user can then control the speed

Table 3.1: Overview of the properties of the Klann, Jansen, Trotbot and Strider mechanism, in which each mechanism has a straight stride.

	Klann [62]	Jansen [63]	Trotbot [65]	Strider [64]
Links/leg	6	8	10	10
Joints/leg	7	10	13	13
Locus shape	Triangular	Triangular	Oval	Oval
Step height-to-step length ratio[1]	0.425	0.321	0.333	0.234
Step height-to-crank radius-ratio[1]	1.67	1.59	1.35	1.14
Step length-to-crank radius-ratio[1]	3.93	4.96	3.93	3.86
Planar crank area[2]	47 m^2	59 m^2	19 m^2	56 m^2
Planar height area[3]	17 m^2	23 m^2	15 m^2	56 m^2
Foot stride speed [60] [4]	0 – 4.5 m/s	2.1 – 4.3 m/s	3.8 – 5.0 m/s	3.4 – 4.0 m/s
Applications [68]	Rugged terrain and obstacle avoidance.	Flat surface and small obstacle avoidance.	Flat surface, rugged terrain and obstacle avoidance.	Flat surface, rugged terrain and obstacle avoidance.

[1]: Maximum step height and step length.
[2]: The planar area of the walking mechanism of one leg at a crank radius of 1 m.
[3]: The planar area of the walking mechanism of one leg at a step height of 1 m.
[4]: Foot speed variation of the locus, in which the leg mechanisms have the same step height.

(a) Forward   (b) Right   (c) Left   (d) Spin
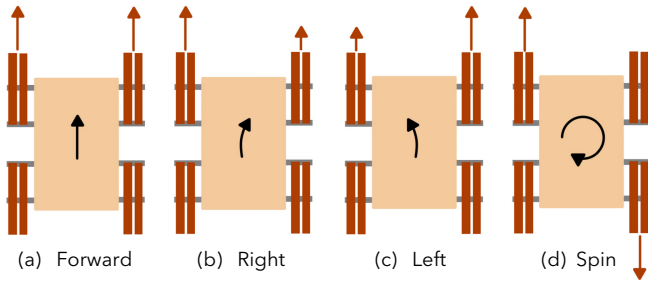
Figure 3.3: Principle of an electronic steering differential. (a) If both, left and right, legs rotate at the same speed, the EPWW moves forward. (b) If the right legs rotate slower with respect to the left legs, the EPWW walks to the right. (c) If the left legs rotate slower with respect to the right legs, the EPWW walks to the left. (d) If both sides rotate at the same speed, but in the opposite direction, the EPWW spins.

(a) Ackermann mechanism   (b) Bell-crank mechanism

(c) Rack-and-pinion mechanism
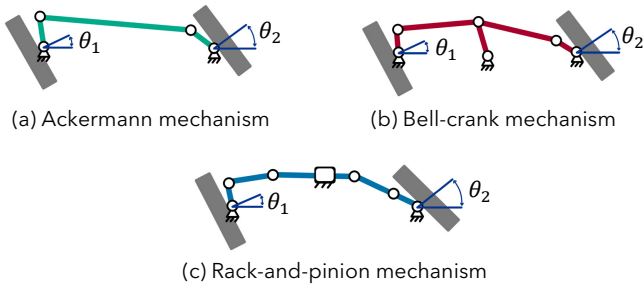
Figure 3.4: The different types of mechanical steering mechanisms, which can be applied as front- or eight-leg steering. (a) The Ackermann mechanism uses a four-bar mechanism [71]; (b) the Bell-crank mechanism uses a six-bar mechanism [70]; and (c) the rack-and-pinion mechanism uses a gear rack to change the direction of the legs [70].

by buttons or an one-axis joystick. If the EPWW with a mechanical steering mechanism will be controlled electronically, an additional actuator will be required for the steering. This results in two or three actuators in total, in which the user controls the speed and direction using a two-axis joystick.

In electronic steering the legs will not mechanically change its direction, but only the speed changes of two actuators influence the direction. Therefore, the minimum steering radius is 0 mm and the maximum rotation angle of the legs is 0°. In mechanical steering mechanisms, the maximum rotation angle of the inner (θ_1) and outer (θ_2) legs

are different, consequently the turning radii will also be different. Furthermore, the use of front- or eight-leg steering also influences these properties (Figure 3.5). In an eight-leg steering mechanism the EPWW requires two times the same mechanical steering mechanism, one for the front legs and one for the hind legs. In Table 3.2 an overview is shown of the rotation angles, turning radii, user control methods and number of required actuators of the different steering mechanisms. The maximum rotation angles (θ_1 and θ_2) were determined using SAM Artas. The turning radii for the front- (R_f) and eight-leg (R_e) steering were determined using trigonometry:

$$R_f = \sqrt{\left(\frac{W_b}{2}\right)^2 + \left(\frac{W_b}{\tan(\theta_2)} - \frac{W_t}{2}\right)^2}, \tag{3.1}$$

$$R_e = \frac{W_b}{\tan(\theta_2)} - \frac{W_t}{2}, \tag{3.2}$$

where W_b = 84 mm and W_t = 84 mm represent the chassis length and width, respectively. Detailed derivations of the turning radii equations can be found in Appendix B.1.

3.1.3   Differential mechanism

Besides changing the direction, the legs should also be able to change its speed during steering. In this subsection, mechanisms will be described that change the speed of the legs, which are called differential mechanisms. As described in subsection 3.1.2, an electronic differential can

Steering mechanism

(a) Eight-leg steering   (b) Front-leg steering
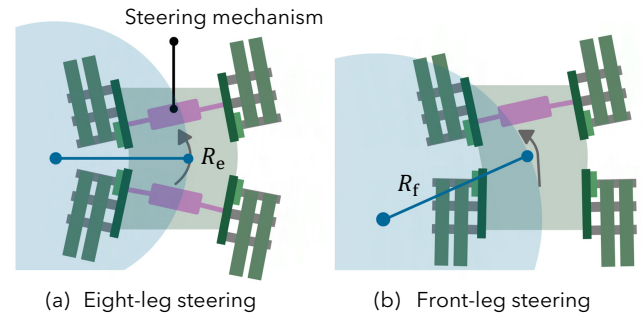
Figure 3.5: Difference between (a) eight-leg steering and (b) front leg steering, in which eight-leg steering requires two steering mechanisms and front-leg steering requires one steering mechanism.

Table 3.2: Overview of the minimum turning radii and maximum rotation angles of the electronic and mechanical steering mechanisms, in which the electronic steering mechanism uses two actuators to control the left and right legs; while mechanical steering mechanisms change the direction of the legs mechanically.

Steering Mechanism	R_f[1] (mm)	R_e[2] (mm)	θ_1[3] (°)	θ_2[4] (°)	User control (direction and speed)	# Actuators[5]
Electronic	-	0	0	0	Two-axis joystick.	2
Ackermann	107	28	24	31	Manual steering with one-axis joystick/buttons or two-axis joystick.	1/2 or 2/3
Bell-crank	99	24	24	33	Manual steering with one-axis joystick/buttons or two-axis joystick.	1/2 or 2/3
Rack-and-pinion	113	32	24	30	Manual steering with one-axis joystick/buttons or two-axis joystick.	1/2 or 2/3

[1]: Minimum turning radius of the steering mechanism at the front legs.
[2]: Minimum turning radius of the two steering mechanisms for all eight legs.
[3]: Maximum rotation angle of the inner front legs, which was set the same for all the mechanical steering mechanisms.
[4]: Maximum rotation angle of the outer front legs.
[5]: Maximum number of actuators (front or eight leg), including walking and steering mechanism, depending on the user control.

change the rotational speeds of the left and right legs with respect to each other by using two rotational DC motors. For the mechanical steering mechanisms, mechanical differentials can be used to change the rotational speeds of the legs during steering. In a mechanical differential, torque is applied to the driving legs through a differential gearbox. This allows the legs of the EPWW to rotate at unequal speeds while making a turn. These type of mechanical differentials can be categorized into bevel gear, spur gear and gearless differentials [72, 73].

The simplest bevel gear differential is the open differential, which consists of a propeller shaft delivering output from the steering of the user (Figure 3.6a) [73]. The crown wheel connects the propeller shaft with the differential coupling, which sends torque to the gears in the rotating cage [74]. When the EPWW moves straight, the small gears move with the crown gears as a single unit, in which both large gears rotate with the same speed. Steering the EPWW will result in the small gears to rotate around their own axis, which allows the large gears to rotate at different speeds [75]. Spur gear differentials have a similar principle, however instead of bevel gears, a planetary gear set with spur gears is used (Figure 3.6b) [76]. Gearless differentials are differentials without gears, which use bearings and sliding elements. There are many variations of differentials with sliding elements, for example the differential from Young et al. (1993), as shown in Figure 3.6c [77]. The sliding elements are inclined and have a triangular shape. The disks that are in contact with the sliding elements are similar to the bevel gears of an open differential. Behind each disk, toothed rings are placed for conveying rotary motion with a variable gear ratio by using friction.

3.1.4   Transmission mechanism
Transmission mechanisms are required to connect the front and hind legs, which depend on the type of steering and differential mechanism that will be selected. In an electronic differential the left and right legs should be able to rotate at different speeds, in which a minimum of two brushed DC motors are required. One DC motor needs to rotate four legs at the left side of the EPWW and one DC motor needs to rotate four legs at the right side of the EPWW. In order to achieve an EPWW with a mechanical differential, two differentials are required, one for the front legs and one for the hind legs. All the mechanical differentials can be

applied to the mechanical steering mechanisms as described in subsection 3.1.2, which are considered equally complex. Additionally, it should be considered that the connection between the crank and each mechanical steering mechanism should be an universal joint, allowing for 2DOF; and an additional transmission mechanism is required to connect the front differential with the hind differential.

In Figure 3.7 the different transmission mechanisms are shown. Possible transmissions include a double crank four-bar mechanism, three gears in series or two gears with a timing belt. In Figure 3.8 all the possible transmission and actuator configurations are shown for the electronic and mechanical steering mechanisms; and their corresponding differential mechanisms and AL-ratios.

3.1.5   Actuators
Since the use of a lead acid battery is required (C4, C4-1), which only supplies a DC current, only DC motors were considered for the different actuators. DC motors can be either brushed or brushless, as shown in Figure 3.9. The simplest and cheapest DC motor is the brushed DC motor, which has a stationary magnet and DC-current-carrying coil connected to a shaft that rotates through the permanent fixed magnetic field (Figure 3.9a) [78]. To keep the loop moving and produce rotation, a commutator with brushes switches the direction of the current, mimicking an alternating current. The advantages of a brushed DC motor include the costs, the small size, easy to control with a motor driver and low power consumption [79]. However, the brushes wear out fairly fast if large amounts of current are applied, in which the efficiency will be lower due to more heat generation. This means that more costs will be required for maintenance.

Brushless DC motors replace the physical brushes and commutator with an electronic means of achieving commutation, typically through the use of hall effect sensors or encoders (Figure 3.9b) [79]. These are more reliable with a longer life cycle, higher torque, higher efficiency and less maintenance, however are more expensive and require more complicated speed controllers. An example of a brushless DC motor is a stepper motor, which divides a full motor rotation into a number of equal steps using an open-loop position control [80]. A stepper motor has therefore a limited position accuracy. Furthermore, servo motors can be brushed or

(a)	(b)	(c)
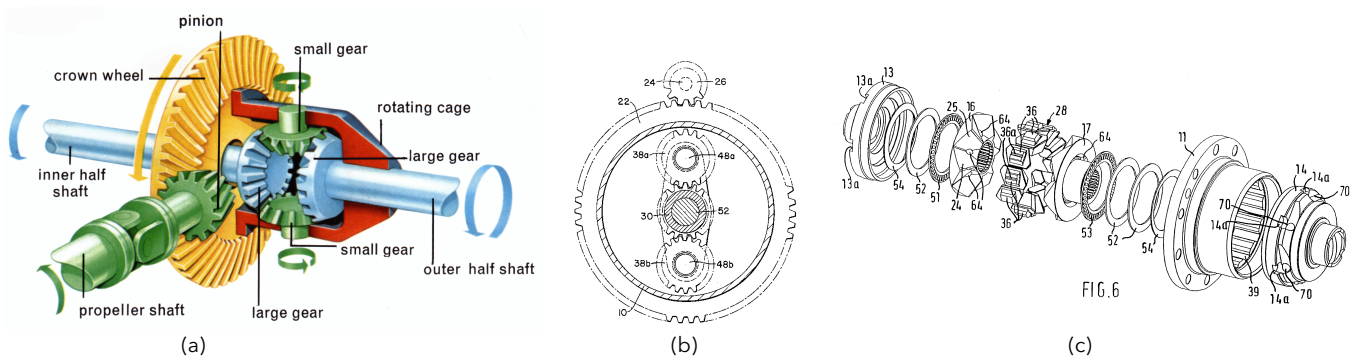
Figure 3.6: (a) Different components of an open differential [75]. The propeller shaft transmits the torque input of the user to the crown wheel, which is connected to the rotating cage. In the rotating cage a planetary gear box determines the speed of each side of the legs. (b) Spur gear differentials use planetary gear boxes instead of bevel gears [76]; and (c) gearless differentials use sliding elements, disks, toothed rings and friction to achieve the same principle [77].

(a) Double crank   (b) Three gears

(c) Two gears with timing belt
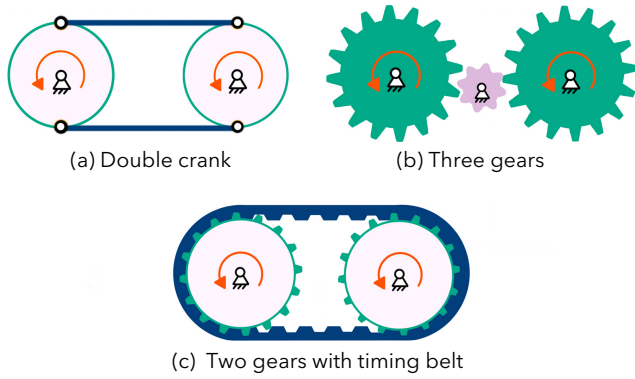
Figure 3.7: Different transmission mechanisms for the differential mechanisms with (a) the double crank mechanism; (b) three gears in series and (c) two gears with a timing belt.

Table 3.3: Overview of the leg mechanism selection according to the performance criteria. Each mechanism received a grade for each criteria, which was multiplied with a weight, resulting in a final score. The sum of all the individual final scores resulted in a total final score for each leg mechanism, with Trotbot's linkage as the best concept.

PCID[1]	W[2]	Klann	Jansen	Trotbot	Strider
PC1-1 Complexity	1	3	2	1	4
PC2-1 Stability	8	8	16	24	32
PC3 Size	5	15	10	20	5
PC4 Step height	4	16	12	8	4
PC5 Step length	2	6	8	6	4
PC6 Footpath	6	12	6	24	18
PC7 Slope	3	9	6	12	3
PC8 Adaptability	6	6	12	24	24
Total		75	72	**119**	94

[1]: Performance criteria according to the leg mechanism criteria in subsection 2.4.2.
[2]: Weight of each performance criteria.

brushless, in which a closed-loop servomechanism with position feedback controls the motion and final position [81]. This means that servo motors are more accurate, but also more expensive than stepper motors.

3.2 Concept selection
3.2.1 Leg mechanism
The final leg mechanism was selected according to the performance criteria described in subsection 2.4.1. Each criteria received a weight from 1-8, indicating the importance of the criteria (Appendix B.2.1). The leg mechanisms were graded from 1-4 at each criteria, in which the best mechanism received the highest grade. Multiplying the weight of each criteria with the corresponding grade resulted in a final score for that specific criteria. In Table 3.3 an overview is shown of the different scores of the performance criteria of the leg mechanisms.

Complexity (PC1-1) - The leg mechanism should be as simple as possible, this means that the number of links and joints should be minimized; which decreases the

complexity, manufacturing costs and maintenance costs of the leg mechanism. Therefore, Strider received the highest score due to the double leg mechanism, while Trotbot received the lowest score.

Stability (PC2) – Minimizing the vertical vibrations experienced by the user can be achieved by having a smooth and steady gait. The foot speed range should therefore be minimized, in order to avoid this bouncing and consumption of energy from constantly accelerating and decelerating the EPWW [60]. Hence, Strider received the highest score and Klann the lowest score.

Size (PC3-1) – When looking at the space each leg mechanism would occupy if the crank radius were equal or if the step heights were equal; it can be seen that Trotbot requires the least space, which consist of a toe and heel; while Strider requires the most space for only half of its mechanism.
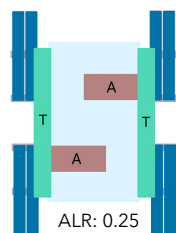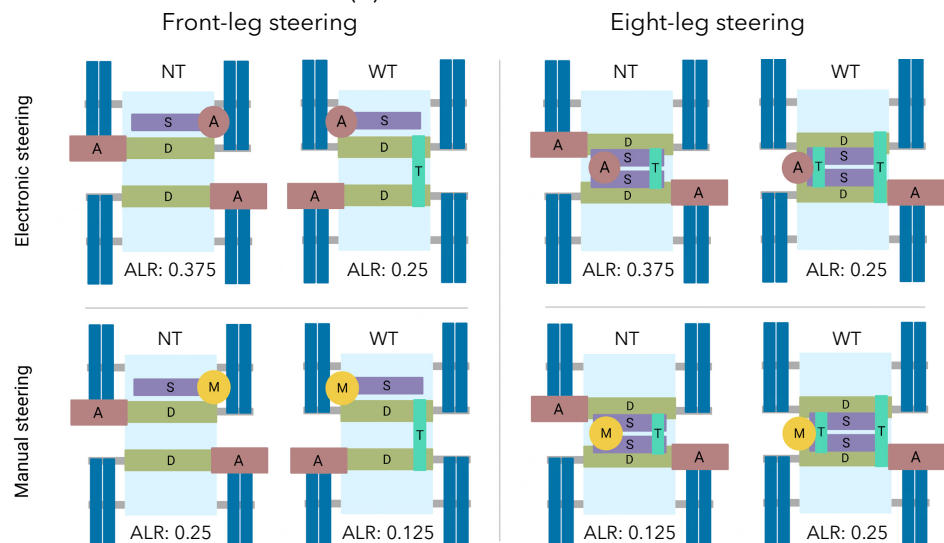
Figure 3.8: Overview of all the possible transmission and actuator configurations with the corresponding AL-ratio (ALR), which are divided into (a) electronical differentials and (b) mechanical differentials (e.g. open differential). The different configurations in front-leg and eight-leg steering include configurations with one to three actuators for the speed control and steering mechanisms (e.g. Ackermann). The number of actuators depend on the transmission mechanism configuration and whether the EPWW will be steered with a joystick or manually. Furthermore, the mechanical steering mechanisms can be divided into no transmission mechanism between the differentials (NT) and with transmission mechanism between the differentials (WT).

14
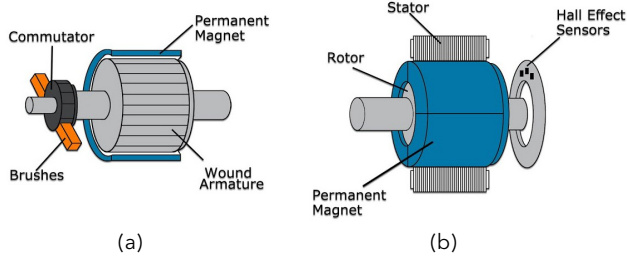
Figure 3.9: The different types of DC motors [79]. (a) Brushed DC motors have a wounded armature connected to a shaft with a commutator with brushes that rotate through a permanent fixed magnetic field. (b) Brushless DC motors use hall effect sensors or encoders to replace the commutator with brushes.

Step height and step length (PC4, PC5) – Both the step height and step length should be maximized. Strider received the lowest score for both the step height and step length; while Klann received the highest score for the step height; and Jansen received the highest score for the step length.

Footpath design (PC6) – The footpath design determines what type of obstacles the legs can avoid. A foot-path design with a large maximum step height is desirable, however it should be considered that some foot-path shapes can cause jamming when lifting their feet over obstacles. A triangular foot-path may be high at the center, but can still collide against obstacles, for example when walking reversed. The footpath should be symmetrical on the horizontal and vertical center lines, such that the inertia forces are equally balanced [67]. Additionally, the footpath should have a long straight stride. Therefore, Trotbot received the highest score due to its oval shape and large step-height-to-step-length ratio. Strider was ranked the second due to its oval shape, but with a smaller step-height-to-step-length ratio. Jansen received the lowest score due to its triangular shape and small step-height-to-step-length ratio.

Climbing slope (PC7) – The required height of the leg mechanism influences the center of gravity of the overall EPWW, which should be as close to the ground as possible for stable walking. The planar areas in Table 3.1 showed that Trotbot requires the least space, hence the highest score. On the contrary, Strider requires the most space, hence the lowest score.

Adaptability (PC8) – The leg mechanism should be able to adapt to different environments and perform the same in these different environments [68]. Klann is suitable for walking over rugged terrains and obstacle avoidance.

However, the large fluctuations in the foot stride speed makes Klann not the best solution for walking on flat terrain. Jansen excels in smooth walking on flat terrain, however lags in walking over rugged terrain. Therefore, Trotbot and Strider received the highest scores, which are suitable for all terrains.

Looking at the total sum of all the final scores, it is clearly noticeable that Trotbot's leg mechanism has the highest score with a total of 119, compared to the 72, 75 and 94 of the Klann's, Jansen's and Strider's mechanisms. The Trotbot excels in the criteria stability, size, overall footpath design, climbing slope and adaptability. However, improvements in the step height and complexity are necessary.

3.2.2 Steering mechanism

The final steering mechanism was selected according to the performance criteria described in subsection 2.4.2. Each criteria received a weight from 1-3, indicating the importance of the criteria (Appendix B.2.2). The steering mechanisms were graded from 1-7 at each criteria, in which the best mechanism received the highest grade. Multiplying the weight of each criteria with the corresponding grade, resulted in a final score for that specific criteria. In Table 3.4 an overview is shown of the different final scores of the steering mechanisms.

Costs (PC1-2) – The electronic differential does not require an additional steering mechanism, which minimizes the costs. The front-leg mechanical steering mechanisms received higher scores than the eight-leg mechanical steering mechanisms, since less components were required for the front-leg steering mechanisms. Moreover, Ackermann's mechanism was considered the least expensive mechanical steering mechanism and the rack-and pinion was considered the most expensive steering mechanisms due to its design complexity.

Size and mass (PC3-2) – Similarly, the electronic steering received the highest score for the required space and mass. The eight-leg mechanical steering mechanism received the lowest scores, since these mechanism required the most space and largest mass. Furthermore, when comparing only the mechanical steering mechanism, Ackermann received the highest score and rack-and-pinion received the lowest score, since this mechanism would require the most components.

Turning radius (PC10) – The electronic differential received the highest score since the EPWW was able to spin around its own axis (R_e = 0 m m). W hen l ooking a t t he mechanical steering mechanisms, the front-leg steering mechanisms resulted in larger turning radii than the eight-leg steering mechanism. In both cases the Bell-crank

Table 3.4: Overview of the steering mechanism selection according to the performance criteria. Each mechanism received a grade for each criteria, which was multiplied with a weight factor, resulting in a final score. The sum of all the individual final scores resulted in a total final score for each steering mechanism, with electronic differential steering as the best concept.

PCID[1]	W[2]	Electronic	Ackermann		Bell-crank		Rack-and-pinion	
			Front	Eight	Front	Eight	Front	Eight
PC1-2 Costs[3]	2	14	12	6	10	4	8	2
PC3-2 Size and mass[3]	1	7	6	3	5	2	4	1
PC10 Turning radius	3	21	6	15	9	18	3	12
	Total	42	24	24	24	24	15	15

[1]: Performance criteria according to the steering and control mechanism criteria in subsection 2.4.3.
[2]: Weight of each performance criteria.
[3]: Only of the steering mechanism.

resulted in the largest turning radii, while the rack-and-pinion resulted in the smallest turning radii.

Looking at the total sum of all the final scores, it is clearly noticeable that the electronic steering mechanism has the highest score with a total of 42 compared to the 15, 24 and 24 of the rack-and-pinion, Ackermann and Bell-crank mechanisms.

3.2.3 Differential mechanism, transmission mechanism and actuators

The transmission configuration combines the differential mechanism, transmission mechanism (incl. steering) and the number of required actuators (Figure 3.8). The final transmission configuration was selected according to the performance criteria described in subsection 2.4.3. Each criteria received a weight from 1-3, indicating the importance of the criteria (Appendix B.2.3). The transmission configurations were graded from 1-8 at each criteria, in which the best configuration received the highest grade. Multiplying the weight of each criteria with the corresponding grade, resulted in a final score for that specific criteria. In Table 3.5 an overview is shown of the different final scores of the transmission configurations.

Costs (PC1-2) – The electronic differential is the simplest mechanism, which requires the least components; and is therefore expected to be the cheapest solution. Furthermore, the mechanical differentials with manual steering and transmission mechanisms were also expected to be low-cost solutions. However, due to the additional mechanical components of the mechanical differential and steering mechanisms, these were considered more expensive with respect to the electronic differential. The mechanical differentials with electronic steering and without transmission mechanism received the lowest score, since these mechanisms required the most components.

AL-ratio (PC9) – The AL-ratio of the different transmission configurations ranged between 0.125 and 0.375; in which the mechanical differentials with manual steering and transmission mechanisms received the highest score, since only one actuator was required. The mechanical differentials with electronic steering and without transmission mechanism received the lowest score, since three actuators were required.

User control (PC11) – From an user perspective, the number of actions performed for steering and speed control should be minimized. The electronic differential,

and mechanical differentials with electronic steering received the highest score, since a two-axis joystick needs to be used to steer the EPWW. The mechanical differentials with manual steering received lower scores, in which manual steering of eight-leg steering received the lowest score. Steering eight legs manually was expected to require a larger force output by the user than manual steering of only the front legs.

Looking at the total sum of all the total scores, it is clearly noticeable that the electronic differential has the highest score with a total of 42. The electronic differential received the highest scores in the criteria costs and user control; and received the second highest score for the AL-ratio. Combining these results with the steering mechanism results (3.2.2), shows that the electronic differential is the most suitable solution in terms of costs, size, maneuverability and user control. Therefore, no additional mechanical differential mechanism was required.

3.3 Final concept

Combining the results of the concept selection (3.2), resulted in a concept with a Trotbot leg mechanism, electronic steering mechanism and electronic differential. For the final concept a transmission mechanism and type of actuator were also selected. As described in subsection 3.1.4, there are different transmission mechanisms that can connect the front and hind legs of the EPWW. The use of a double crank four-bar mechanism is considered the simplest and cheapest solution. However, using additional links will increase the width of the EPWW. Additionally, closed-chain mechanisms would result in additional singularity points [82]. On a scaled prototype the use of three gears also seemed to be a simple solution. However, when considering a full scaled prototype, three large gears such that the front and hind legs would not interfere with each other, would result in increasing costs. Therefore, the use of two gears with an additional timing belt was the most suitable solution for an electronic differential. Furthermore, considering that the complexity and costs should be minimized (PC1-2) and that the proof of concept will be an 1:3 scaled prototype (S1); the continuous rotational brushed DC motor was the most suitable solution for an electronic differential. In Figure 3.10 the final concept with the Trotbot leg mechanism, electronic differential, timing belt transmission and brushed DC motors is shown, which is controlled by a two-axis joystick.

Table 3.5: Overview of the transmission configuration selection according to the performance criteria, divided into electronic differentials and mechanical differentials (front- and eight-leg steering). Each mechanism received a grade for each criteria, which was multiplied with a weight factor, resulting in a final score. The sum of all the individual final scores resulted in a total final score for each transmission configuration, with an electronic differential as the best concept.

PCID[1]	W[2]	Electronic differential	Front-leg steering				Eight-leg steering			
			Electronic		Manual		Electronic		Manual	
			NT[3]	WT[4]	NT	WT	NT	WT	NT	WT
PC1-2 Costs[5]	2	16	4	10	10	14	2	6	8	12
PC9 AL-ratio	1	2	1	2	2	3	1	2	2	3
PC11 User control	3	9	9	9	6	6	9	9	3	3
Total		27	14	21	18	23	12	17	13	18

[1]: Performance criteria according to the steering and control mechanism criteria in subsection 2.4.3.
[2]: Weight of each performance criteria.
[3]: Without transmission mechanism between the two differential mechanisms.
[4]: With transmission mechanism between the two differential mechanisms.
[5]: Estimated costs of the steering, differential and transmission mechanisms and actuators combined.
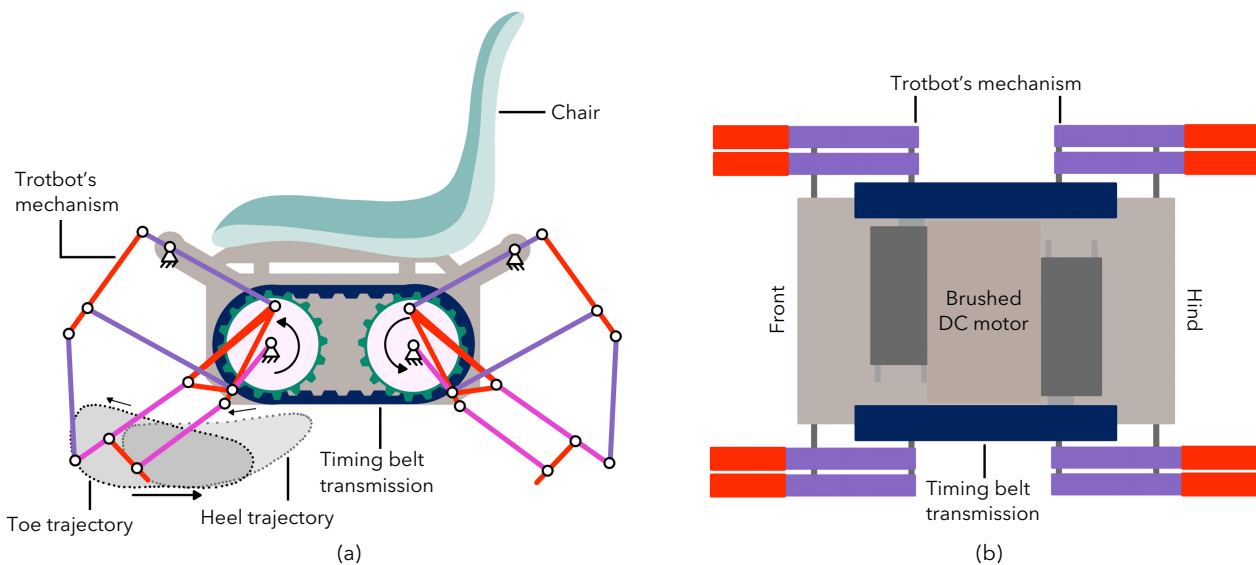
Figure 3.10: (a) Side view of the final concept and (b) top view of the chassis of the final concept. The final concept consist of eight Trotbot legs with timing belt transmission, electronic differential and two brushed continuous rotating DC motors; which is controlled by a two-axis joystick.

4 Final design

4.1 Mechanical design

4.1.1 Leg mechanism design

The maximum seat height must be 173 mm (C7), which means that the maximum height of the leg mechanism also must be 173 mm, such that the legs will not obstruct the user. Considering this constraint, the original Trotbot mechanism had a maximum toe step height of 48 mm, heel step height of 43 mm, toe step length of 107 mm, heel step length of 116 mm and total step length of 137 mm. According to leg constraint C18, the minimum step height must be 50 mm. Modifying the Trotbot mechanism with the path optimization function in SAM Artas, by replacing ground joint 12 to joint 11, resulted in a maximum toe step height of 57 mm, heel step height of 46 mm, toe step length of 110 mm, heel step length of 126 mm and total step length of 151 mm (Figure 4.1). Furthermore, the maximum absolute velocity of the toe and heel decreased from 0.54 m/s and 0.63 m/s to 0.44 m/s and 0.52 m/s, resulting in a smoother grounding [83].

The wheelchair width must not exceed 233 mm (C5), in which 150 mm was already occupied by the seat width (C9). This means that the total width of the left and right leg mechanisms combined must not exceed 83 mm; and the width of one leg must not exceed 20.75 mm. Therefore, the pivot joints also required the least amount of space, which corresponded to the minimum head thickness (d_h) of the pivot joints. In Figure 4.2 an overview is shown of the different types of suitable pivot joint mechanisms. Bolts and nuts require the most amount of space, with a d_h of 4 mm for a M5 bolt. Moreover, due to the threaded surface of the bolts, additional bearings would be required, which results in additional costs. The remaining solutions have a smooth shaft which do not require additional bearings, and therefore reduce costs. Book screws have a d_h of 1.7 mm for a shaft diameter 5 mm. Pivot pins with push on fasteners for a shaft diameter of 5 mm require a d_h of 2.6 mm [84]. Clevis pins with c-clips require the least amount of space with a d_h of 1.5 mm for a shaft diameter of 5 mm. However, these types of joints are difficult to find and expensive with respect to the other two solutions. Therefore, steel nickel

Figure 4.1: The original and modified Trotbot linkage, in which the ground joint 12 in the original leg mechanism was moved to the position of joint 11 in the modified mechanism, while the lengths of the links remained the same. This resulted in larger step heights, larger step lengths and smaller peak velocities.
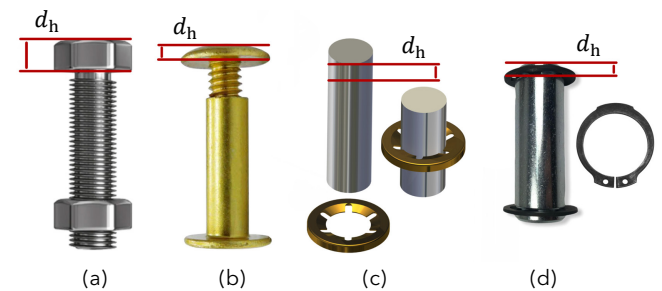
Figure 4.2: Different types of pivot joint mechanisms for connecting the links of the leg mechanism, which include (a) bolts and nuts with a minimum head thickness (d_h) of 4 mm, (b) book screws with d_h = 1.7 mm, (c) pivot pins with push on fasteners (d_h = 2.6 mm), and (d) clevis pins with c-clips (d_h = 1.5 mm).

plated book screws were selected as joints for the leg mechanism, since these were easily available at different shaft lengths, such that no additional post-processing would be required.

Since the head diameter of the book screws are 10 mm, a link width of 12 mm was selected. The thickness of the links were a combination of single parts of 2 mm and double parts of 1 mm, such that both, the inner and outer surface of the leg mechanism could subject to almost equal axial loads, while still minimizing the width. In Table 4.1 an overview of the lengths of each link are shown and whether it is a single or double part. The modified Trotbot mechanism with a height maximum of 173 mm, resulted in a left maximum of 139 mm and a right maximum of 43 mm, including the width of the links (Figure 4.3). Combining the front and hind legs would therefore result in a total minimum wheelchair depth of 364 mm, which fits within the maximum wheelchair depth of 433 mm (C6).

Table 4.1: The dimensions of each link of the modified Trotbot mechanism for the EPWW, in which for example BCDO is the combination of the B, C, D and O link, resulting in one part. Each part can be a single part with a thickness of 2 mm or a double part of two links with a thickness of 1 mm.

Link	Length (mm)	Single or double part
A (crank)	34	Single
BCDO	45-58-25-8	Single
EF	66-17	Double
GH	50-17	Single
I	66	Double
JK	21-53	Double
LM	21-8	Single
N	61	Single
P	90	Single

In order to manufacture the links accurately, laser cutting was selected as main manufacturing technique for the production of the prototype. This limited the type of material to aluminium 1050, steel DC01 or stainless steel 304. Aluminium has a density (ρ) of 2.71 g/cm^3, yield strength (σ) of 20 MPa and module of elasticity (E) of 71 GPa [85]. Steel has a ρ of 7.8-7.9 g/cm^3, σ of 140 MPa and E of 200-215 GPa. Stainless steel has a ρ of 7.8 g/cm^3, σ of 190 MPa and E of 200-210 GPa. Aluminium is the lightest of the three, which has a good resistance to corrosion. On the contrary, the yield strength and module of elasticity are low compared to steel and stainless steel, which have similar properties in terms of weight and
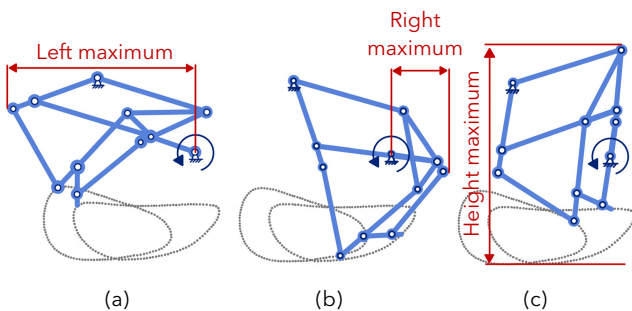
strength. Stainless steel also has a high resistance to corrosion, however is more expensive than normal steel. The links will therefore be made of steel, in which an additional coating will be required to prevent corrosion. The longest 1 mm double link (EF = 83 mm) was considered the weakest link, which was further analyzed in SolidWorks with static force analysis. The positions of joint 3 and joint 11 were considered fixed geometry; and uniform axial forces were applied in the weakest direction of the link until the yield strength was reached, which resulted in a sufficient maximum yield force of 64.6 N.

PLA cylindrical spacers of various lengths were placed in the linkage, in order to prevent collisions between the moving parts of each leg. For example, in joint 2 a spacer of 3 mm was placed for the movement between link P and link BCDO; and in joint 9 a spacer of 3 mm was placed for the movement between link N and link K. Furthermore, "singularity" or "dead point" remains one of the main issues when designing a closed-chain mechanism [82]. This occurs when two links are nearly parallel with respect to each other, resulting in an undetermined point. In the modified Trotbot mechanism, this phenomenon occurs between link BCDO and EF. Therefore, placing a dead point stopper at the B link prevents this singularity point from flipping in the unwanted direction. This resulted in the design of an individual leg as shown in Figure 4.4.

4.1.2 Gear transmission design

In total the EPWW will require eight legs (S2), in which there are four pairs of legs. Each pair consist of an inner leg, which is connected to the inner frame; and an outer leg, which is connected to the outer frame (Figure 4.5). The inner and outer legs are connected with a double crank link, which has two times the length of the crank radius A. Additionally, in order to always have four feet on the ground, a fixed phase shift of 180° between the lead and follower crank is required. This can be achieved by fixing the inner crank parallel to the double crank, using a bolt and nut; and welding the bolt and nut to the two cranks (Figure 4.6).

The left and right side of the EPWW both consist of an outer and inner frame, which are connected by three outer fixing M5 bolts and nuts. The front and hind legs of one leg half are connected by a gear transmission with a timing belt.

(a) (b)

Figure 4.3: The maximum dimensions of the modified Trotbot mechanism, including the link width of 12 mm. (a) The left maximum has a width of 139 mm; (b) the right maximum has a width of 43 mm; (c) and the maximum height is equal to 173 mm.

(a) (b)
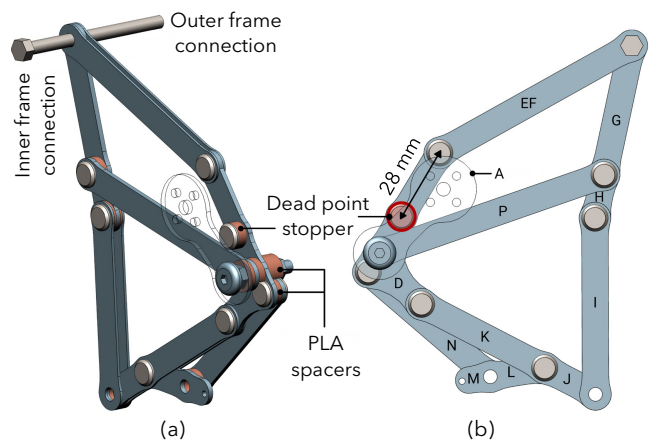
Figure 4.4: (a) Isometric view and (b) front view of the leg mechanism of the inner leg, consisting of 1 mm and 2 mm steel links, book screws, PLA cylindrical spacers and a dead point stopper at link B, in order to prevent the singularity point from flipping to the unwanted direction.
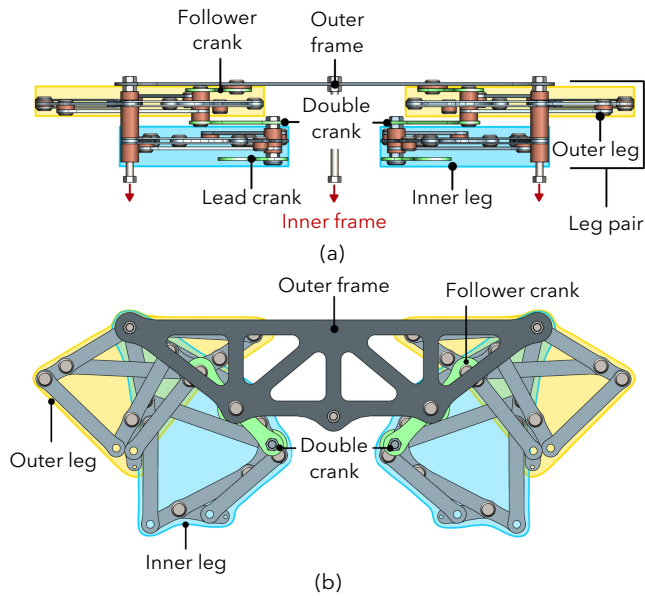
Figure 4.5: (a) Top view and (b) side view of one leg half. The inner frame connects the inner legs with the double cranks, in which the lead crank and double crank are always parallel with respect to each other. The outer legs connect the double crank with the follower crank at the outer frame.
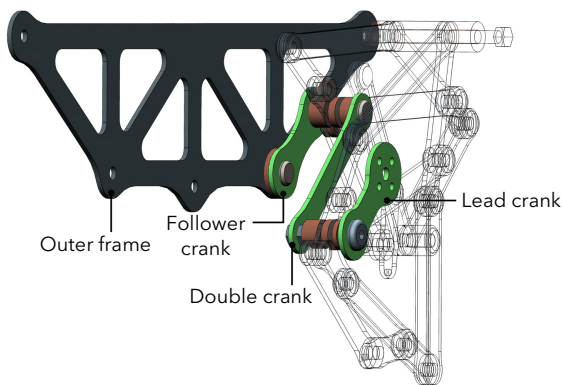
Figure 4.6: A phase shift of 180° is always required between the inner and outer legs, which can be achieved by fixing the lead crank parallel to the double crank. Subsequently, the follower crank will also be automatically parallel to the double and lead crank.

Each lead crank is connected to an aluminium GT2 60 teeth gear with four M3 bolts through a bearing house, as shown in Figure 4.7. The bearing house consist of two outer houses fixed to the inner frame; a thin (20 x 27 x 4 mm) ball bearing; and two inner houses that connect the lead crank and GT2 gear, allowing it to rotate freely. Furthermore, the flat contact surface between the outer house and lead crank, minimizes the bending moment of the lead crank.

The distance between the front and hind legs is 130 mm, which required a GT2 timing belt of 380 mm (Figure 4.8a) [86]. An additional dynamic tensioner was placed at the inner frame between the front and hind legs, in order to tension the timing belt at the required tension force (Figure 4.8b). The belt tensioner consist of a ball bearing, which comes in contact with the timing belt. A M5 bolt connects the ball bearing with a tension spring on the other side of the inner frame through a vertical slot (Figure 4.9). Besides the inner frame, the tension spring is also connected to the outer frame by an outer fixing bolt.
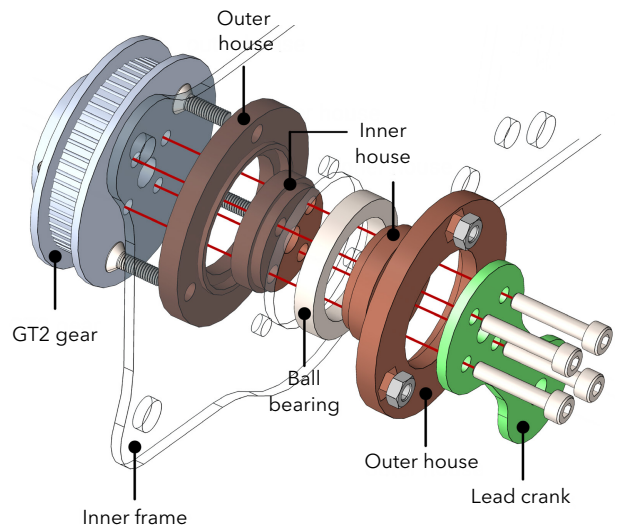
Figure 4.7: The bearing house connects the GT2 gear with each lead crank through two outer houses, two inner houses and a thin ball bearing with an outer diameter of 27 mm and thickness of 4 mm; such that the legs and gears can rotate freely without additional bending moments

When the spring force is larger than the tension force of the timing belt, the spring of the belt tensioner will pull the ball bearing down on the timing belt through the slot. When the spring force is smaller than the tension of the timing belt, the timing belt will push the ball bearing up, such that no additional force will be applied to the timing belt.

The required average deflection force (F_{def}) by the tension spring (Figure 4.10), was determined by the equation, according to the force-deflection method [86]:

$$F_{\text{def}} = \frac{1.05 T_{\text{st}} + 4.448 \left(\frac{t_{\text{span}}}{L_{\text{pitch}}} \right) Y_b}{16}, \tag{4.1}$$
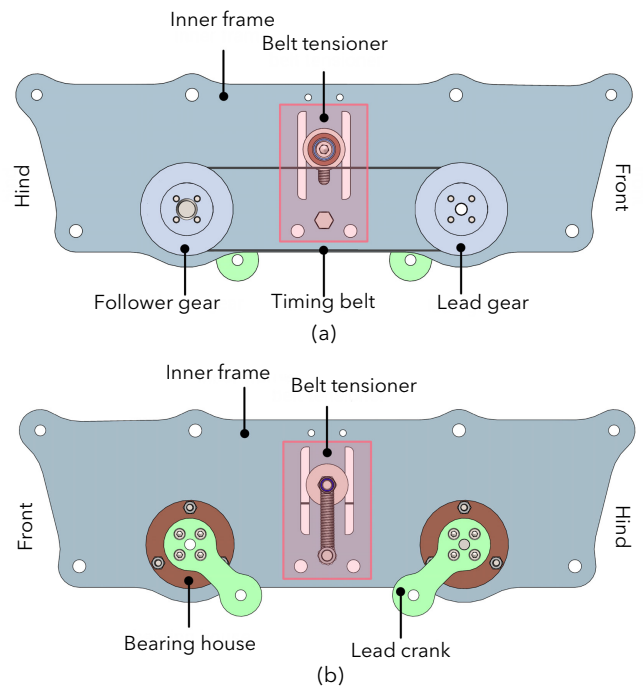
Figure 4.8: The inner frame consist of two bearing houses, two lead cranks and two gears, in which an actuator will be fixed to the lead gear. (a) The follower gear is connected to the lead gear with a GT2 timing belt. (b) A dynamic belt tensioner was placed in the middle of the inner frame, in order to tension the timing belt with the required tension force.
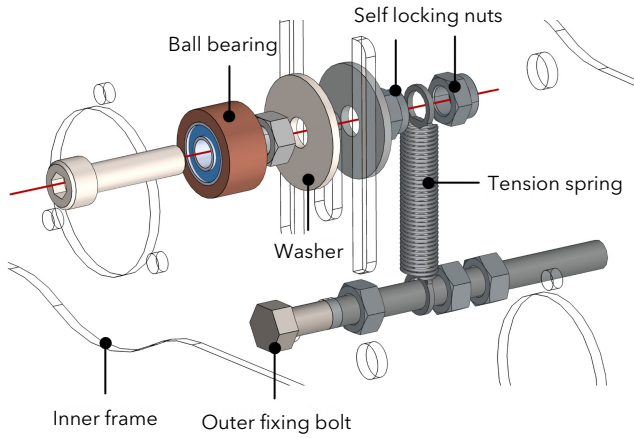
Figure 4.9: The belt tensioner consist of a ball bearing, which is connected to a tension spring by using a M5 bolt through a vertical slot in the inner frame. This allows the tension spring to pull the ball bearing, when the belt tension is too low; and the timing belt to push the tension spring, when the belt tension is too high.
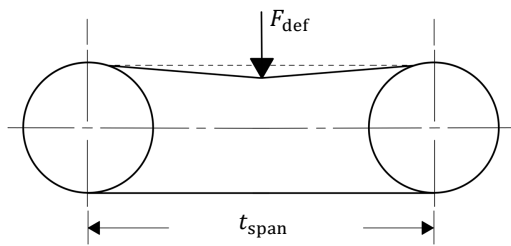
Figure 4.10: The force-deflection method, which relates the deflection of the belt to a required force input, in order to determine the required spring tension deflection force (F_{def}) at a giving span length (t_{span}) between the two GT2 gears [86].

where, T_{st} = 13.34 N, t_{span} = 130 mm, L_{pitch} = 2 mm and Y_{b} = 2.05 represent the minimum static belt tension, span length, belt pitch length and belt constant. This resulted in a required tension spring force of 38.7 N, in which the values of the minimum static belt tension and belt constant were retrieved by the GT2 technical data sheet of SDP/SI [86]. When assuming an initial spring extension (x_{spring}) of 15 mm, a spring stiffness (k_{spring}) of 2.58 N/mm will be required for the belt tensioner.

4.1.3   Feet design

Before designing the ideal foot shape, the angle ranges of the different joint and link connections were analyzed in SAM Artas. In Table 4.2 an overview is shown of the different joints and the maximum and minimum angles between the corresponding link connections.

The minimum and maximum angles of the link connections at joint 7, 8 and 10 resulted in different individual free spaces, in which the toes and heels would not interfere with other links (Appendix C.1). Combining these individual free spaces resulted in the total toe free space, total heel free space and joined free space, as shown in Figure 4.11; in which the joined free space is the maximum free area between the toes and heels. In these free spaces, an additional feet design could be placed, such that the stability of the EPWW could be increased without interfering the movement of the leg mechanism. Shigley (1960) described that the foot of a closed-chain mechanism should be narrow; be capable of supporting large shear

Table 4.2: Overview of the different maximum and minimum angles between different link connections and joints, in which joint 7, 8 an 10 are important joints for the feet design.

Joint	Link connection[1]	Max (°)	Min (°)
2	(B,P)	140	39
3	(B,EF)	147	40
4	(C,K)	228	112
5	(G,P)	122	33
6	(H,I)	188	76
7	(I,J)	75	58
8	(J,L)	148	40
9	(N,O)	194	94
10	(M,N)	129	45
11	(EF,G)	148	49

[1]: The angle between the corresponding links.

deflections in the direction of travel; must be able to accommodate the angle movement of the leg mechanism; and should be capable of supporting and absorbing shock in the vertical direction [67]. Therefore, Shigley proposed an "ideal" foot shape, which has a rounded triangular shape with additional rubber placed below the foot. Combining the free space and the proposed design requirements of Shigley, the final toe and heel design was determined as shown in Figure 4.12.

The toe design follows the circular shape of joint 7, while the heel design follows the shape of joint 10 and link M combined. Increasing the width of these shapes, increased the contact area with the ground and therefore also increased the stability. The widths of the feet were chosen,
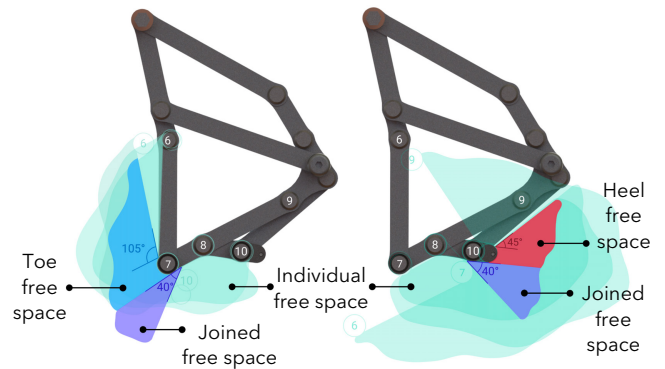
Figure 4.11: The free spaces of the toe and heel of the leg mechanism. The individual free spaces represent the free spaces around the toes and heels, when the maximum or minimum angle of the corresponding link connection is reached. (a) The toe free space (105°) shows the area, in which there is always no link that interferes with the toes. (b) The heel free space (45°) shows the area, in which there is always no link that can interfere with the heels. The joined free space (40°) is the area that is free in between the toe and heel of the leg.
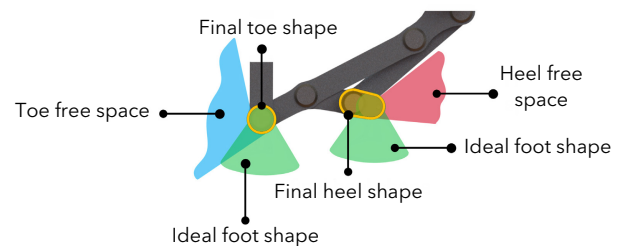
Figure 4.12: The toe and heel free space, ideal foot shape proposed by Shigley (1960); and the final toe and heel shape, which were retrieved by combining the free spaces and Shigley's design [67].

such that the movement of the different links would not be obstructed by the feet. The toes consist of two cylinders with a length of 12 mm and 16 mm, which are connected with one book screw. The 12 mm cylinder was placed closest to the side of the double crank for both the inner and outer leg, resulting in a symmetric feet design between the inner and outer feet (Figure 4.13 and 4.14). The heels of the inner and outer legs have a width of 13 mm, in which the heel was fixed to the leg mechanism by a book screw in joint 10; and a fixation screw between the heels and M links. Both the heels at the inner and outer leg were placed at the same side as the 16 mm toe cylinders, in which at the outer legs an additional spacer was placed between the heel and link M (Figure 4.14). Additionally, due to the limited joined free space, only a thin rubber layer could be placed around the toes and heels without interfering the movement of the leg mechanisms. This would still provide some shock absorption and prevent slip with the ground. In Appendix C.2 more detailed exploded views of the different toe and heel designs can be found.

4.1.4   Actuator selection

Before selecting an actuator, the minimum required motor torque was determined. The minimum torque should be enough for the EPWW to climb a slope (α) of 28° (C21) and lift a payload up to 3.7 kg (C2). The EPWW will be subjected to gravity (F_g) and resistance forces (F_r), which consist of air drag resistance (F_{air}) and friction (F_f) (Figure 4.15) [87].
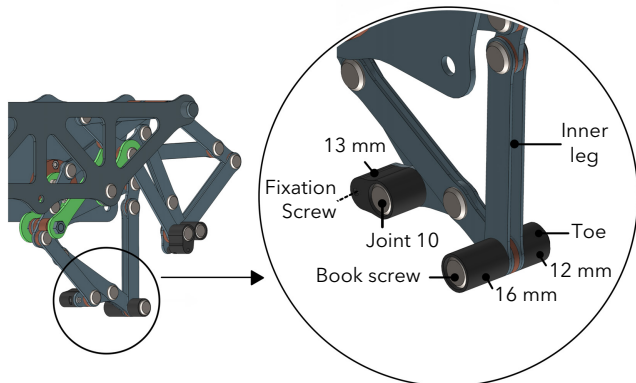
Figure 4.13: Foot design of the inner legs, in which the toe shape consist of two cylinders of 12 mm and 16 mm and the heel shape has a width of 13 mm fixed with a fixation screw to link M.
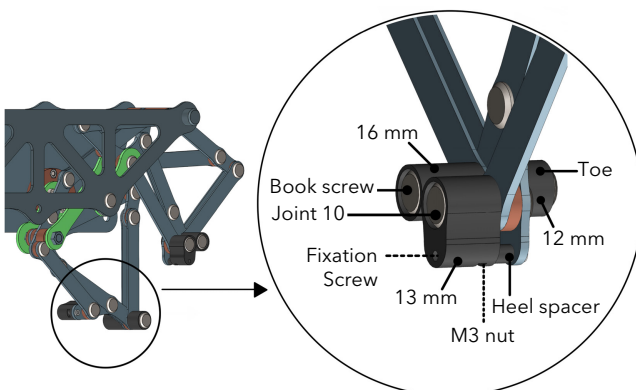
Figure 4.14: Foot design of the outer legs, in which the toe shape consist of two cylinders of 12 mm and 16 mm; and the heel shape has a width of 13 mm fixed with a fixation screw to link M and a heel spacer between the heel and link M.

Therefore, the actuator has to provide a traction force (F_t) to overcome these resistances when walking at a constant speed. This was determined by the following equation:

$$F_t = F_g \sin(\alpha) + F_r = F_g \sin(\alpha) + F_f + F_{air}, \qquad (4.2)$$
$$F_t = m_{ev}g\sin(\alpha) + \mu_k m_{ev}g\cos(\alpha) + \frac{1}{2}pAc_dv^2, \qquad (4.3)$$

where m_{ev} is the estimated total mass with payload of the EPWW (excl. legs), g is the gravitational constant and μ_k is the kinetic friction coefficient between the feet and ground. The air drag resistance was influenced by the air density p, vehicle front surface area A, air drag coefficient c_d and velocity v; in which the surface of the EPWW was simplified to a rectangle. When assuming that one actuator had to provide half of the traction force with a crank radius of 34 mm, a minimum traction torque of 0.704 Nm was required. Furthermore, additional torque due to the inertia of the Trotbot leg mechanism was determined in SAM Artas, which resulted in a torque of 0.116 Nm for one side of the EPWW. This resulted in a total continuous rated torque of 0.820 Nm. Further details on all the parameters of the model are described in Appendix C.3

When selecting the most suitable actuator, the risk of the actuator overheating was also considered. Therefore, the maximum torque of the actuator had to be at least two times the continuous rated torque (1.64 Nm) [88]. Considering these specifications, the *Modelcraft RB350050-22H22R* brushed DC motor was selected as the actuator, which has a maximum no load speed of 120 RPM and maximum torque of 5.7 Nm. However, the nominal torque at highest efficiency, in which the heat generation is minimized, is equal to 0.94 Nm with a current of 3.96 A and speed of 102 RPM [89]. This resulted in the half chassis design as shown in Figure 4.16, in which the DC motor was fixed to the lead gear, and two DC motor clamps fixed the motor to the inner frame. The follower gear was fixed to the inner frame by the follower gear frame. Combining two half chassis', resulted in the total chassis with two DC motors and eight legs as shown in Figure 4.17, in which each DC motor was fixed to both inner frames.
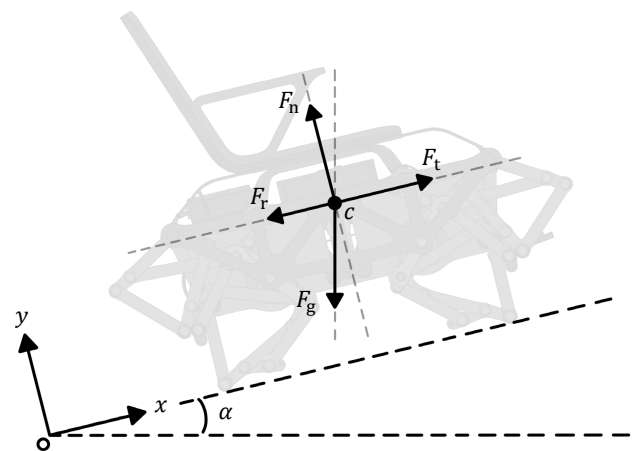
Figure 4.15: The different forces acting on the center of mass (c) of the EPWW when walking uphill on a slope (α), including a normal force (F_n). The EPWW should provide a traction force (F_t) to overcome gravity (F_g) and resistance forces (F_r), which consist of air drag resistance (F_{air}) and friction (F_f) [87].
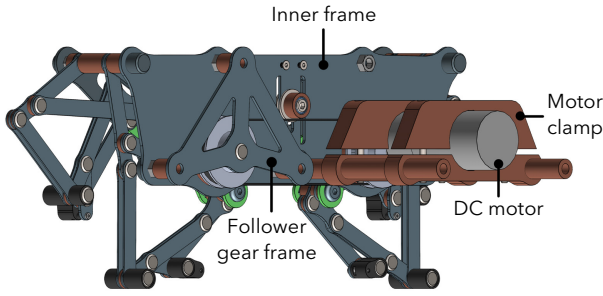
Figure 4.16: Dimetric view of half of the chassis, in which the DC motor is connected with the lead gear and fixed to the inner frame by two motor clamps; and the follower gear frame fixes the follower gear to the inner frame.

4.2   Electric circuit design

The electric circuit of the EPWW consist of a lead-acid 6V battery, that powers two 6V DC motors, an Arduino nano, a volt meter, motor driver and dual axis-joystick (Figure 4.18). The on/off switch allows to turn the motors on and off, in which a green LED will indicate whether the EPWW is on or off. A motor driver allows to change the rotation direction of the DC motors. In order to select the correct motor driver, the required current of the DC motors at maximum efficiency was considered, which is 3.96 A [89]. This means that the motor driver should also be able to require this input current. Therefore, the *MDD10A Dual Channel 10A DC Motor Driver* of Cytron was selected for the circuit, which can provide a maximum continuous motor current of 10 A and allows a power input voltage from 5 V – 30 V.
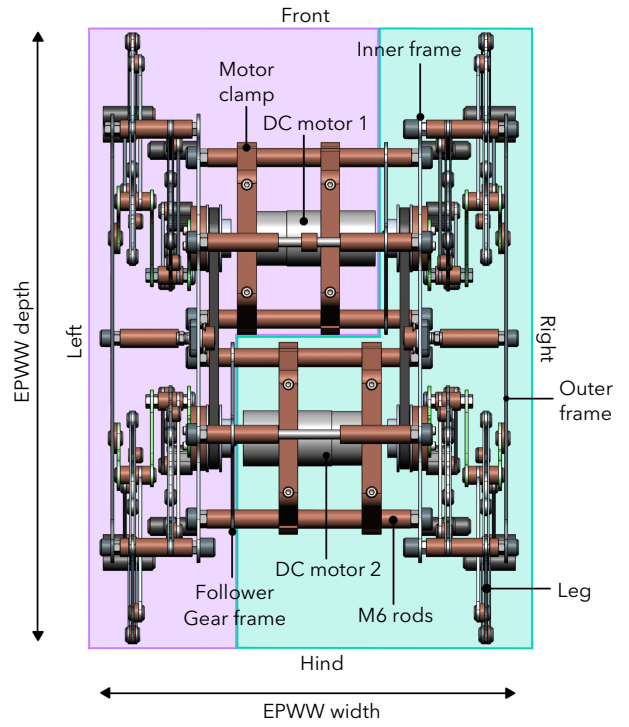
Figure 4.17: Top view of the complete chassis, in which two half chassis' were combined through six M6 threaded rods and PLA spacers between the two inner frames. This resulted in a design of two DC motors, four motor clamps, two gear transmissions and eight legs.
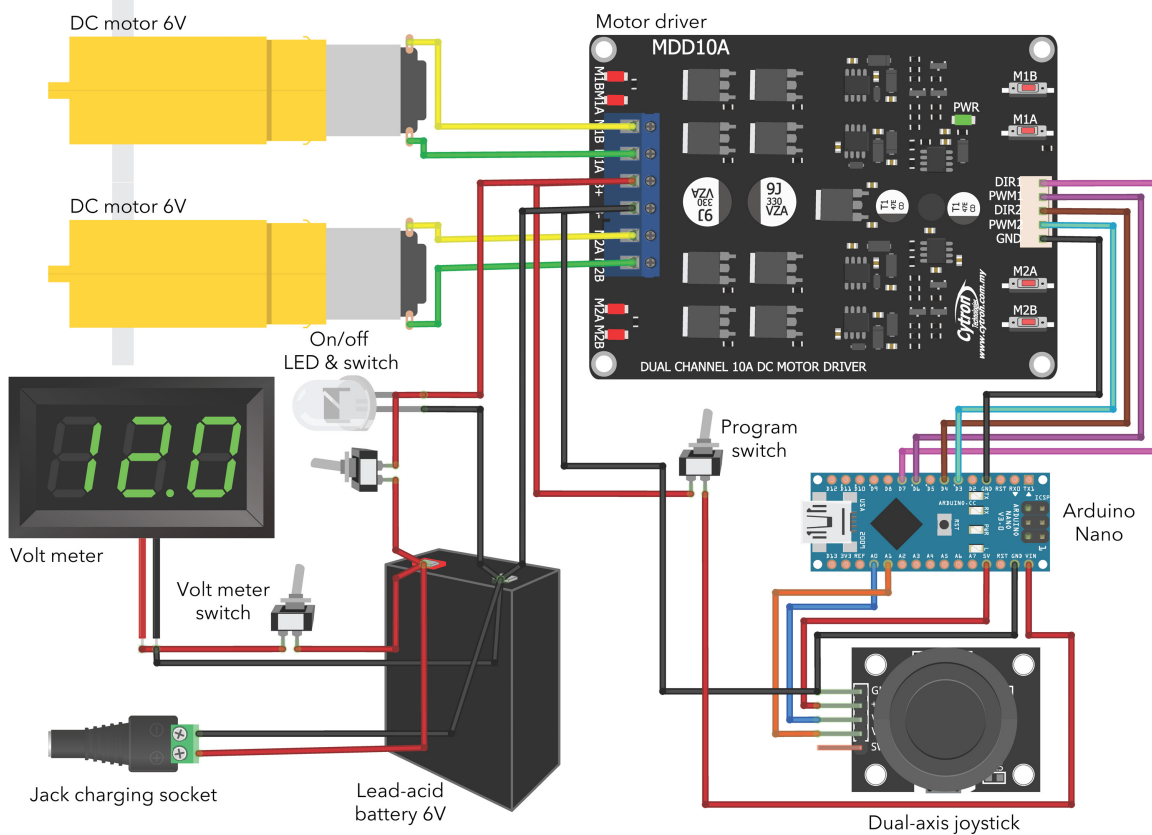
Figure 4.18: The electric circuit of the EPWW, which consist of a 6V lead-acid battery that powers the 6V DC motors, the MDD10A motor driver, Arduino Nano and dual-axis joystick. Additional switches were placed in the circuit to break or close the electric circuit, in which the on/off switch turns the EPWW on or off; the program switch allows to (re-)program the Arduino; and the volt meter allows to measure the voltage of the battery. Furthermore, a jack charging socket was placed to recharge the lead acid battery.

The motor driver connects the DC motors with the Arduino nano, such that the DC motors can be controlled by a dual-axis joystick. A program switch was placed, which had to be turned off when programming the Arduino, in order to prevent current from the battery flowing through the programming device and damaging it. For selecting the lead-acid battery (C4), the dimensions between the two inner frames and two actuators were considered, which had a maximum space of 140 mm x 82 mm x 50 mm (width x depth x height). Furthermore, the battery must provide a voltage of 6 V due to the selected DC motors (4.1.4), which resulted in the *Power Sonic PS-630ST rechargeable lead-acid battery* with a capacity of 3400 mAh.

The DC motors required a current of 3.96 A at maximum efficiency and the Arduino Nano required a current of 40 mA, which resulted in a total required current of 4 A. This would allow the EPWW to operate for 51 minutes at a speed of 102 RPM. The total step length of the legs was predicted to be 151 mm (4.1.1). Combining these results with the specifications of the battery, the EPWW was predicted to travel 786 m at an average speed of 0.257 m/s. Furthermore, the volt meter measures the voltage of the battery when turning on the volt meter switch. This allows to track the battery capacity, in which the battery voltage decreases when the battery capacity decreases.

The jack charging socket allowed to charge the lead-acid battery. The lead-acid battery was placed in between the two inner frames of the EPWW in a battery box (Figure 4.19a). The other electronic control components were placed in the switch box and control box of the EPWW at the back of the chassis (Figure 4.19b). In the switch box the on/off switch, charging socket, volt meter and volt meter switch were placed; and in the control box the Arduino, program switch and motor driver were placed. The joystick consists of a joystick front case, thumb stick, two-axis control stick and joystick back case, which connects the Arduino through a 4 m coil cord (Figure 4.19c). The two-axis control stick consists of two potentiometers, that read the user's analog input, due to a change in output voltage.

4.3 Overall final design

In order to complete the final design of the 1:3 scaled EPWW, a chair was designed according to the dimensional constraints as described in subsection 2.3.2, such that a payload could be placed during the evaluation phase of the prototype. The chair consisted of a seat, two armrests and footrests (Figure 4.20). Furthermore, safety shields were placed to cover the moving components of the EPWW, which consisted of two mudguards at the legs; and a back and front shield in order to protect the rotating gears and DC motors. Combining all the components described in section 4.1 and 4.2 resulted in the final overall design, named the OctoWalker, as shown in Figure 4.20 and 4.21. The EPWW has a total wheelchair depth of 396 mm; wheelchair width of 256 mm; wheelchair height of 321 mm; and seat height of 173 mm. The total estimated mass of the EPWW was equal to 4.8 kg; and the total number of components is equal to 817.

5 Prototyping
5.1 Leg and feet mechanism

The first step of producing the 1:3 scaled prototype of the OctoWalker, consisted of laser cutting all the links of the leg mechanism and the different frames of the overall chassis (110 parts). The links of the leg mechanism were cut in DC01 steel plates with 1 mm or 2 mm thicknesses, as described in subsection 4.1.1. The outer frames, inner frames and follower gear frames were cut in 2 mm DC01 steel plates, since these parts will be subjected to larger forces. Current literature states that laser cutting steel usually results in higher quality cuts, in terms of cut surface roughness, heat affected zone and detail with respect to stainless steel and aluminium, when cutting materials up to 25 mm [90, 91]. Laser cutting in 1 mm steel, the surface roughness was hardly noticeable (Figure 5.1a), which required little post-processing. On the contrary, laser cutting the different parts in 2 mm steel, resulted in rough edges with thicknesses up to 1 mm (Figure 5.1b).
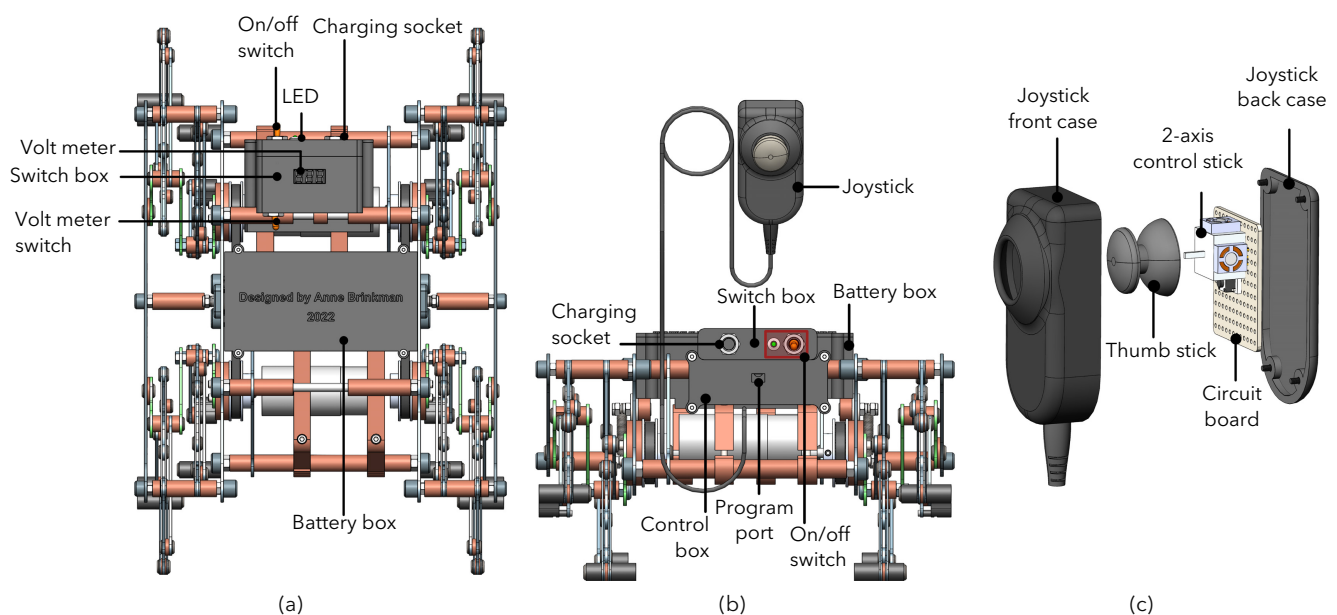
Figure 4.19: (a) Top view of the chassis of the EPWW, in which the battery box was placed in the middle of the chassis; (b) the back view of the chassis of the EPWW, in which the switch box and control box were placed at the back of the chassis; and (c) the different components of the joystick, which were connected to the Arduino Nano in the control box with a 4 m coil cord.
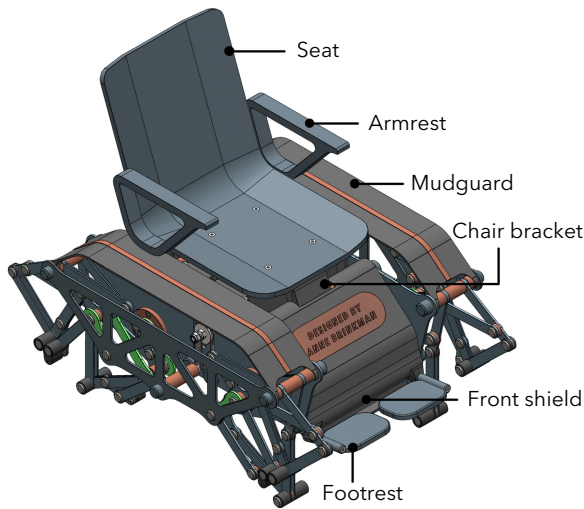
Figure 4.20: The isometric front view of the OctoWalker, in which a chair was placed, consisting of a seat, armrests and footrests. Safety shields were placed at the legs (mudguard) and at the front of the chassis (front shield), to protect the user from the moving components of the EPWW.
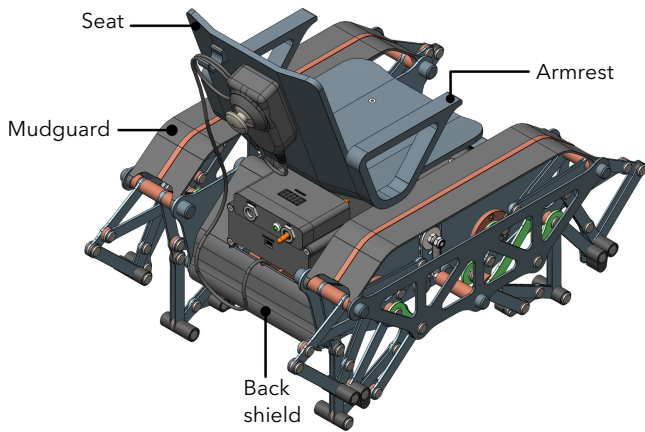
Figure 4.21: The isometric back view of the OctoWalker, in which a chair was placed consisting of a seat, armrests and footrests. Safety shields were placed at the legs (mudguard) and at the back of the chassis (back shield), to protect the user from the moving components of the EPWW.

Additional post-processing was therefore required, in which all the rough edges were first cut and filed.

Furthermore, the OctoWalker should perform in outdoor conditions (FR5), in which moisture can cause corrosion to the steel plates. In order to prevent this from happening in a short period of time, the steel plates were coated with a two component (2K) spray paint and dried for 24 hours on a drying rack, in order to harden the paint [92]. The first components of the leg mechanism that needed to be assembled, were link P, BCDO and N of the inner legs, without additional spacers, in which joint 9 was assembled with a book screw and thread locker; and joint 2 was assembled with a bolt and nut connection. As described in subsection 4.1.2, the lead crank always has to be parallel to the double crank, in order to have a 180° phase between the inner and outer leg. This was achieved by welding the lead crank and double crank to the common rod in joint 2. The spacers for the leg mechanism and the toes and heels of the feet were 3D-printed with PLA using fused deposition modeling (FDM). For the spacers in joint 2 and 9, a slit was made such that the spacers could be pressed on the rods (Figure 5.2). The remaining links for the individual inner and outer legs were assembled, as described in subsection 4.1.1, using book screws at each joint and thread locker inside the book screw connection. Except in joint 7 and 10, since here the toes and heels of the feet were assembled. This resulted in the inner and outer legs, as shown in Figure 5.3. Subsequently, the PLA feet were assembled and rubber bands and rubber heat shrink "shoes" were placed over the feet for shock absorption and preventing slip (Figure 5.3c).

5.2   Gear transmission and chassis

The remaining components, including the inner and outer house of the bearing house, motor clamps, electronic boxes, joystick cases, chair components and safety shields, were 3D-printed with PLA. Before assembling the legs to the inner and outer frame, the outer houses and bearings of the bearing houses were attached to the inner frames (Figure 4.7 and 5.4). Subsequently, each individual leg was lubricated with a polytetrafluoroethylene (PTFE) lubricant, such that the amount of friction between the moving links and book screw joints was minimized and no dust or sand would stick on the moving joints [93, 94]. Each inner leg was first pre-assembled to the outer legs with book screws, thread locker and lubricant. Subsequently, each individual leg pair was assembled to the inner and outer frame with the gear, such that the movement of each leg pair could be pre-tested with a drill, to analyze if the movement was correct and if there were no unwanted friction and noises (e.g. due to too little lubricant). After all the leg pairs were individually tested, all the leg pairs were disassembled from the frames and re-assembled to the outer frames
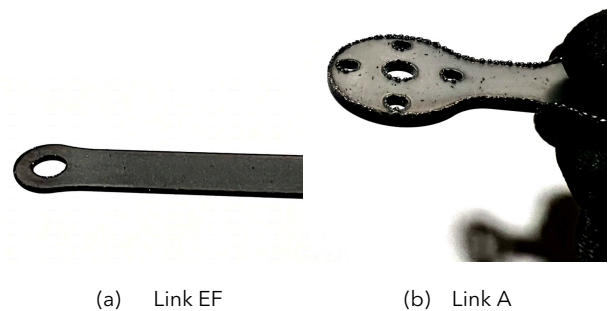
Figure 5.1: Laser cutting always results in a certain degree of surface roughness at the cutting edges. (a) Laser cutting in 1 mm steel, the rough edges were hardly noticeable, while (b) laser cutting in 2 mm steel resulted in rough edges up to 1 mm in height.
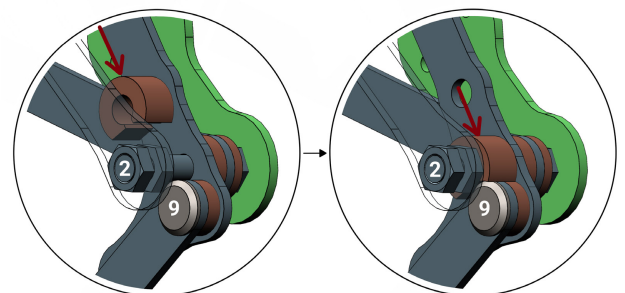
Figure 5.2: After welding the lead crank and double crank to the rod of joint 2, spacers with slits were pushed into the rod of joint 2 and book screw of joint 9, to minimize axial play of link A, BCDO and P.

24

(a)   (b)   (c)
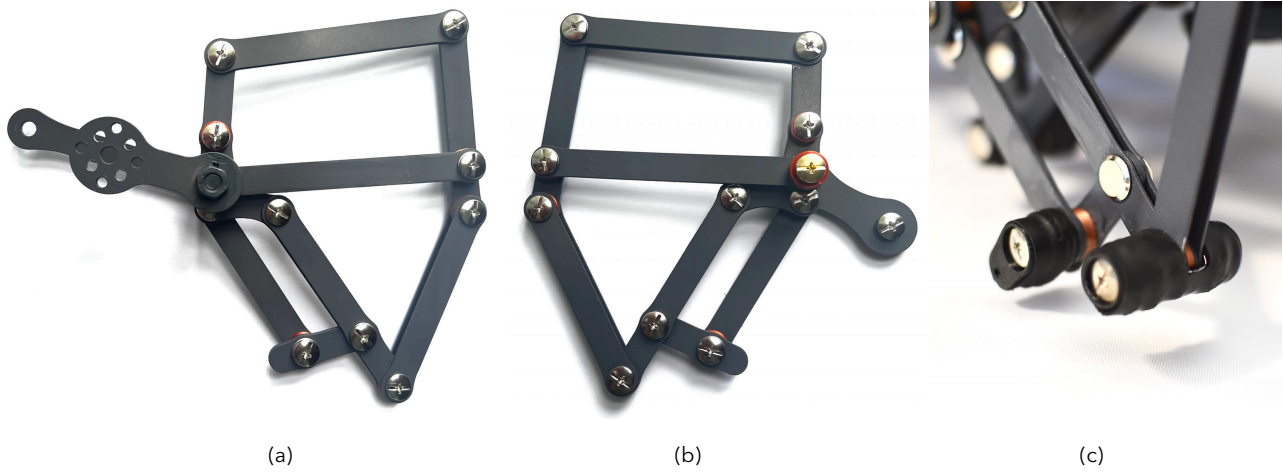
Figure 5.3: The (a) inner and (b) outer legs were first pre-assembled before welding the double crank and applying thread locker to the book screw connections. The last step of building the leg mechanism was placing (c) the toes and heels with rubber bands and rubber heat shrinks for shock absorption and preventing slip.

Figure 5.4: Before assembling the legs to the two inner and outer frames, the bearing houses were assembled to the inner frames. The outer houses and bearings of the bearing houses were attached to the inner frames with three M3 flat-headed bolts and nuts.

with book screws and thread locker. Before fixing the legs to the gears, the timing belt was placed between the two gears. Subsequently, the lead crank of each leg pair was connected to the GT2 gears with the timing belt through the two inner frames and bearing houses. It should be mentioned that the cranks of the hind and front legs of each leg half were assembled with a phase of 180°, such that each leg half would always have two feet on the ground. The belt tensioner was the last part that needed to be assembled to the inner and outer frame, resulting in the final leg half, as shown in Figure 5.5.

Before attaching the DC motors to the leg halves, the legs were again pre-tested with a drill to analyze
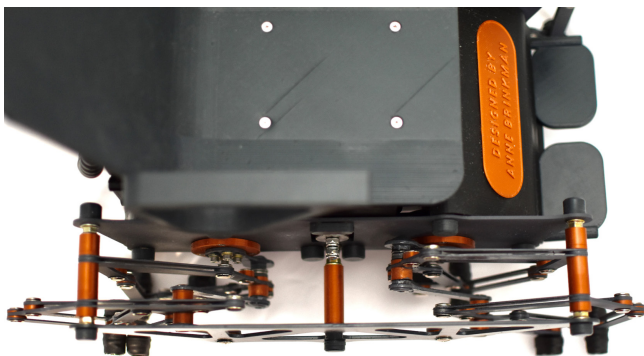
Figure 5.5: Top view of one leg half, which consist of two leg pairs, two bearing houses with gears that are connected with a timing belt, one outer frame, one inner frame and a belt tensioner in between the two leg pairs.

if everything ran smoothly; if enough lubricant was applied; and if there were no unwanted noises due to the legs and gear transmissions. Subsequently, the follower gear frames and DC motors with motor clamps were fixed to the two leg halves and combined to one complete chassis by using four M6 threaded rods. Following this, the electric circuit was build on a breadboard and pre-programmed, which will be described in section 5.3 in more detail. Every component of the circuit was placed in the corresponding box and soldered (Figure 4.19). The battery box was placed between the two DC motors, and the control and switch boxes were placed on top of the hind DC motor. Additionally, tie wraps were used for cable management, such that the cables would not touch the rotating components of the DC motors and gears (Figure 5.6).

The last steps of finalizing the OctoWalker, included placing the chair brackets with the chair to the chassis with two M6 threaded rods; and placing the front and back shield, footrests and mudguards. This resulted in the final 1:3 scaled EPWW prototype, the OctoWalker, as shown in Figure 5.7 and 5.8. The OctoWalker has a total wheelchair depth of 385 mm; wheelchair width of 263 mm;

Figure 5.6: Bottom inside view of the chassis, in which two DC motors are connected to two lead gears; and two follower gears are connected to the follower gear frame. Each lead gear was connected to a follower gear by a timing belt, which is tensioned by a belt tensioner. Tie wraps were used for cable management, such that the cables do not touch the rotating components of the DC motors and gears.

25

Figure 5.7: Front isometric view of the complete OctoWalker, in which the chair, safety shields and mudguards were placed.

Figure 5.8: Back isometric view of the OctoWalker, in which the chair, safety shields, electronic boxes, joystick and mudguards were placed.

wheelchair height of 333 mm; and seat height of 173 mm. The total mass of the prototype is equal to 5.2 kg and the material costs were equal to € 225 (excl. manufacturing costs). In Appendix D.1 more detailed photos of the complete OctoWalker can be found.

5.3   Joystick calibration and steering

After assembling all components, the Arduino was programmed, such that the joystick could control the direction and speed of the DC motors. The joystick is made of two potentiometers that send analog inputs to the Arduino, due to a change in voltage [95]. The joystick must be able to steer in eight different directions, as shown in Figure 5.9. In order to steer forward, the thumb stick has to be pushed upward; and in order to steer backward the thumb stick has to be pushed downward. Pushing the thumb stick to the left or right allows the OctoWalker to spin around its own axis; and the remaining directions allow the OctoWalker to make a smooth forward or backward turn to the left or right.
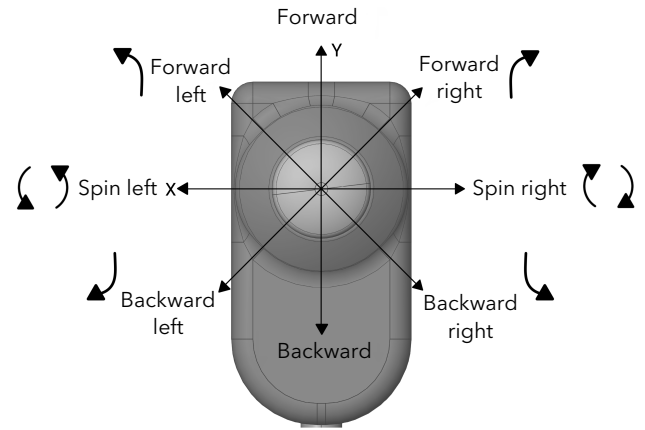
Figure 5.9: All the steering directions of the joystick, in which the EPWW can move forward, backward, spin around its own axis; and can make a smooth forward or backward turn to the left or right.

Theoretically, these joysticks have a value range from 0 to 1023. However, in reality this value range is smaller, due to limitations of the joystick case and the size of the thumb stick. By measuring the Y-axis and X-axis extremes of the joystick, the actual value range of the used joystick could be determined. This resulted in a value range of $j4$ = 150 to $j8$ = 890 for the Y-axis; and $j5$ = 220 to $j7$ = 980 for the X-axis. With these values, different regions could be made such that different steering tasks could be performed (Figure 5.10a). Subsequently, these analog input values were translated to pulse-width modulation (PWM) values from -255 to 255, which corresponded to the speeds of the DC motors (Figure 5.10b). First, a center region bounded by the values $j1$, $j2$, $j3$ and $j6$ was selected in which the EPWW does not move. To prevent motor buzzing an initial minimum speed ($vmin$) was set for all the steering directions, which was equal to -150 or 150, depending on the rotation direction of the motors (Figure 5.10b). The maximum speed ($vmax$) for all steering directions was set to -255 or 255.

In the forward and backward region the left motor (M1) and right motor (M2) had the same speed in the same direction. For the forward steering, $vmin$ was equal to -150 and $vmax$ was equal to -255; while for the backward steering $vmin$ was equal to 150 and $vmax$ was equal to 255. Spinning the EPWW, the motors had the same $vmin$ and $vmax$, but in the opposite direction (+/-). For spin left, M1 had positive PWM values, while M2 had negative PWM values; and for spin right, M1 had negative PWM values, while M2 had positive PWM values. The last regions lay between the forward/backward and spinning steering directions, in which one motor rotates faster with respect to the other motor, allowing for a smooth turn to the right or left (Figure 5.10). In forward left steering, M1 rotates slower with respect to M2. The speed differences between these two motors depend on the position of the thumb stick in the forward left region with respect to the X-axis of the joystick, which has been described in the Arduino code as:

```
float a1 = 1; // minimum variable smooth turn
float a2 = 0.75; // maximum variable smooth turn

...
```

(a)

Y
j4 = 150
forward M1 = M2
j1 = 400
forward left M1 < M2   forward right M1 > M2
center
j5 = 220   spin left M1 = - M2   j2 = 500   M1 = M2 = 0   j3 = 700   spin right - M1 = M2   j7 = 980   X
M1 < M2 backward left   j6 = 600   M1 > M2 backward right
M1 = M2 backward
j8 = 890

(b)

M1 = M2   M1 = M2
Y
$vmax = -255$
forward
M2 = 0.75M1
forward left $vmin = -150$ forward right   M1 = 0.75M2
M1: $vmax$ = 255 / M2: $vmax$ = -255
M1: $vmin$ = 150 / M2: $vmin$ = -150
center
M1: $vmin$ = -150 / M2: $vmin$ = 150
M1: $vmax$ = -255 / M2: $vmax$ = 255
spin left   spin right
M2 = 0.75M1
backward left $vmin = 150$ backward right   M1 = 0.75M2
backward
$vmax = 255$
M1 = M2   M1 = M2

Figure 5.10: The left motor (M1) and right motor (M2) result in different speeds when steering. Different type of steering regions in the joystick consist of forward, backward, forward left/right, backward left/right steering and spinning. In (a) the analog input values of different steering regions are displayed, which has a center region. In this region the EPWW does not move and therefore has a (PWM) speed value of 0. In the forward left/right and backward left/right steering, one motor rotates slower with respect to the other motor. In (b) the different PWM values of the different regions are shown, which correspond to the motor speeds that have been translated from the analog input values of the joystick. For the forward left/right and backward left/right steering, moving the thumb stick further away from the center Y-axis in these regions result in a larger motor speed difference between the two motors.

```
...

// Y-axis forward left ----------------------------------------------
  else if (yAxis < j1 && xAxis < j2){
    // speed motor 1 decreases or increases due to change in X-axis
    int DF = map(xAxis, j2, j5, -a1*vmax, -a2*vmax);
    motor1.setSpeed(map(yAxis,j1,j4,-vmin,DF));
    motor2.setSpeed(map(yAxis,j1,j4,-vmin,-vmax));
  }
```

Steering the thumb stick more to the left side of the forward left region results in a larger motor speed difference between M1 and M2, with as maximum that M1's speed is equal to 0.75M2. This would result in a tighter turn. When steering the thumb more to the right side of the forward left region, the speed difference between these two motors becomes smaller. Similarly, this was also applied in the forward right, backward right and backward left steering; in which M1's speed is larger than M2's speed in the forward and backward right region; and M1's speed is smaller than M2's speed in the backward left steering. These steering principles have been programmed in the Arduino Nano, in which the complete Arduino code used for the OctoWalker can be found in Appendix D.2.

6 Evaluation methods and results

In this section, the performed evaluation methods and results of the technical specifications of the OctoWalker are discussed. An initial test setup is described in section 6.1, which was required in all the performed tests. In total seven tests were executed as described in sections 6.2–6.8.

6.1 Initial test setup

In order to track the motion of the feet and the overall OctoWalker in all the tests, outer toe, heel and frame markers were placed at both sides, as shown in Figure 6.1. Black anti-reflection markers blocked reflections of moving joints which were not tracked. Furthermore, the OctoWalker was placed on a white tiled flat surface with a white background; and an iPhone 13 Pro fixed to a tripod was used as a camera to record all the tests at 60 fps (frames per second).

6.2 Test 1: Static walking

6.2.1 Test setup and protocol

In the static walking test, the foot trajectories of the OctoWalker at a fixed position were analyzed. In Figure 6.2 the test setup of the static walking test is shown. The OctoWalker was fixated by a chair support, such that the legs could move freely at a fixed position. A ruler fixed to the outer frame was used to calibrate the measured data.
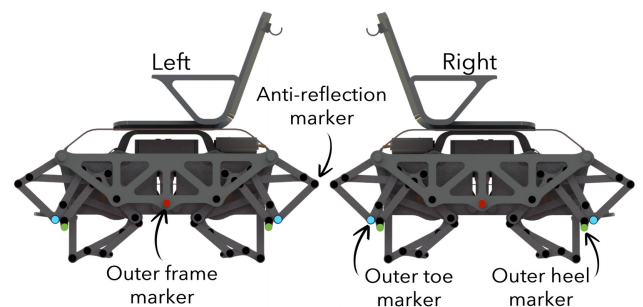
Figure 6.1: Initial test setup for left and right side of the OctoWalker. Red outer frame markers, blue outer toe markers and green outer heel markers tracked the motion of the OctoWalker; and black anti-reflection markers blocked reflections of joints that were not tracked.
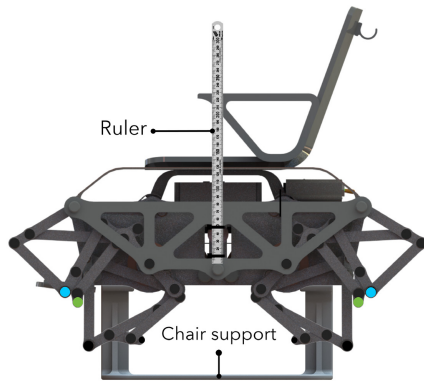
Figure 6.2: Test setup for the left side of the static walking test (T1), in which the OctoWalker was fixated on a chair support; allowing the legs to move freely at a fixed position; and a ruler was fixed to the outer frame for calibration of the recorded videos.

The tasks performed in the static walking test are shown in Table 6.1. The legs of the OctoWalker moved forward at maximum speed for 30 s by moving the joystick forward; while doing this the movement of the left feet were recorded. Subsequently, the legs of the OctoWalker moved forward again at maximum speed for 30 s; while doing this the movement of the right feet were recorded.

Table 6.1: Test protocol for the static walking test (T1), which recorded the left and right foot trajectories at a fixed position.

Task	Joystick input[1]	Time (s)	Record[2]
T1.1	Forward	30	Left feet
T1.2	Forward	30	Right feet

[1]: At maximum speed.
[2]: Calibration ruler was fixed at the recorded side.

6.2.2 Results

The recorded videos were first processed in Kinovea, in which the x- and y-coordinates of the trajectory pad of the toe and heel markers were measured. In MATLAB eight cycles from the measured data were further processed, in which initial rise time was removed. The foot trajectories of the left and right outer feet were compared to the theoretical gait, as described in subsection 4.1.1 (Figure 6.3). A zero-phase low pass filter with a cut off
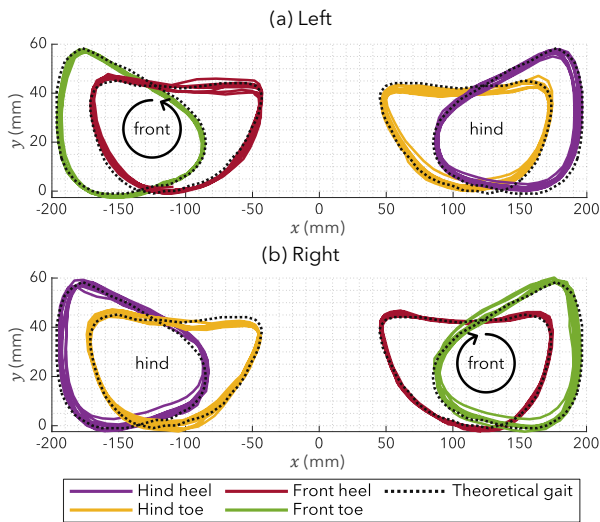
Figure 6.3: Foot trajectory results of the static walking test (T1) with (a) the foot trajectories of the left outer feet, with a counter clock wise rotation as forward motion; and (b) foot trajectories of the right outer feet, with a clock wise rotation as forward motion.

frequency of 7.5 Hz and sample rate of 60 was applied to the velocity data by using the "filtfilt" function, which removed the noise of the raw measurements [96, 97]. Numerical results of the minimum and maximum absolute speeds, phase shifts and motor speeds are shown in Table 6.2. The graphical results of the absolute speeds with respect to time of the left and right feet are shown in Figure 6.4. The left and right speed results with respect to the position of the foot trajectories are shown in Figure 6.5. The minimum foot speeds were reached for both, left and right, sides when the heels almost reached their maximum height. The maximum foot speeds were reached for both sides after the heels reached their maximum height and started to move in a horizontal motion. Further results of the position and velocity can be found in Appendix E.1.

Table 6.2: Absolute foot speeds, phase shifts, motor speeds and time cycle results of the static walking test (T1). The left and right side had similar results for the minimum and maximum speeds, while the phase shift, motor speed and mean cycle time were not similar.

		$v_{f,min}$[1] (m/s)	$v_{f,max}$[2] (m/s)	Φ[3] (°)	v_m[4] (RPM)	T_m[5] (s)
Left	Toes	0.23	0.91	44	102.4	0.59
	Heels	0.15	1.03			
Right	Toes	0.23	0.91	54	100.6	0.60
	Heels	0.16	1.04			

[1]: Minimum absolute toe and heel speed; [2]: Maximum absolute toe and heel speed; [3]: Phase shift hind feet with respect to front feet; [4]: Mean motor speed of n = 8 cycles; [5]: Mean cycle time.

6.3 Test 2: Straight unloaded walking
6.3.1 Test setup and protocol
In the straight unloaded walking test, the foot trajectories and vertical displacements of the OctoWalker were
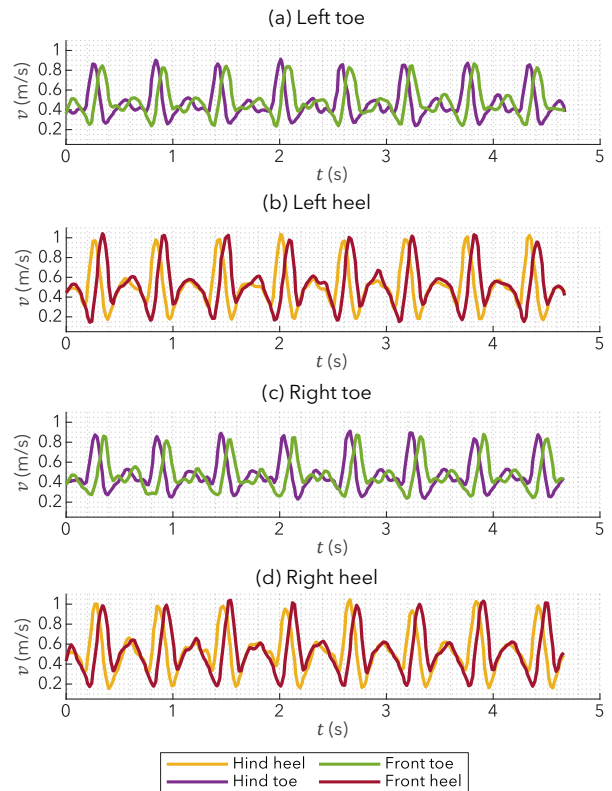
Figure 6.4: Absolute speeds with respect to time results of the static walking test (T1), with (a) the front and hind left toes; (b) the front and hind left heels; (c) the front and hind right toes; and (d) the front and hind right heels.
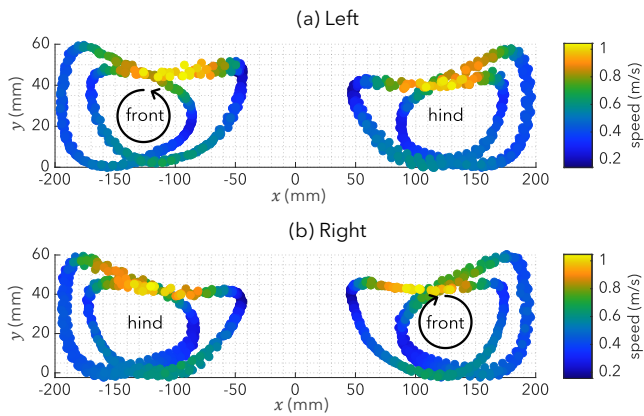
Figure 6.5: Absolute speeds with respect to the foot trajectories of the static walking test (T1), with (a) the left front and hind foot trajectories; and (b) the right front and hind foot trajectories.

analyzed while walking a straight line on a flat tiled surface without additional payload. Two lines were marked with tape at a flat surface, which indicated the start and finish of a 1 m walking path; and were used to calibrate the measured data (Figure 6.6). The camera was placed 2.5 m from the walking path, which was the maximum distance the camera was still able to identify the tracking markers.

The tasks performed in the straight unloaded walking test are shown in Table 6.3. The OctoWalker was placed at the starting position, in which the hind inner legs were placed on the starting line (Figure 6.6). The OctoWalker moved forward in a straight line at maximum speed until the front inner legs reached the finish line; while doing this the movement of the right side of the OctoWalker was recorded. This walking cycle was repeated five times.

Table 6.3: Test protocol for the straight unloaded walking test (T2), which recorded the right foot trajectories over a walking path of 1 m.

Task	Joystick input[1]	Distance (m)	# cycles[2]
T2.1	Forward	1	5

[1]: At maximum speed.
[2]: Number of repetitions.

6.3.2 Results

The recorded videos were first processed in Kinovea, in which the x- and y-coordinates of the trajectory pad of the right outer toe, heel and frame markers were measured. In MATLAB the measured data were further processed. The mean measured results of the markers with respect to the starting position of the five cycles are shown in Figure 6.7. Numerical results of the vertical displacement (Δy_{frame}), step heights (Δy_{heel} and Δy_{toe}) and step lengths (Δx_{heel} and Δx_{toe}) of all the cycles combined are shown in Table 6.4. The vertical fluctuations of the outer frame marker were
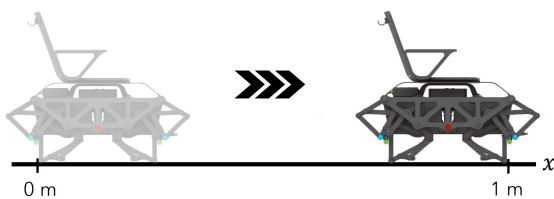
Figure 6.6: Test setup of the straight unloaded walking test (T2), in which the OctoWalker walked a straight line on a flat tiled surface. Two lines were marker with tape, which indicated the start and finish.
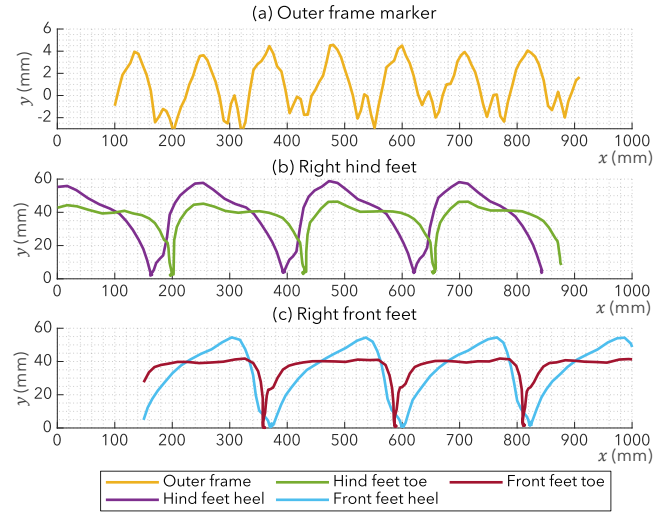
Figure 6.7: The mean foot trajectory results (n = 5) of the straight unloaded walking test (T2) with (a) vertical fluctuations of the right outer frame marker; (b) the foot trajectories of the right hind toe and heel; and (c) the foot trajectories of the front toe and heel.

determined by the difference between the local maximum vertical fluctuations of the outer frame marker were determined by the difference between the local maximum and minimum of the outer frame marker at each performed step. The step height of the feet were determined by the difference between the local maximum and minimum of the feet at each performed step. The step length of the feet were determined by the difference of the local minimum of the feet at each performed step.

A zero-phase low pass filter with a cut off frequency of 7.5 Hz and sample rate of 60 was applied to the velocity and acceleration data by using the "filtfilt" function, which removed the noise of the raw measurements [96, 97]. The mean vertical velocity, horizontal velocity and acceleration of the five cycles are shown in Figure 6.8.

Table 6.4: Results of the straight unloaded walking test (T2), with the outer frame vertical displacement (Δy_{frame}), heel and toe step heights (Δy_{heel} and Δy_{toe}) and heel and toe step lengths (Δx_{heel} and Δx_{toe}) results of all the five cycles combined.

(mm)	Δy_{frame}	Δy_{heel}	Δy_{toe}	Δx_{heel}	Δx_{toe}
Median[1]	8.4	42	54	226	225
IQ1[3]	7.8	40	53	222	223
IQ3[4]	9.2	44	55	228	229
IQR[5]	1.4	4.0	2.2	6.5	6.1
Min.[6]	7.2	38	51	215	217
Max.[7]	11	47	55	234	234

[1]: Median; [2]: Lower quartile; [3]: Upper quartile; [4]: Interquartile range; [5]: Whisker minimum; [6]: Whisker maximum.

The mean cycle time (T_{m}) resulted in 3.0 s. The horizontal velocities of five cycles combined resulted in a mean rise time (t_{r}) of 0.12 s reaching a mean horizontal velocity of 0.44 m/s. The vertical velocity of five cycles combined ranged between -0.080 m/s and 0.078 m/s, resulting in an absolute mean vertical velocity of 0.033 m/s. The horizontal acceleration of five cycles combined resulted in an initial mean peak acceleration of 3.39 m/s² which settled to a mean horizontal acceleration of -0.024 m/s² and decelerated to -1.80 m/s². Further results of the positions, velocities and accelerations can be found in Appendix E.2.
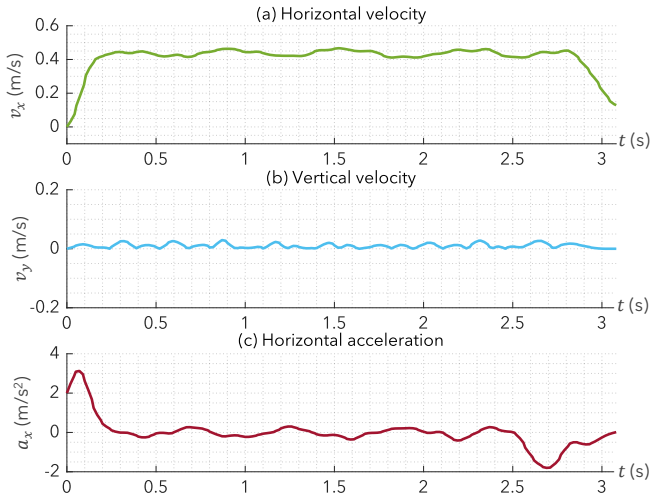
Figure 6.8: (a) The mean horizontal velocity, (b) vertical velocity and (c) horizontal acceleration results of the straight unloaded walking test (T2) of all the five cycles combined.

6.4 Test 3: Steering
6.4.1 Test setup and protocol
In the steering test, the steering radius of the OctoWalker was analyzed when rotating 360° on a flat tiled surface. In Figure 6.9 the starting position of the OctoWalker is shown, in which the OctoWalker always started faced up. A red chair marker was placed at the center of the chair to track the rotation of the OctoWalker during steering; and a black cross behind the chair marker was used to calibrate the measured data. The camera was placed 1 m above the OctoWalker.

The tasks performed in the steering test are shown in Table 6.5. During left steering the OctoWalker rotated 360° counter clock wise at maximum speed by moving the joystick to left. During right steering the OctoWalker rotated 360° clock wise at maximum speed by moving the joystick to right. Both steering cycles were repeated 15 times and while doing this the movement of the chair marker was recorded.

Table 6.5: Test protocol for the steering test (T3), which recorded the chair marker trajectories when rotating 360° to left and right.

Task	Joystick input[1]	Steering rotation[2]	# cycles[3]
T3.1	Left	CCW	15
T3.2	Right	CW	15

[1]: At maximum speed; [2]: OctoWalker rotates 360° counter clock wise (CCW) or clock wise (CW); [3]: Number of repetitions.
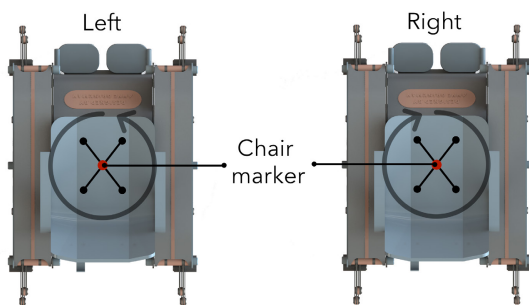
Figure 6.9: Test setup of the steering test (T3), in which the OctoWalker rotated on a flat tiled surface. A chair marker was placed to analyze the turning radius.

6.4.2 Results
The recorded videos were first processed in Kinovea, in which the x- and y-coordinates of the trajectory pad of the chair marker were measured. In MATLAB the measured data were further processed. The maximum turning circles were determined by combining the boundary areas of each individual turning circle. Steering to the left resulted in a maximum turning radius of 100 mm with a turning circle center point at (17 mm, -19 mm) (Figure 6.10). The numerical results of the turning radii, cycle times and angular speeds of the 15 individual cycles are shown in Table 6.6.

Steering to the right resulted in a maximum turning radius of 121 mm with a turning circle center point at (15 mm, -74 mm) (Figure 6.11). The numerical results of the turning radii, cycle times and angular speeds of the 15 individual cycles are shown in Table 6.7. More extensive results of the individual turning circles can be found in Appendix E.3.

Table 6.6: Left steering results of the steering test (T3) of the turning radii of individual cycles (R_{ind}), distance between the (0,0) starting point to the end point ($d_{0,end}$), maximum distance from the starting point (d_{max}), cycle time for one rotation (T_c), and mean angular speed of each cycle (ω_{st}).

	R_{ind} (mm)	$d_{0,end}$ (mm)	d_{max} (mm)	T_c (s)	ω_{st} (rad/s)
Median[1]	36	34	54	4.15	1.51
IQ1[2]	29	29	36	4.05	1.49
IQ3[3]	40	64	70	4.22	1.55
IQR[4]	11	35	34	0.17	0.06
Min.[5]	18	2.5	28	3.86	1.49
Max.[6]	47	93	93	4.22	1.63

[1]: Median; [2]: Lower quartile; [3]: Upper quartile; [4]: Interquartile range; [5]: Whisker minimum; [6]: Whisker maximum.
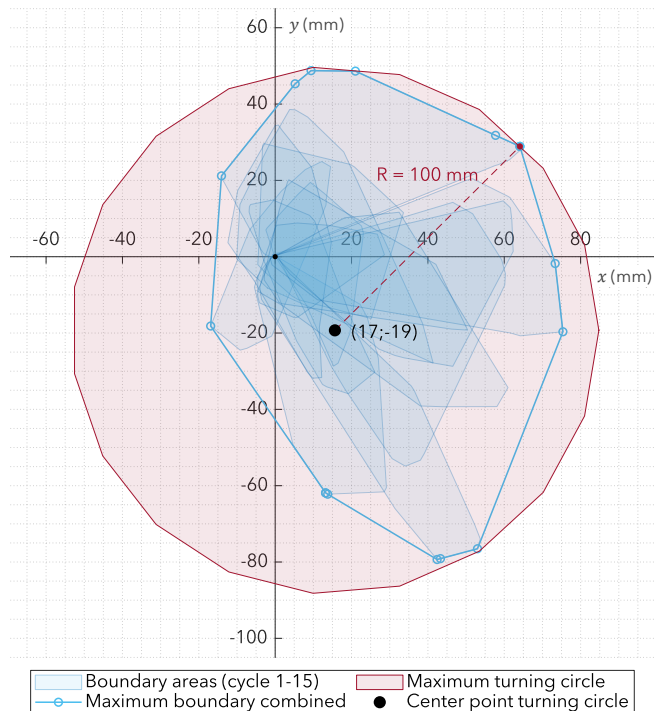
Figure 6.10: Left steering results of the steering test (T3) of the maximum turning circle, turning radius (R) and center point of the turning circle results of all the 15 cycles combined.
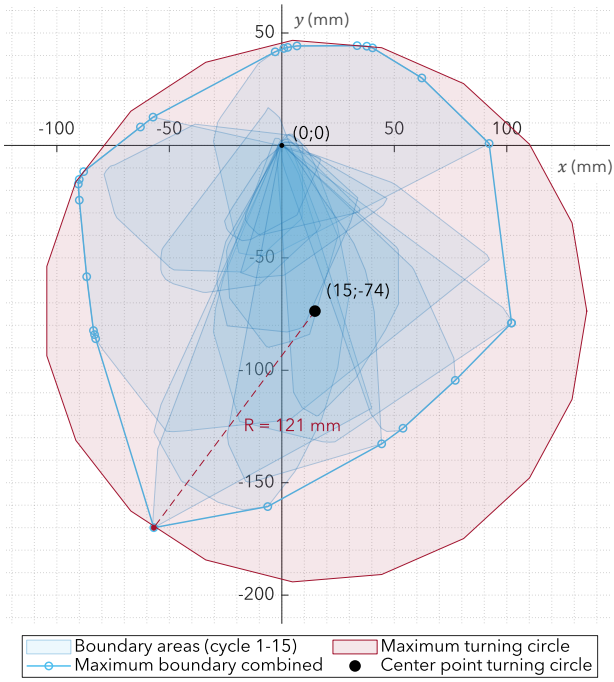
Figure 6.11: Right steering results of the steering test (T3), with the maximum turning circle, turning radius (R) and center point of the turning circle results of all the 15 cycles combined.

Table 6.7: Right steering results of the steering test (T3) of the turning radii of individual cycles (R_{ind}), distance between the (0,0) starting point to the end point ($d_{0,end}$), maximum distance from the starting point (d_{max}), cycle time for one rotation (T_c), and mean angular speed of each cycle (ω_{st}).

	R_{ind} (mm)	$d_{0,end}$ (mm)	d_{max} (mm)	T_c (s)	ω_{st} (rad/s)
Median[1]	64	86	92	4.89	1.29
IQ1[2]	44	40	79	4.83	1.22
IQ3[3]	76	104	137	5.15	1.30
IQR[4]	31	64	58	0.32	0.08
Min.[5]	27	3.6	45	4.41	1.20
Max.[6]	95	130	179	5.26	1.35

[1]: Median; [2]: Lower quartile; [3]: Upper quartile; [4]: Interquartile range; [5]: Whisker minimum; [6]: Whisker maximum.

6.5 Test 4: Payload
6.5.1 Test setup and protocol
In the payload test, the speed changes and vertical fluctuations were analyzed, when walking a straight line on a flat tiled surface with additional payload. In total five 1 kg dumbbells were used as payload which were fixed horizontally to the chair and stacked as shown in Figure 6.12. Similar to the straight unloaded walking test (6.3.1), two lines were marked with tape at the flat surface, indicating the start and finish of a 1 m walking path, This was used to calibrate the measured data (Figure 6.6). The camera was placed 2.5 m from the walking path.

The tasks performed in the payload test are shown in Table 6.8. The OctoWalker was placed at the starting position with 1 kg on the chair, in which the hind inner legs were placed on the starting line. The OctoWalker moved forward in a straight line at maximum speed until the front inner legs reached the finish line. This walking cycle was repeated three times. Similarly, these steps where also repeated for a payload of 2-5 kg, with increments of 1 kg dumbbells as shown in Figure 6.12.

Figure 6.12: Dumbbell stacking for the payload test (T4) with each dumbbell weighing 1 kg. The numbers indicate the order, in which the dumbbells were stacked and fixed to the chair.

Table 6.8: Test protocol for the payload test (T4), which recorded the right side markers over a walking path of 1 m with additional payload.

Task	Joystick input[1]	Distance (m)	Payload (kg)	# cycles[2]
T4.1	Forward	1	1	3
T4.2	Forward	1	2	3
T4.3	Forward	1	3	3
T4.4	Forward	1	4	3
T4.5	Forward	1	5	3

[1]: At maximum speed; [2]: Number of repetitions.

6.5.2 Results
The recorded videos were first processed in Kinovea, in which the x- and y-coordinates of the trajectory pad of the right outer frame marker were measured. In MATLAB the measured data were further processed. The mean measured results of the outer frame marker with respect to the starting position of three cycles for each payload are shown in Figure 6.13. The boxplot results of the vertical displacement ($\Delta y_{max,min}$) of all the payloads combined are shown in Figure 6.14. The vertical displacements of the right outer frame marker were determined by the difference between the local maximum and minimum at each performed step.

A zero-phase low pass filter with a cut off frequency of 7.5 Hz and sample rate of 60 was applied to the velocity and acceleration data by using the "filtfilt" MATLAB [96, 97]. The mean horizontal velocity and mean horizontal acceleration results of the different payloads are shown in Figure 6.15. After the initial acceleration the horizontal velocity resulted in a constant median velocity of 0.42 m/s (1 kg) to 0.43 m/s (5 kg) (Figure 6.16). The numerical results of the initial acceleration, maximum acceleration, rise time and cycle time are shown in Table 6.9. Further results of the positions and velocities can be found in Appendix E.4.
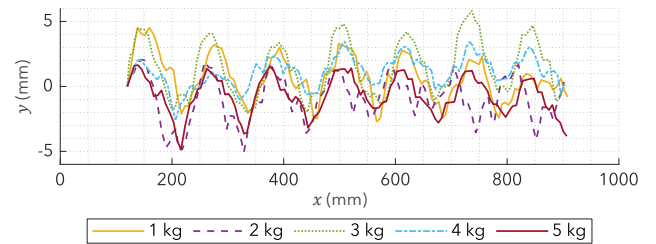
Figure 6.13: The mean position results (n = 3) of the payload test (T4) with vertical fluctuations of the right outer frame marker at each payload.
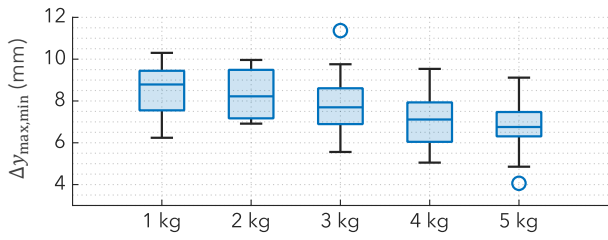
Figure 6.14: Boxplot results of vertical displacements ($\Delta y_{\text{max,min}} = y_{\text{max}} - y_{\text{min}}$) of the right outer frame marker in the payload test (T4) at different payloads (n = 3).
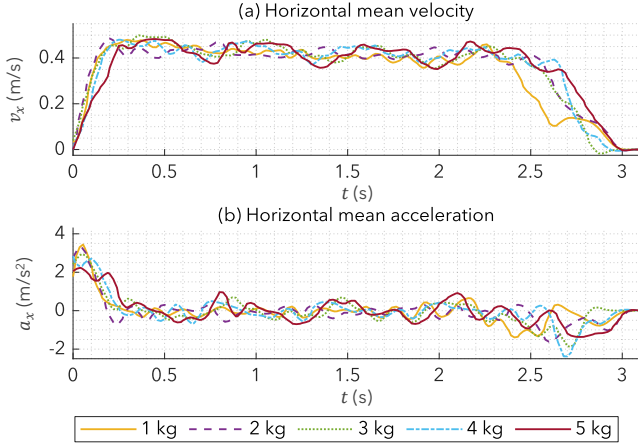
Figure 6.15: (a) The horizontal mean (n=3) velocity and horizontal mean (n=3) acceleration results of the payload test (T4) for payloads 1-5 kg.
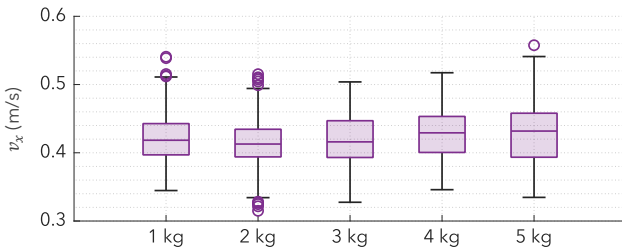
Figure 6.16: The horizontal constant velocity results of the payload test (T4) of all three cycles combined. Only the velocity results from t_{start} = 0.5 s until t_{end} = 2.0 s were extracted.

Table 6.9: Numerical mean (n = 3) results of the initial maximum acceleration (a_{max}), rise time (t_{r}) and cycle time (T_{c}) of the payload test (T4) for different payloads.

Payload (kg)	1	2	3	4	5
a_{max} (m/s^2)[1]	3.44	3.31	2.95	2.71	2.23
t_{r} (s)[2]	0.14	0.13	0.14	0.16	0.22
T_{c} (s)[3]	3.03	2.98	2.97	2.95	3.02

[1]: Maximum mean horizontal acceleration; [2]: Mean rise time; [3]: Mean cycle time.

6.6   Test 5: Static battery
6.6.1   Test setup and protocol
In the static battery test, the battery voltage and angular speed of the motors were analyzed. The voltage meter build in the OctoWalker was used to measure the battery voltage. Before starting the test, the battery was fully charged. Similarly to the static walking test, the OctoWalker was fixed to a chair support such that the legs could move freely at a fixed position (Figure 6.2).

The tasks performed in the static battery test are shown in Table 6.10. The legs of the OctoWalker moved forward at a fixed position at maximum speed in cycles of 10 minutes, in order to prevent overheating of the motors and Arduino. While doing this, the movement of the right side of the OctoWalker was recorded. Between every two cycles the OctoWalker received a cooling down time of 15 minutes. These tasks were repeated until the battery ran out.

Table 6.10: Test protocol for the static battery test (T5), which measured the output voltage at a fixed position.

Task[1]	Joystick input[2]	Time (minutes)
T5.1	Forward	10
T5.2	Center[3]	15

[1]: Tasks repeated until battery ran out.
[2]: At maximum speed.
[3]: Cooling down time.

6.6.2   Results
The recorded videos were first processed in Kinovea, in which the cycle time (T_{m}) of each motor rotation was determined. The measured data of the voltage meter and the cycle time data were further processed in MATLAB. The results of the measured voltage are shown in Figure 6.17a. The data consisted of three phases: the initial phase (I), the mid phase (II) and the end phase (III); in which the cooling down time was removed. For a fully charged battery, the measured voltage meter was 6.93 V. After 34 minutes and 39 seconds, the last voltage was measured (4.06 V) and the motor stopped running. The motor speed was determined by the reciprocal of the measured cycle time, which are shown in Figure 6.17b. The initial measured motor speed resulted in 120 RPM and the final measured motor speed resulted in 72 RPM. Furthermore, using the measured step length results (226 mm) in the straight unloaded walking test (6.3.2) the maximum travelled distance (766 m) and maximum horizontal walking velocity (0.45 m/s) was determined (Figure 6.18). The battery had a capacity of 3.40 Ah when fully charged, which could provide an average current (I_{avg}) of 5.88 A for 34 minutes and 39 seconds. The average calculated power consumption (P_{avg}) resulted in 32 W during the static battery test, which resulted in a calculated energy consumption of 3985 kJ.
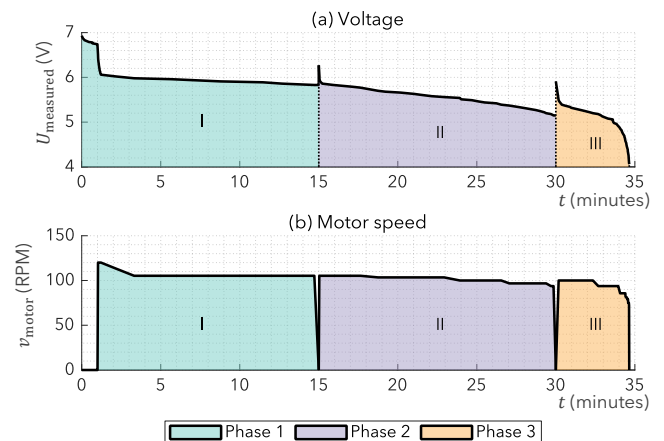
Figure 6.17: The (a) measured output voltage and (b) motor speed results of the static battery test (T5) divided into three phases, in which the cooling down time was removed.
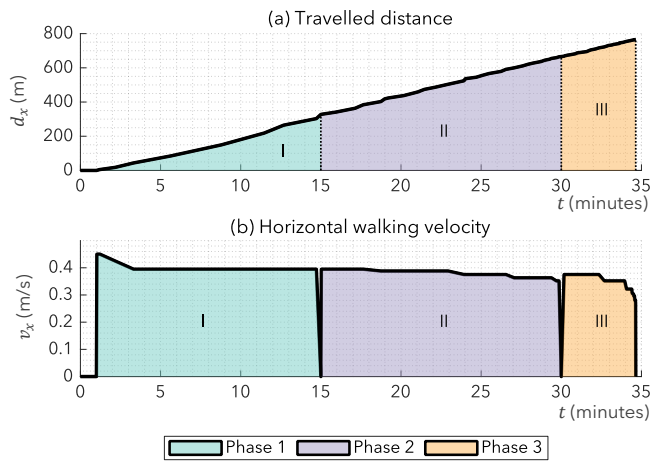
Figure 6.18: (a) Predicted travelled distance and (b) horizontal walking velocity results of the static battery test (T5) divided into three phases, in which the cooling down time was removed.

6.7 Test 6: Sidewalk step
6.7.1 Test setup and protocol
In the sidewalk step test, the foot trajectories of the right outer feet were analyzed, while walking on a step at different starting distances from the step. A wooden platform was build to mimic an 1:3 scaled sidewalk and slope according to the requirements in subsection 2.3.3 (Figure 6.19). For the sidewalk step test only the left side of the wooden platform was required, which had a step height of 50 mm. The dimensions of the wooden platform were used to calibrate the measured data. The camera was placed 1.5 m from the walking path.

The tasks performed in the sidewalk step test are shown in Table 6.11. The OctoWalker was placed at the starting position, in which the front inner toes were placed at a specific distance from the step as described in Table 6.11. and Figure 6.19. The OctoWalker moved forward at its minimum speed until all eight legs reached the flat top of the wooden platform.

6.7.2 Results
The recorded videos were first processed in Kinovea, in which the x- and y-coordinates of the trajectory pads of the outer right toes and heels were measured. In MATLAB the measured data were further processed. The foot trajectory results of each starting distance are shown in Figure 6.20. The OctoWalker was able to walk on the step at all the

Table 6.11: Test protocol for the sidewalk step test (T6), which recorded the right side markers while walking over a wooden step with a step height of 50 mm.

Task	Joystick input[1]	Distance[2] (mm)
T6.1	Forward	120
T6.2	Forward	100
T6.3	Forward	80
T6.4	Forward	60
T6.5	Forward	40

[1]: At minimum speed.
[2]: Distance with respect to step.

starting distances, however starting distances of 60 mm up to 120 mm collided with the front toes against the step before it continued walking. At a starting distance of 40 mm no collisions with the front toes occurred, instead collisions with the hind feet and legs occurred.

In Figure 6.21 the locations of the collisions between the wooden platform and feet of each starting distance are shown. The starting distance of 40 mm had one collision with the hind legs. In general, the feet collided at a median of 45 mm with an IQR of 5.9 mm, a minimum of 37 mm and maximum of 50 mm with two outliers at y_{feet} = 22 mm and y_{feet} = 14 mm.

6.8 Test 7: Slope walking
6.8.1 Test setup and protocol
In the slope walking test, the foot trajectories of the right outer front toe and outer frame marker were analyzed while walking on a slope without and with additional payload. A wooden platform was build to mimic an 1:3 scaled sidewalk and slope according to the requirements in subsection 2.3.3 (Figure 6.19). For the slope walking test only the right side of the wooden platform was required, which had a slope of 28°. The dimensions of the wooden platform were used to calibrate the measured data. Similar to the payload test (6.5.1), five 1 kg dumbbells were used as payload, which were fixed horizontally to the chair and stacked as shown in Figure 6.12. The camera was placed 1.5 m from the walking path.

The tasks performed in the slope walking test are shown in Table 6.12. In the first task (T7.1) no payload was fixed to the chair. The OctoWalker walked over the slope at its minimum speed until all eight legs reached the flat top of the wooden platform. In the second task (T7.2) a payload of 1 kg was fixed to the chair when walking over the slope.
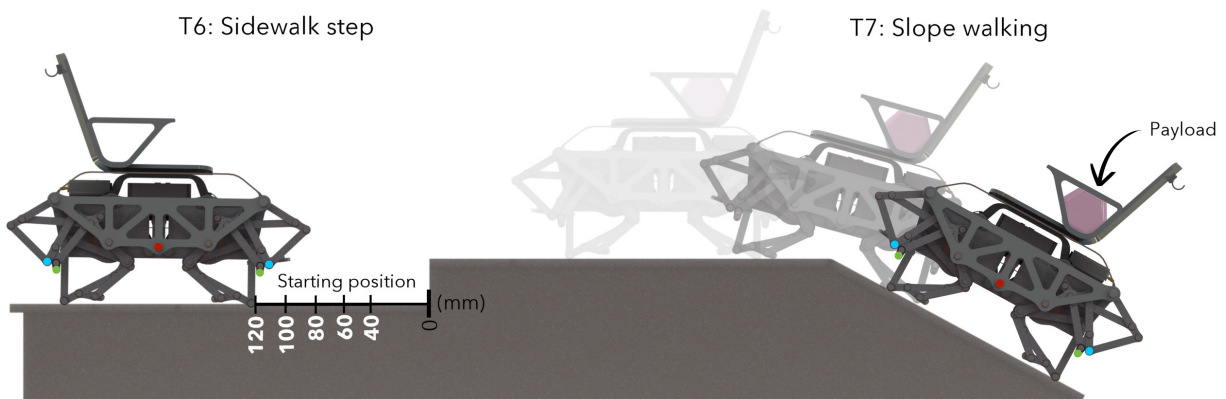
Figure 6.19: Wooden platform for the test setups of the sidewalk step test (left) and slope walking test (right), with (T6) a 50 mm step and markers indicating different starting positions; and (T7) a slope of 28° with a payload fixed to the chair.
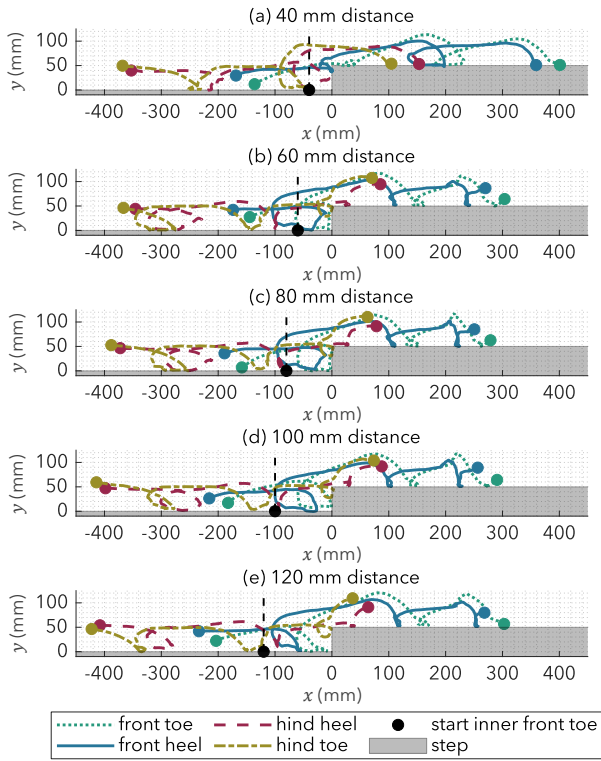
Figure 6.20: The right outer foot trajectories of the sidewalk step test (T6) at different starting distances with respect to the wooden step: (a) 40 mm, (b) 60 mm, (c) 80 mm, (d) 100 mm and (e) 120 mm.
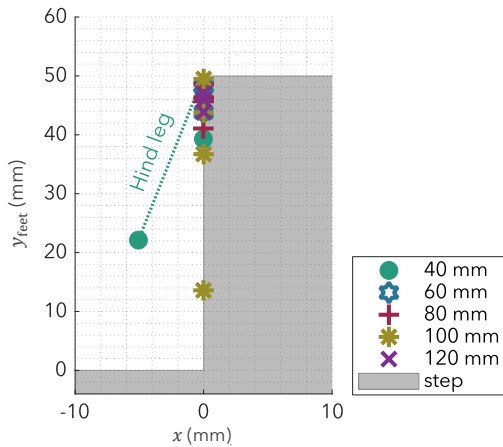
Figure 6.21: The collision locations (y_{feet}) of the right inner and outer foot trajectories of the sidewalk step test (T6) at different starting distances. At 40 mm one collision with the right outer hind leg occurred.

Similarly, these steps where also repeated for a payload of 2-5 kg, with increments of 1 kg dumbbells as shown in Figure 6.12.

Table 6.12: Test protocol for the slope walking test (T7), which recorded the right side markers while walking over a wooden slope with a slope angle of 28°.

Task	Joystick input[1]	Payload (kg)
T7.1	Forward	0
T7.2	Forward	1
T7.3	Forward	2
T7.4	Forward	3
T7.5	Forward	4
T7.6	Forward	5

[1]: At minimum speed.

6.8.2   Results

The recorded videos were first processed in Kinovea, in which the x- and y-coordinates of the trajectory pads of the outer front toes and outer frame markers were measured. In MATLAB the measured data were further processed. A zero-phase low pass filter with a cut off frequency of 7.5 Hz and sample rate of 60 was applied to the velocity data by using the "filtfilt" MATLAB function [96, 97]. The foot trajectories at each payload are shown in Figure 6.22. The OctoWalker was able to walk over the slope without a payload and with payloads of 1 kg and 2 kg in four steps. However, at a payload of 3 kg the front feet started to lift from the platform, reaching a maximum speed of 0.68 m/s. Therefore, the tasks T7.4 until T7.6 were not performed.

7   Discussion
7.1   System verification
7.1.1   Dimensions and mass

The seat, backrest, armrest, footrest and wheelchair depth (385 mm) of the OctoWalker were designed according to the dimensional constraints of the EPWW in section 2.3.2. The wheelchair width of the prototype (263 mm) was larger than the maximum width of 233 mm (C5). This would mean that a true-scaled EPWW would not fit through a normal sized entrance (~800 mm), which was perceived as one of the issues for wheelchair users with current wheelchairs [40, 98]. In this scaled prototype this additional width was caused due to the dimensional constraints of the DC motors, electronic components and the limited space for the legs between the inner and outer frames due to the limitations in joint connections. Furthermore, the OctoWalker had a total weight of 5.2 kg and was tested with payloads up to 5 kg for straight walking (C2), which resulted in a payload-to-mass-ratio (PM-ratio) of 0.96. The speeds remained similar, while the initial acceleration decreased when increasing the payload. The OctoWalker could therefore lift a human adult up to 135 kg in a true-scaled EPWW, which is 1.4 to 1.9 times larger than current existing leg-based EPWs [99, 100]. The actual maximum PM-ratio on a flat surface could not be determined, due to the limited space on the wheelchair seat.

7.1.2   Step height and step length

The static foot trajectory of the modified mechanism had a maximum mean toe and heel step height of 57 mm and
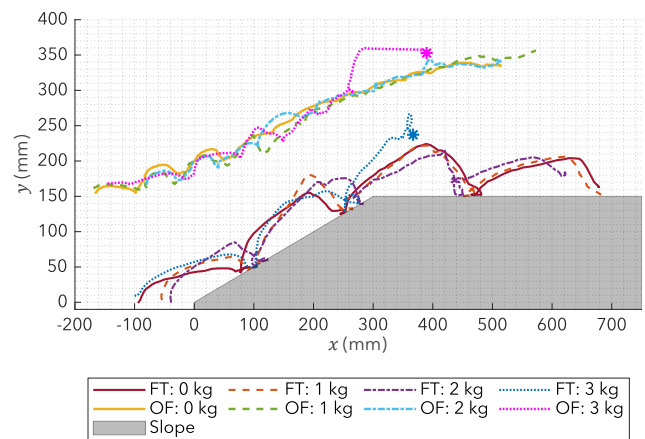
Figure 6.22: Right outer front toe (FT) and outer frame marker (OF) trajectory results of the slope walking test (T7). The OctoWalker was tested with payloads up to 3 kg.

46 mm. When considering a true-scaled EPWW, this would be larger than majority of the walking robots with a closed-chain mechanism [101-105]. The maximum measured step height of the toes and heels dropped to 54 mm and 42 mm when walking on a flat surface without additional payload (C18). This was caused due to the gravity force of the weight of the OctoWalker itself, that pushed the clearance between the different moving components and joint connections towards the walking surface. Moreover, the maximum step lengths for the toes and heels increased to 226 mm and 225 mm (C19), which is larger than currently existing true-scaled leg-based EPWs [13, 99, 100]. The vertical unloaded fluctuations of the OctoWalker was equal to 8.4 mm, in which the vertical fluctuations decreased to 6.6 mm when increasing the payload, resulting in a more stable walking EPWW. Translating these results to a true-scaled EPWW, would result in vertical fluctuations of 19 mm to 25 mm, which is smaller than trunk vertical displacements of human adults walking (~45 mm) [105] and horse walking (~53 mm) [107].

7.1.3   Curb climbing and slope climbing
Walking on a scaled curb caused the legs and feet to collide with the curb at different points. The majority of the results showed, that a collision occurred between a step height of 37 mm and 50 mm. This means that in order to achieve a practical step height of 50 mm, both the step heights of the toes and heels should become a minimum of 1.45 times larger to decrease the probability of collisions with the obstacles. This could otherwise cause damage to the legs and feet, such as deformation of the different links and faster corrosion due to removal of the coating of the steel links. The initial leg configuration of the OctoWalker before walking the obstacle could also increase the risks of collisions between the obstacles and legs. The front and hind feet had the same gait pattern. However, for both the left and right side, a phase difference between the front and hind legs was measured (left = 44°; right = 54°), which also resulted in not always having four feet on the ground. This was caused due to the initial assembling of the gear transmission to the leg halves and the deflection force of the belt tensioner, in which the front and hind lead cranks did not exactly have a phase of 180° when assembling the legs to the gears.

Furthermore, the OctoWalker was able to walk on slopes up to 28°, in which a maximum payload of 2 kg was possible at 28° (C21). At a payload of 3 kg the driver lost control, leading to lifting the front legs of the EPWW, which was caused due to the center of gravity (COG) not being low enough [11]. In order to climb higher slopes, stability control should be implemented into the EPWW, which prevents the user from tipping or falling when walking on slopes [11]. Standard EPWs, without stability control features, have a tipping angle anywhere from 2° to 14° [108]. The slope climbing results of the OctoWalker are therefore almost comparable to EPWs with stair-climbing features without the need for active stability control [109-111]. This reduces the control complexity and costs of an EPWW with respect to current EPWs.

7.1.4   Speed and acceleration
The static motor speed of the left motor was equal to 102.4 RPM, while the right motor speed was equal to 100.6 RPM, resulting in a speed difference of 1.8 RPM. This caused a slight deviation to the right when trying to walk in a straight line. The maximum measured unloaded horizontal speed of the OctoWalker on a flat surface was equal to 0.44 m/s (1.56 km/h) (C1) and the normalized speed was equal to 1.07 1/s (3.84 1/h). This is slower than wheel-based EPWs, but faster than leg-based EPWs and most walking robots with a closed-chain leg mechanism [99, 100, 108, 112-117]. The top horizontal part of the toe and heel trajectories had the largest absolute speeds, in which after lifting the feet up and before dropping the feet down caused the largest speed changes in the feet. This would mean that the energy consumption would also be the largest during this period [83]. A maximum initial horizontal peak acceleration of 3.39 m/s^2 was measured during the unloaded walking tests, in which the OctoWalker settled to a mean horizontal acceleration of -0.024 m/s^2. This was caused due to the vertical fluctuations of the OctoWalker.

7.1.5   Steering and control
The EPWW can be controlled single-handed by a wired two-axis joystick (S4), allowing it to walk forward, walk backward, steer to the left and right, accelerate and decelerate (FR2, FR3, FR4). Spinning or steering the OctoWalker to the left resulted in a minimum left turning radius of 100 mm. Spinning the OctoWalker to the right resulted in a minimum right turning radius of 121 mm, which did not exceed the maximum allowed turning radius of 933 mm (C3). Since the design of the OctoWalker is symmetrical, the difference of these turning radii could be caused due to the phase differences in the front and hind legs. However, further analysis on these phase differences are required. Besides the control of the joystick, no additional sensors and complex control features were implemented in the OctoWalker with respect to current EPWs, such as traction and suspension control [11]. The battery was tested during a static unloaded test, in which the OctoWalker was able to "walk" for 34 minutes and 39 seconds. During this test the initial maximum speed slowly decreased from 120 RPM to 72 RPM. Therefore, speed differences during different tests could also be caused due to a decreased capacity level of the battery. The battery had an estimated average current of 5.88 A and a mean electric power of 32 W, resulting in an electrical power-to-weight-ratio of 6.1 W/kg. The required mechanical power for the OctoWalker will in reality be lower than the required electrical power, due to losses from heat and friction in the overall mechanism and electrical losses in the cables and motors [118].

7.2   Scalability
7.2.1   Manufacturing techniques and materials
Scaling the overall dimensions of the OctoWalker, would result in a scaling factor of $\beta^3 = 27$ for the weight of the OctoWalker [122]. This would result in an EPWW of 140 kg, which is heavier than current existing EPWs (~60 kg) [40]. The use of steel plates for the frames and leg mechanism is one of the main causes of this large weight. Scaling the OctoWalker would allow for different lighter material options of the leg mechanism, such as aluminium. However, the mechanical differences between steel and aluminium have to be considered when scaling the OctoWalker. Steel has the ability to laser cut, up to thicknesses of 25 mm, while aluminium has a maximum cuttable thickness of 2 mm [90,

91]. Therefore, thicker aluminium plates would require a different accurate manufacturing technique, e.g. CNC milling. Additionally, aluminium (E = 71 GPa) has a lower module of elasticity with respect to steel (E = 200 GPa) [85], which means that the thickness of each link of the leg mechanism is also scaled more than β = 3, in order to achieve the same structural strength. This would again lead to an increase in weight of the leg mechanism. Therefore, a consensus should be reached between minimizing size and weight of the scaled leg mechanism, while still maintaining its mechanical strength.

The use of FDM with PLA in the true-scaled EPWW for components, such as the seat, safety shields, bearing houses and motor clamps, will also not be possible due to the large sizes and forces. Other materials and manufacturing techniques should be considered, such as aluminium and plastics (e.g. acrylic); and turning and (CNC) milling. However, scaling the EPWW would still require the same amount of components and also the same mechanical complexity with respect to conventional EPWs [108]. This would result in longer production times and potentially the requirement of more frequent repair and replacement services with respect to conventional EPWs. Therefore, it is important to select materials that have a longer life cycle, such that the amount of required service, maintenance and long term costs can be minimized.

7.2.2   Mechanical design
The limited amount of space for the leg mechanisms, resulted in using variations of single and double links. This made the legs of the OctoWalker still weak in the axial direction, especially in the single link connections. In order to increase the axial stiffness of the leg mechanism, double links would be required for every link connection. However, this would increase the overall wheelchair width, which was already one of the main issues of the OctoWalker (7.1.2). When scaling the OctoWalker to a true-scaled EPWW, more space will be available to remove this play, such that it can be subjected to larger axial forces. This could for example be achieved by replacing the book screw joint connections with cylindrical rods and push-on fasteners. The use of these fasteners have the advantage that increasing the rod size, would allow the thickness of these washers to still remain similar (e.g. M6 to M8 rods, d_h = 2.6 mm [84]).

Furthermore, due to the limited space at the feet, the widths of the toe design were increased for higher stability. This was not perceived as an issue when walking over flat undergrounds, since both inner and outer sides of each toe would receive equal amount of reaction forces. However, when walking on unstructured undergrounds, the reaction forces will not be distributed equally, which could cause large bending moments between the feet and legs. This could potentially deform or break the toes. Therefore, in the true-scaled EPWW, triangle structures between the toes and I links should be placed (Figure 4.13 and 4.14), which would decrease the bending moment between the feet and legs. Additionally, the thin rubber layer at the toes and heels were subjected to a lot of wear and tear during the tests. The true-scaled EPWW should, therefore have thicker rubber "shoes" that are easily replaceable.

7.2.3   Electronic design
In practice the weights and dimensions of different electronic and control components, such as the battery and actuators, will not be scaled exactly 27 times; and are expected to have smaller scaling factors. Selecting the correct actuator for the true-scaled EPWW depends on the required torque and weight of the EPWW, which would become larger when scaling the OctoWalker. This would also influence the applied voltage and applied current, and therefore also the required battery [41]. However, it should be considered that a larger torque would also require more expensive actuators. In order to minimize these costs, additional gear transmissions can be placed between the legs and actuator. Conventional EPWs usually have batteries with a nominal voltage output between 12 to 36 V, capacities above 10 Ah and a travel range of 10 to 32 km [103, 120]. The 1:3 scaled OctoWalker had a much smaller estimated travel range (766 m), which depended on the selected battery capacity. The actuator and battery determines therefore many kinematic specifications of an EPWW, such as speed, payload, travel distance, climbing slope, and the type of motor driver.

7.3   Limitations
7.3.1   Design and evaluation limitations
This research mainly focused on the kinematic design of the OctoWalker and did not focus on the user perspectives of the design, such as the seat design, comfort and safety of the user. The 1:3 scaled prototype was tested with dumbbells as payload, to mimic a passenger sitting on the EPWW. However, the weight distribution of these dumbbells do not correspond with the anatomical weight distribution of real humans. Future studies should therefore focus on including feedback from potential users, which can be achieved through doing interviews or questionnaires and tests with disabled people that already use an electric powered wheelchairs. Regarding the safety of the user, protection shields were implemented in the OctoWalker. Nonetheless, safety measures against the environment to decrease the risk of accidents were not implemented yet, such as a safety belt or a required braking distance [108]. In order to collect the data of the OctoWalker, videos were recorded and processed in Kinovea, in which it was assumed that the OctoWalker was a two-dimensional object. In practice the view angle of the camera could deform the recorded objects, which could result in measuring inaccuracies. Moreover, the measured walking range of the OctoWalker was limited to 1 m. The evaluation of the prototype was therefore only done in an indoor off-site setting. In order to have a better understanding of the poor environmental conditions in LMICs, future studies should focus more on outdoor and on-site testing in these LMICs.

7.3.2   Societal and economical limitations
A wheelchair is a critical source of mobility, which allows a person with a disability to become independent and able to integrate into society, especially LMICs which have higher disability rates due to poverty [6, 9, 10]. The majority of LMICs have an average income of € 2015 GNI per capita, which would make it difficult to buy a low-cost EPW by private individuals [121]. Therefore, funding and support is required in order to provide a suitable wheelchair for these people, for example from the government or insurance companies [122]. Additionally, an EPWW requires many components, which would also mean that the EPWW would require more repair and maintenance services than

conventional (electric) wheelchairs; which also increases the costs of the EPWW. Hartridge et al. (1991) estimates that conventional electric wheelchairs usually have an annual maintenance cost of 25% to 30% of the purchase price [122]. However, in these LMICs maintenance and repair services are usually short in supply [34]. Therefore, it should also be considered where the EPWWs should be manufactured and where these manufacturing and service stations should be located. Manufacturing these EPWWs in LMICs in combination with more service stations would reduce the costs for these EPWWs and indirectly also create more job opportunities for the locals. Besides these societal and economical issues, the lack of stable electric supply still persist, especially in the least developed countries [123]. Therefore, other forms of electrical supply, such as solar powered batteries, should also be considered for these less developed countries.

8   Recommendations

This research mainly focused on the kinematic design of the 1:3 scaled OctoWalker, in order to analyze its feasibility and conduct specific design guidelines for a true-scaled EPWW. Future studies could therefore focus on the following design recommendations for building and improving a true-scaled EPWW:

- Using other materials (e.g. aluminium), in order to decrease the weight of the EPWW, while still maintaining the mechanical strength.
- Using push-on fasteners joint connections with double link connections, in order to improve the axial stability of the legs, while also decreasing the width of the EPWW.
- Adding triangle structures between the toes and legs in order to minimize the bending moment at the feet.
- Focus on solutions that minimize the risk of collisions of the legs against obstacles by adding more intelligence (e.g. ultrasonic sensors), for example rearrange the leg configuration when approaching an obstacle.
- Focus on stability control methods for climbing larger slopes, for example by implementing a mechanism that could change the COG of the EPWW.
- Focus on designing for a longer life cycle, such that the required service, maintenance and long term costs could be minimized.
- Increase the battery life by a larger capacity, allowing for a larger travel range, while also considering other forms of electric supply such as solar powered batteries.
- Focus on the user perspectives of the design, such as the seat design, comfort and safety of the user; and include feedback from potential users by doing interviews and questionnaires.
- Focus on testing the EPWW with potential users and more on-site outdoor testing, in order to get a better understanding of the poor environmental conditions.

9   Conclusion

This study presents the design and evaluation of the first prototype of an electric powered walking wheelchair (EPWW) with an one degree of freedom closed-chain walking mechanism, called the OctoWalker, for the purpose of providing transportation for human adults with lower and upper extremity impairments in low- and middle-income countries (LMICs). An 1:3 scaled prototype with a modified Trotbot leg mechanism, two DC motors, timing belt transmission and electronic differential was designed and build according to the ISO-7176 standards for wheelchairs. The mechanical, kinematic, control and electronic specifications of the OctoWalker were evaluated and compared to currently available electric powered wheelchairs (EPWs). The OctoWalker was able to climb over curb heights of 50 mm and slopes up to 28° without the need of additional sensors and control features to maintain its stability. This reduces the control complexity and costs of the OctoWalker with respect to other currently available stair-climbing and obstacle avoidance EPWs. Additionally, a true-scaled OctoWalker would have a larger payload (135 kg), step length (675 mm) and speed (4.75 km/h) than currently existing leg-based EPWs. Improvements for a true-scaled OctoWalker are required in terms of travel range (2.5 km), wheelchair width (789 mm) and weight (140 kg), in order to achieve similar specifications as stair-climbing and obstacle avoidance EPWs. Besides that, future studies should also focus on other factors, such as user perspectives, safety and the societal and economical issues in these LMICs. Generally speaking, this EPWW is the first build prototype with a modified Trotbot mechanism and opens up future opportunities for providing low-cost transportation for disabled people in the rural environmental conditions of LMICs with respect to the currently available expensive stair-climbing and obstacle avoidance EPWs .

References

[1]   Banks, L.M., Kuper, H., & Polack, S. (2017). Poverty and disability in low- and middle-income countries: A systematic review. *PLOS ONE*, 12(12). doi: 10.1371/journal. pone.0189996.

[2]   Wheelchair Foundation. (2019). *Worldwide need*. Retrieved Nov. 24, 2022, from https://www.wheelchairfoundation.org/ fth/analysis-of-wheelchair-need/.

[3]   World Health Organization, & The World Bank. (2011*). World report on disability*. Geneva: WHO. ISBN: 9789-2406-8521-5.

[4]   Parnes, P., Cameron, D., Christie, N., et al. (2009). Disability in low-income countries: Issues and implications. *Disability and Rehabilitation*, 31(14), 1170-1180. doi: 10.1080/096382 80902773778.

[5]   The World Bank. (2021). *GNI per capita, Atlas method (current US$)*. Retrieved Nov. 24, 2022, from https://data.worldbank.org/indicator/NY.GNP.PCAP.CD?mo st_recent_value_desc=false.

[6]   Shore, S., & Juillerat, S. (2012). The impact of a low cost wheelchair on the quality of life of the disabled in the developing world. *Medical Science Monitor*, 18(9). doi: 10.12659/msm.883348.

[7]   Oderud, T. (2014). Surviving spinal cord injury in low income countries. *African Journal of Disability*, 3(2). doi: 10.4102/ajod.v3i2.80.

[8]   Vergunst, R., Swartz, L., et al. (2015). 'you must carry your wheelchair' – barriers to accessing healthcare in a South African rural area. *Global Health Action*, 8(1). doi: 10.3402/gha.v8.29003.

[9]   Trani, J., & Loeb, M. (2010). Poverty and disability: A vicious circle? evidence from Afghanistan and Zambia. *Journal of International Development*, 24. doi: 10.1002/jid.1709.

[10] Yeo, R., & Moore, K. (2003). Including disabled people in poverty reduction work: "nothing about us, without us". *World Development*, 31(3), 571-590. doi: 10.1016/s0305-750x(02)00218-8.

[11] Ding, D., & Cooper, R. (2005). Electric powered wheelchairs. *IEEE Control Systems*, 25(2), 22-34. doi: 10.1109/mcs.2005.1411382.

[12] Attali, X., & Pelisse, F. (2001). Looking back on the evolution of electric wheelchairs. *Medical Engineering & Physics*, 23(10), 735-743. doi: 10.1016/s1350-4533(01)00053-4.

[13] Tao, W., Xu, J., & Liu, T. (2017). Electric-powered wheelchair with stair-climbing ability. *International Journal of Advanced Robotic Systems*, 14(4). doi: 10.1177/1729881417721436.

[14] Heinrich, A. (2016). *Topchair-S wheelchair has no problem with stairs.* Retrieved Nov. 24, 2022, from https://newatlas.com/topchair-s-stair-climbing-wheelchair/41421/.

[15] IBOT. (2022). *Meet iBOT.* Retrieved Nov. 24, 2022, from https://meetibot.com/nl/pers/.

[16] 永井美智子. (2010). *フォトレポート：トヨタが描く、新しい自動車のカタチ (Photo report: A new form of automobile drawn by Toyota).* Retrieved Nov. 24, 2022, from https://japan.cnet.com/article/20078203/.

[17] Chocoteco, J., Morales, R., & Feliu, V. (2015). Improving the climbing/descent performance of stair-climbing mobility systems confronting architectural barriers with geometric disturbances. *Mechatronics*, 30, 11-26. doi: 10.1016/j.mechatronics.2015.06.001.

[18] Norton, R.L. (2020). *Design of machinery: An introduction to the synthesis and analysis of mechanisms and machines.* New York, NY: McGraw-Hill Education. ISBN: 9780-0731-2158-1.

[19] Grübler, M. (1917). *Getriebelehre (Gear gauge).* doi: 10.1007/978-3-662-32953-5.

[20] McCarthy, J.M., & Soh, G.S. (2011). Geometric design of linkages. *Interdisciplinary Applied Mathematics.* doi: 10.1007/978-1-4419-7892-9.

[21] Fang, W.E., & Freudenstein, F. (1990). The stratified representation of mechanisms. *Journal of Mechanical Design*, 112(4), 514-519. doi: 10.1115/1.2912640.

[22] Yadav, J.N., Pratap, C.R., & Agrawal, V.P. (1995). Detection of isomorphism among kinematic chains using the distance concept. *Journal of Mechanical Design*, 117(4), 607-611. doi: 10.1115/1.2826728.

[23] Ding, D., Parmanto, B., et al. (2007). Design considerations for a personalized wheelchair navigation system. *2007 29th Annual International Conference of the IEEE Engineering in Medicine and Biology Society.* doi: 10.1109/iembs.2007.4353411.

[24] Kairy, D., Rushton, P., et al. (2014). Exploring powered wheelchair users and their caregivers' perspectives on potential intelligent power wheelchair use: A qualitative study. *International Journal of Environmental Research and Public Health*, 11(2), 2244-2261. doi: 10.3390/ijerph110202244.

[25] Mines, R. (2008). Wheelchair postural support solutions for low-income countries. *Ergonomics in Design: The Quarterly of Human Factors Applications*, 16(4), 4-28. doi: 10.1518/106480408x393356.

[26] Pearlman, J., Cooper, R.A., et al. (2008). Lower-limb prostheses and wheelchairs in low-income countries [an overview]. IEEE *Engineering in Medicine and Biology Magazine*, 27(2), 12-22. doi: 10.1109/emb.2007.907372.

[27] Aldersey, H., Quadir, M.M., et al. (2018). Barriers and facilitators for wheelchair users in Bangladesh: A participatory action research project. *Disability, CBR Inclusive Development*, 29(2), 24. doi: 10.5463/dcid.v29i2.730.

[28] Parekh, B.J., Thakkar, P.N., & Tambe, M.N. (2015). Design and analysis of Theo Jansen's mechanism based sports ground (pitch) marking robot. *11th IEEE India Conference: Emerging Trends and Innovation in Technology.* doi: 10.1109/INDICON.2014.7030533.

[29] Desai, S.G., Annigeri, A.R., & Timmana, A. (2019). Analysis of a new single degree-of-freedom eight link leg mechanism for walking machine. *Mechanism and Machine Theory*, 140, 747-764. doi: 10.1016/j.mechmachtheory.2019.06.002.

[30] Vogel, B. (2021). *The iBOT is back. is the second time the charm?* Retrieved Nov. 24, 2022, from https://newmobility.com/the-ibot-is-back/.

[31] De Britto, W., Filho, V., & Bezerra, J.M. (2010). Mechatronic design of a chair for disabled with locomotion by legs. *ABCM Symposium Series in Mechatronics 5,* pp. 1142–1149. ISBN 9788-5857-6950-5. Retrieved Nov. 30, 2022, from https://abcm.org.br/symposium-series/SSM_Vol5/Section_VII_Robotics/13031.pdf.

[32] ISO. (2017). *ISO-7176.* Retrieved Nov. 26, 2022, from https://www.iso.org/search/x/query/7176.

[33] Malan, R., & Bredemeyer, D. (2001). *Functional requirements and use cases.*

[34] Williams, E., Hurwitz, E., et al. (2017). Perspectives of basic wheelchair users on improving their access to wheelchair services in Kenya and Philippines: A qualitative study. *BMC International Health and Human Rights*, 17(1). doi: 10.1186/s12914-017-0130-6.

[35] Labib, O.E.E., El-Safty, S.W., et al. (2019). Towards a stair climbing robot system based on a re-configurable linkage mechanism. *Advances in Intelligent Systems and Computing*, 867, 278–288. doi: 10.1007/978-3-030-01370-7_22.

[36] Wu, J., Yang, H., et al. (2021). Design and analysis of a novel octopod platform with a reconfigurable trunk. *Mechanism and Machine Theory, 156.* doi: 10.1016/j.mechmachtheory. 2020.104134.

[37] Wu, J., Guo, L., et al. (2021). Design and performance analysis of a novel closed-chain elastic-bionic leg with one actuated degree of freedom. *Mechanism and Machine Theory*,165. doi: 10.1016/j.mechmachtheory.2021.104444.

[38] Kruth, J., Leu, M., & Nakagawa, T. (1998). Progress in additive manufacturing and rapid prototyping. *CIRP Annals*, 47(2), 525-540. doi: 10.1016/s0007-8506(07)63240-5.

[39] Rainford Solutions. (2021). *IP ratings explained: IP rating chart.* Retrieved Nov. 26, 2022, from https://rainfordsolutions.com/products/ingress-protection-ip-rated-enclosures/ip-enclosure-ratings-standards-explained/.

[40] Rodrigo, S.E., & Herrera, C.V. (2008). Wheelchairs: History, characteristics, and technical specifications. *Smart Wheelchairs and Brain-Computer Interfaces*, 257-290. doi: 10.1016/b978-0-12-812892-3.00011-x.

[41] Chung, M., & Wang, M. J. (2010). The change of gait parameters during walking at different percentage of preferred walking speed for healthy adults aged 20-60 years. *Gait & Posture*, 31(1), 131-135. doi: 10.1016/j.gaitpost.2009.09.013.

[42] Geyer, H., Seyfarth, A., & Blickhan, R. (2006). Compliant leg behaviour explains basic dynamics of walking and running. *Proceedings of the Royal Society B: Biological Sciences*, 273(1603), 2861-2867. doi: 10.1098/rspb.2006.3637.

[43] Walpole, S.C., Prieto-Merino, D., et al. (2012). The weight of nations: An estimation of adult human biomass. *BMC Public Health*, 12(1). doi: 10.1186/1471-2458-12-439.

[44] ISO. (2012). *ISO 7176-11:2012 (en) Wheelchairs – Part 11: Test dummies.* Retrieved Nov. 26, 2022, from https://www.iso.org/standard/53056.html.

[45] Altalmas, T., Ahmad, S., et al. (2013). Mechanical design and simulation of two-wheeled wheelchair using solidworks *IOP Conf. Series: Materials Science and Engineering*, 53. doi: 10.1088/1757-899X/53/1/012042.

[46] ISO. (2008). *ISO 7176-5:2008 (en) Wheelchairs – Part 5: Determination of dimensions, mass and manoeuvring space.* Retrieved Nov. 26, 2022, from https://www.iso.org/obp/ui/#iso:std:iso:7176:-5:ed-2:v1:en.

[47] ISO. (2022). *ISO 7176-25:2022 (en) Wheelchairs – Part 25: Lead-acid batteries and chargers for powered wheelchairs – Requirements and test methods.* Retrieved Nov. 26, 2022, from https://www.iso.org/obp/ui/#iso:std:iso:7176:-25:ed-2:v1:en.

[48] Generex Systems. (2020). *Lithium vs lead acid –Safety first*. Retrieved Nov. 26, 2022, from https://www.generex.de/news/lithium-fire.

[49] Keljik, J. (2013). *Electricity 4: AC/DC Motors, controls, and maintenance*. Clifton Park, NY: Delmar, Cengage Learning. ISBN: 9781-1116-4675-2.

[50] Cooper, R.A. (1995). *Rehabilitation Engineering applied to mobility and manipulation*. doi: 10.1201/9780367802448.

[51] Pradita, A.A., Priadythama, I., & Susmartini, S. (2018). Perancangan ulang kursi roda manual menggunakan kriteria standar ISO 7176-5 (Manual wheelchair redesign using ISO 7176-5 standard criteria). *Performa : Media Ilmiah Teknik Industri*, 17(1). doi: 10.20961/performa.17.1.19068.

[52] Candiotti, J.L., Kamaraj, D.C., et al. (2019). Usability evaluation of a novel robotic power wheelchair for indoor and outdoor navigation. *Archives of Physical Medicine and Rehabilitation*, 100(4), 627-637. doi: 10.1016/j.apmr.2018.07.432.

[53] Kirby, R.L., Bennett, S., et al. (2008). Wheelchair curb climbing: Randomized controlled comparison of highly structured and conventional training methods. *Archives of Physical Medicine and Rehabilitation*, 89(12), 2342-2348. doi: 10.1016/j.apmr.2008.04.028.

[54] Lalumiere, M., Gagnon, D.H., et al. (2013). Ascending curbs of progressively higher height increases forward trunk flexion along with upper extremity mechanical and muscular demands in manual wheelchair users with a spinal cord injury. *Journal of Electromyography and Kinesiology*, 23(6), 1434-1445. doi: 10.1016/j.jelekin.2013.06.009.

[55] Plaxico, C.A. (2002). *Design guidelines for the use of curbs and curb/guardrail combinations along high-speed roadways*. Retrieved Nov. 26, 2022, from https://core.ac.uk/download/pdf/212997676.pdf.

[56] Ackermans, T.M., Francksen, N.C., et al. (2020). Stair negotiation behaviour of older individuals: Do step dimensions matter? *Journal of Biomechanics*, 616, 101-109. doi: 10.1016/j.jbiomech.2020.109616.

[57] Livingston, L.A., Stevenson, J.M., Olney, S.J. (1991). Stairclimbing kinematics on stairs of differing dimensions. *Arch Phys Med Rehabil.* 72(6), 398-402. PMID: 2059107.

[58] Livingston, L.A., Mandigo, J.L., & Irwin, J. (1995). *Influence of stair dimensions and subject height on angular displacement of the trunk during stairclimbing*.

[59] Ogawa, A., Iijima, H., & Takahashi, M. (2021). Staircase design for health monitoring in elderly people. *Journal of Building Engineering*, 37, 102-152. doi: 10.1016/j.jobe.2021.102152.

[60] Vagle, W. (2018). *Walker ABC's*. Retrieved Nov. 26, 2022, from https://www.diywalkers.com/walker-abcs.html.

[61] Artobolevsky, I. (1975). *Mechanisms in modern engineering design: Lever mechanisms, Vol. 1*. Moscow: MIR. ISBN: 9789-9956-0998-6.

[62] Klann, J. (1998). *U.S. Patent No. US6260862B1*. Washington, DC: U.S. Patent and Trademark Office.

[63] Jansen, T. (2016). *The great pretender*. Rotterdam: Nai010. ISBN: 9789-4620-8344-8.

[64] Vagle, W. (2018). *Strider linkage plans*. Retrieved November 27, 2022, from https://www.diywalkers.com/strider-linkage-plans.html.

[65] Vagle, B., & Vagle, W. (2016). *TrotBot linkage plans*. Retrieved Nov. 27, 2022, from https://www.diywalkers.com/trotbot-linkage-plans.html.

[66] Ghassaei, A. (2011). *The design and optimization of a crank-based leg mechanism* (master's thesis). Pomona College Department of Physics and Astronomy. Retrieved Nov. 27, 2022, from https://amandaghassaei.com/projects/mechanical_walking_machine/.

[67] Shigley, J. (1960). *The mechanics of walking vehicles*, Report. Detroit, Michigan: The University of Michigan Research Institute. Retrieved Nov. 27, 2022, from https://www.diywalkers.com/uploads/5/3/3/9/53394177/shigley-mech-of-walk-veh-1960.pdf.

[68] Kavlak, K., & Kartal, I.A. (2021). Kinematic analysis of mobile robot with Klann walking mechanism. *2021 3rd International Congress on Human-Computer Interaction, Optimization and Robotic Applications (HORA)*. doi: 10.1109/hora52670.2021.9461372.

[69] Maulana, E., Muslim, M.A., & Zainuri, A. (2014). Inverse kinematics of a two-wheeled differential drive an autonomous mobile robot. *2014 Electrical Power, Electronics, Communicatons, Control and Informatics Seminar (EECCIS)*. doi: 10.1109/eeccis.2014.7003726.

[70] Simionescu, P.A., Hoeltgebaum, T., & Martins, D. (2022). On the evolution of automotive steering mechanisms. *Proceedings of the 2022 USCToMM Symposium on Mechanical Systems and Robotics*, 116-128. doi: 10.1007/978-3-030-99826-4_11.

[71] Mitchell, W., Staniforth, A., & Scott, I., (2006). *Analysis of Ackermann steering geometry*. SAE Technical Paper 2006-01-3638, doi: https://doi.org/10.4271/2006-01-3638.

[72] Mihailidis, A., & Nerantzis, I. (2013). Recent developments in automotive differential design. *Power Transmissions*, 125-140. doi: 10.1007/978-94-007-6558-0_8.

[73] Davis, C. (1934). *U.S. Patent No. US2065661A*. Washington, DC: U.S. Patent and Trademark Office.

[74] Brumercik, F., Lukac, M., & Nieoczym, A. (2015). Mechanical differential mathematical model. *Communications - Scientific Letters of the University of Zilina*, 17(3), 88-91. doi: 10.26552/com.c.2015.3.88-91.

[75] Khattak, M. (2017). *What is a differential and how it works!* Retrieved Nov. 27, 2022, from https://www.pakwheels.com/blog/differential-working/.

[76] Parsons, F. (1994). *U.S. Patent No. US5443430A*. Washington, DC: U.S. Patent and Trademark Office.

[77] Young, A., Spooner, J., & Chippendale, J. (1993). *U.S. Patent No. US5557986A*. Washington, DC: U.S. Patent and Trademark Office.

[78] Condit, R. (2004). *Brushed DC motor fundamentals. Microchip Application Note AN905*. Microchip Technology Inc. Retrieved Nov. 27, 2022, from https://pi-plates.com/downloads/AN905.pdf.

[79] Moyer, E., & Chicago, U. (2010). *Basics on electric motors*. Retrieved Nov. 27, 2022, from https://geosci.uchicago.edu/~moyer/GEOS24705/Readings/ElecReadingII_Motors.pdf.

[80] Gastreich, W. (2022). *Stepper motors advantages and disadvantages*. Retrieved Nov. 27, 2022, from shorturl.at/adfX8.

[81] Gastreich, W. (2022). *What is a servo motor?' and how it works*. Retrieved Nov. 27, 2022, from https://realpars.com/servo-motor/.

[82] Gosselin, C., & Angeles, J. (1990). Singularity analysis of closed-loop kinematic chains. *IEEE Transactions on Robotics and Automation*, 6(3), 281-290. doi: 10.1109/70.56660.

[83] Komoda, K., & Wagatsuma, H. (2016). Energy-efficacy comparisons and multibody dynamics analyses of legged robots with different closed-loop mechanisms. *Multibody System Dynamics*, 40(2), 123-153. doi: 10.1007/s11044-016-9532-9.

[84] Baker & Finnemore Ltd. (2016). *Starlock push-on fasteners data sheet*. Retrieved Nov. 28, 2022, from https://www.viba.nl/media/files//resources/103676%2020618starlocks_-_metric.pdf.

[85] Beek, A.V. (2019). *Advanced engineering design: Lifetime performance and reliability*. Delft: TU Delft. ISBN: 9789-0810-4061-7.

[86] Stock Drive Products, & Sterling Instruments. (2017). *Handbook of timing belts, pulleys, chains and sprockets*. Retrieved Nov. 28, 2022, from https://www.sdp-si.com/PDFS/Technical-Section-Timing.pdf.

[87] Asamer, J., Graser, A., et al. (2016). Sensitivity analysis for energy demand estimation of electric vehicles. *Transportation Research Part D: Transport and Environment*, 46, 182-199. doi: 10.1016/j.trd.2016.03.017.

[88] Calanca, A., Toxiri, S., et al. (2020). Actuation selection for assistive exoskeletons: Matching capabilities to task requirements. *IEEE Transactions on Neural Systems and Rehabilitation Engineering*, 28(9), 2053-2062. doi: 10.1109/tnsre.2020.3010829.

[89] Modelcraft. (2014). *Technical Data RB350050-22H22R*.

[90] Seaman, F. (1988). *Laser cutting* (pp. 1-113, Report No. MTIAC SOAR-88-02). Cresap: A Towers Perring Company. Retrieved Nov. 30, 2022, from https://apps.dtic.mil/sti/pdfs/ADA198299.pdf.

[91] Nattermann, K., & Hermanns, C. (2002). Post-processing by laser cutting. *Schott Series on Glass and Glass Ceramics*, 381-412. doi: 10.1007/978-3-642-55966-2_7.

[92] Roberts, B. (2012). Paint systems for steel. *Steel Times International*, 36(3), 36-37. Retrieved Nov. 30, 2022, from: https://www.steeltimesint.com/content-images/subscriberpdfs/sti_april_2012_editorial_3916.pdf.

[93] Myoshi, K. (2007). *Solid lubricants and coatings for extreme environments: State-of-the-art survey* (pp. 1-23, Rep. No. NASA/TM-2007-214668). Cleveland, Ohio: NASA, Glenn Research Center. Retrieved Nov. 30, 2022, from https://ntrs.nasa.gov/citations/20070010580.

[94] Rao, K., & Xie, C. (2006). A comparative study on the performance of Boric acid with several conventional lubricants in metal forming processes. *Tribology International*, 39(7), 663-668. doi: 10.1016/j.triboint.2005.05.004.

[95] Saharia, T., Bauri, J., & Bhagabati, C. (2017). Joystick controlled wheelchair. *International Research Journal of Engineering and Technology*, 4(7), 235-237. e-ISSN: 2395-0056.

[96] Kinovea. (2021). *Linear and angular kinematics*. Retrieved Nov. 29, 2022, from https://www.kinovea.org/help/en/measurement/kinematics.html.

[97] MathWorks Benelux. (2016). *Filtfilt, zero-phase digital filtering*. Retrieved Nov. 29, 2022, from https://nl.mathworks.com/help/signal/ref/filtfilt.html.

[98] Evcil, A.N. (2009). Wheelchair accessibility to public buildings in Istanbul. *Disability and Rehabilitation: Assistive Technology*, 4(2), 76- 85. doi: 10.1080/17483100802543247.

[99] Davies, D., & Hirose, S. (2009). Continuous high-speed climbing control and leg mechanism for an eight-legged stair-climbing vehicle. *2009 IEEE/ASME International Conference on Advanced Intelligent Mechatronics*. doi: 10.1109/aim.2009.5229819.

[100] Sugahara, Y., Hashimoto, K., et al. (2006). Towards the biped walking wheelchair. *The First IEEE/RAS-EMBS International Conference on Biomedical Robotics and Biomechatronics*, 2006. BioRob 2006. doi: 10.1109/biorob.2006.1639185.

[101] Birglen, L., & Ruella, C. (2014). Analysis and optimization of one-degree of Freedom Robotic legs. *Journal of Mechanisms and Robotics*, 6(4). doi: 10.1115/1.4027234.

[102] Giesbrecht, D., Wu, C. Q., & Sepehri, N. (2012). Design and optimization of an eight-bar legged walking mechanism imitating a kinetic sculpture, "Wind beast". *Transactions of the Canadian Society for Mechanical Engineering*, 36(4), 343-355. doi: 10.1139/tcsme-2012-0024.

[103] Liu, C., Lin, M., et al. (2017). The development of a multi-legged robot using eight-bar linkages as leg mechanisms with switchable modes for walking and stair climbing. *2017 3rd International Conference on Control, Automation and Robotics*, 103-108. doi: 10.1109/iccar.2017.7942669.

[104] Soyguder, S., & Alli, H. (2007). Design and prototype of a six-legged walking insect robot. *Industrial Robot: An International Journal*, 34(5), 412-422. doi: 10.1108/01439910710774412.

[105] Sun, J., & Zhao, J. (2019). An adaptive walking robot with reconfigurable mechanisms using shape morphing joints. *IEEE Robotics and Automation Letters*, 4(2), 724-731. doi: 10.1109/lra.2019.2893439.

[106] Gard, S.A., Childress, D.S. (2001). What determines the vertical displacement of the body during normal walking? *JPO Journal of Prosthetics and Orthotics*, 13(3), 64-67. doi: 10.1097/00008526-200109000-00009.

[107] Buchner, H., Obermüller, S., & Scheidl, M. (2000). Body centre of mass movement in the sound horse. *The Veterinary Journal*, 160(3), 225-234. doi: 10.1053/tvjl.2000.0507.

[108] Rentschler, A. J., Cooper, R. A., et al. (2004). Evaluation of selected electric-powered wheelchairs using the ANSI/resna standards. *Archives of Physical Medicine and Rehabilitation*, 85(4), 611-619. doi: 10.1016/j.apmr.2003.06.023.

[109] Lawn, M., Sakai, T., et al. (2001). *Development and practical application of a stairclimbing wheelchair in Nagasaki*. Retrieved Nov. 30, 2022, from http://murraylawn.org/MJLneWW/kaistPp2.pdf.

[110] Quaglia, G., & Nisi, M. (2017). Design of a self-leveling cam mechanism for a stair climbing wheelchair. *Mechanism and Machine Theory*, 112, 84-104. doi: 10.1016/j.mechmachtheory.2017.02.003.

[111] Yu, S., Wang, T., et al. (2010). Configuration and tip-over stability analysis for stair-climbing of a new-style wheelchair robot. *2010 IEEE International Conference on Mechatronics and Automation*. doi: 10.1109/icma.2010.5589079.

[112] Kim, H., Lee, D., Jeong, K., & Seo, T. (2015). Water and ground-running robotic platform by repeated motion of six spherical footpads. *IEEE/ASME Transactions on Mechatronics*. doi: 10.1109/tmech.2015.2435017.

[113] Wu, J., Ruan, Q., et al. (2015). A novel skid-steering walking vehicle with dual single-driven quadruped mechanism. *Mechanisms, Transmissions and Applications*, 231-238. doi: 10.1007/978-3-319-17067-1_24.

[114] Wu, J., & Yao, Y. (2018). Design and analysis of a novel walking vehicle based on leg mechanism with variable topologies. *Mechanism and Machine Theory*, 128, 663-681. doi: 10.1016/j.mechmachtheory.2018.07.008.

[115] Wu, J., Yao, Y., et al. (2019). Design and analysis of a sixteen-legged vehicle with reconfigurable close-chain leg mechanisms. *Journal of Mechanisms and Robotics*, 11(5). doi: 10.1115/1.4044003.

[116] Yang, J., Saab, W., et al. (2021). Reuleaux triangle–based two degrees of freedom bipedal robot. *Robotics*, 10(4), 114. doi: 10.3390/robotics10040114.

[117] Wu, J., Yang, H., et al. (2021). Design and analysis of a novel octopod platform with a reconfigurable trunk. *Mechanism and Machine Theory*, 156, 104-134. doi: 10.1016/j.mechmachtheory.2020.104134.

[118] Takacs, G. (2018). Analysis and optimization. *Electrical Submersible Pumps Manual*, 307-366. doi: 10.1016/b978-0-12-814570-8.00006-4.

[119] Alves, M., & Oshiro, R.E. (2006). Scaling impacted structures when the prototype and the model are made of different materials. *International Journal of Solids and Structures*, 43(9), 2744-2760. doi: 10.1016/j.ijsolstr.2005.03.003.

[120] Kauzlarich, J.J. (1990). Wheelchair batteries II: Capacity, sizing, and life. The Journal of Rehabilitation Research and Development, 27(2), 163. doi: 10.1682/jrrd.1990.04.0163.

[121] OECD. (2022). *DAC list of ODA recipients | Effective for reporting on 2022 and 2023 flows*. Retrieved December 01, 2022, from https://www.oecd.org/dac/financing-sustainable-development/development-finance-standards/daclist.htm.

[122] Hartridge, M., & Seeger, B. R. (1990). International wheelchair standards: A study of costs and benefits. *Assistive Technology*, 2(4), 117-124. doi: 10.1080/10400435.1990.10132163.

[123] Neighbour, R., & Eltringham, R. (2012). The design of medical equipment for low income countries: Dual standards or common sense. *7th International Conference on Appropriate Healthcare Technologies for Developing Countries*. doi: 10.1049/cp.2012.1462.

Appendix A Constraints

Table A.1: Overview of the constraints and scaling factors of a true-scaled EPWW. The constraints are divided into general constraints, dimensional constraints and leg constraints. Each requirement includes a requirement identification (ID), the requirement itself and the scaling factor for the 1:3 scaled prototype.

ID	Constraints (1:1)	Scaling factor (β)
General constraints		
C1	The maximum **speed** of the EPWW cannot exceed 1.8 m/s (6.5 km/h).	3
C2	The EPWW must transport **payloads** up to 100 kg.	27
C3	The **turning radius** cannot be larger than 2800 mm.	3
C4	The EPWW must use a lead acid **battery** with a nominal **voltage** not greater than 36 V.	-
Dimensional constraints		
C5	The maximum **wheelchair width** must be 700 mm.	3
C6	The maximum **wheelchair depth** must be 1300 mm.	3
C7	The maximum **seat height** must be 520 mm.	3
C8	The maximum **seat depth** must be 450 mm.	3
C9	The maximum **seat width** must be 450 mm.	3
C10	The maximum inclination of the **seat angle** must be 4°.	-
C11	The maximum **armrest height** must be 200 mm.	3
C12	The maximum **backrest height** must be 420 mm.	3
C13	The maximum **backrest width** must be 450 mm.	3
C14	The **backrest angle** must be between 100°-110°.	-
C15	The minimum **distance** of the **footrest to seat** must be 40 mm.	3
C16	The maximum **distance** of the **footrest to seat** must be 450 mm.	3
C17	The maximum **footrest length** must be 250 mm.	3
Leg constraints		
C18	The minimum **step height** must be 150 mm.	3
C19	The maximum **step length** must not exceed 280 mm.	3
C20	The minimum **climbing slope** must be 20°.	-
C21	The maximum **climbing slope** must be 28°.	-

Appendix B Conceptual design

B.1 Turning radius derivation

Derivation of front-leg steering equation (Figure B.1):

$$\tan(\theta_2) = \frac{W_b}{R_1 + \frac{1}{2}W_t} \rightarrow R_1 = \frac{W_b}{\tan(\theta_2)} - \frac{1}{2}W_t \rightarrow R = \sqrt{l^2 + R_1^2} \rightarrow \boldsymbol{R_f} = \sqrt{\left(\frac{1}{2}\boldsymbol{W_b}\right)^2 + \left(\frac{\boldsymbol{W_b}}{\tan(\boldsymbol{\theta_2})} - \frac{1}{2}\boldsymbol{W_t}\right)^2}.$$

Derivation of the eight-leg steering equation (Figure B.2):

$$\tan(\theta_2) = \frac{\frac{1}{2}W_b}{R + \frac{1}{2}W_t} \rightarrow \left(R + \frac{1}{2}W_t\right)(\tan(\theta_2)) = \frac{1}{2}W_b \rightarrow \boldsymbol{R_e} = \frac{\frac{1}{2}\boldsymbol{W_b}}{\tan(\boldsymbol{\theta_2})} - \frac{1}{2}\boldsymbol{W_t}.$$
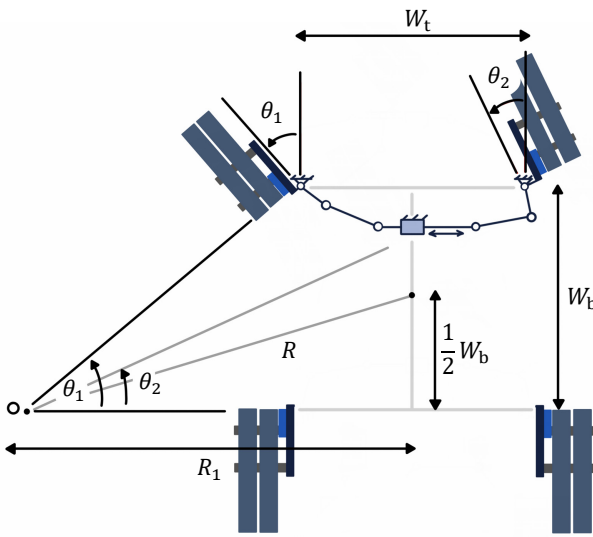
Figure B.1: Visualization of the different variables of the turning radius and maximum rotation angles for front-leg steering.
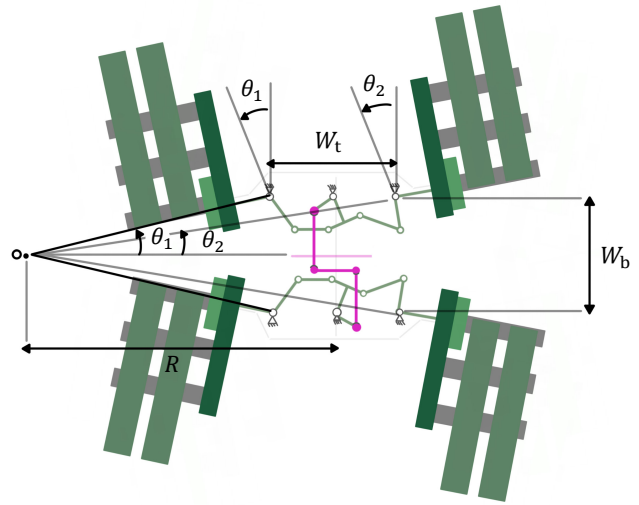
Figure B.2: Visualization of the different variables of the turning radius and maximum rotation angles for eight-leg steering.

B.2 Weighted criteria tables

B.2.1 Leg mechanism

Table B.1: Determining the importance of each performance criteria of the leg mechanism, the more important criteria will receive an "1" score and the less important criteria will receive a "0" score, resulting in a total score for each criteria. This corresponds to a specific weight, which will be used in the concept selection.

	1	2	3	4	5	6	7	8	Total score		Weight		Ranking	Criteria	Weight
1	✕	1	1	0	1	0	0	1	4	Size	5		1	Stability	8
2	0	✕	1	0	1	0	0	1	3	Max. step height	4		2	Footpath design	6
3	0	0	✕	0	1	0	0	0	1	Max. step length	2		3	Adaptability	6
4	1	1	1	✕	1	0	0	1	5	Footpath design	6		4	Size	5
5	0	0	0	0	✕	0	0	0	0	Complexity and costs	1		5	Max. step height	4
6	1	1	1	1	1	✕	1	1	7	Stability	8		6	Max. climbing slope	3
7	1	1	1	1	1	0	✕	1	6	Adaptability	7		7	Max. step length	2
8	0	0	1	0	1	0	0	✕	2	Max. climbing slope	3		8	Complexity and costs	1

B.2.2 Steering mechanism

Table B.2: Determining the importance of each criteria of the steering mechanisms, the more important criteria will receive an "1" score and the less important criteria will receive a "0" score, resulting in a total score for each criteria. This corresponds to a specific weight, which will be used in the concept selection.

	1	2	3	Total score		Weight		Ranking	Criteria	Weight
1	✕	0	0	0	Costs	2		1	Turning radius	3
2	1	✕	0	1	Size	1		2	Costs	2
3	1	1	✕	2	Turning radius	3		3	Size	1

B.2.3 Differential mechanism, transmission mechanism and actuators

Table B.3: Determining the importance of each criteria of the differential mechanism, transmission mechanism and actuators, the more important criteria will receive an "1" score and the less important criteria will receive a "0" score, resulting in a total score for each criteria. This corresponds to a specific weight, which will be used in the concept selection.

	1	2	3	Total score		Weight	Ranking	Criteria	Weight
1	╳	1	0	1	Costs	2	1	**User control**	3
2	0	╳	0	0	AL-ratio	1	2	**Costs**	2
3	1	1	╳	2	User control	3	3	**AL-ratio**	1

Appendix C Final design

C.1   Feet shape generation

For the toe shape generation, the maximum and minimum of joint 6 and joint 7 were analyzed. This resulted in two individual free spaces (Figure C.1 and C.2), which where combined in one free space (Figure C.3). In Figure C.4, the toe free space (blue, 105°) and joined free space (purple, 40°) are shown. For the heel shape generation, the maximum and minimum of joint 6 and joint 10 were analyzed. This resulted in two individual free spaces (Figure C.5 and C.6), which where combined in one free space (Figure C.7). In Figure C.8, the heel free space (red, 45°) and joined free space (purple, 40°) are shown.

joint 7 maximum
joint 6 minimum

joint 6 maximum
joint 7 minimum
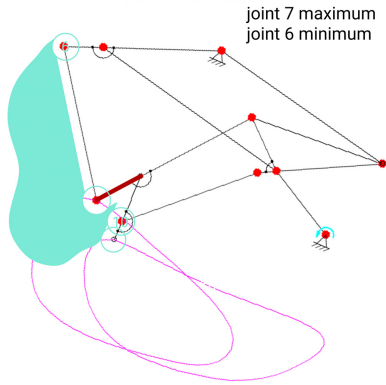
Figure C.1: The configuration of the leg, in which joint 7 is at its maximum angle and joint 6 is at its minimum angle, resulting in an individual toe free space at the front of the leg.
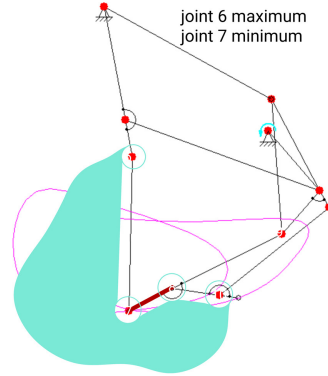
Figure C.2: The configuration of the leg, in which joint 6 is at its maximum angle and joint 7 is at its minimum angle, resulting in an individual toe free space at the front of the leg and below the feet.
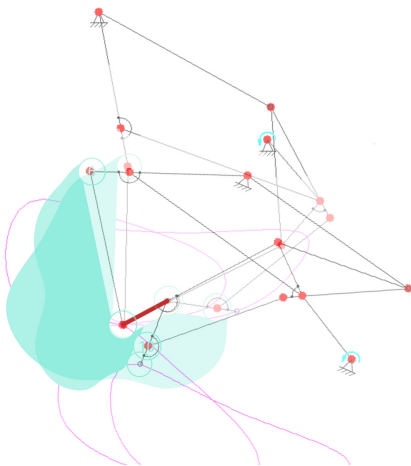
Figure C.3: Combining the individual free spaces of the maximums and minimums of joint 6 and 7 resulted in a combined toe free space.
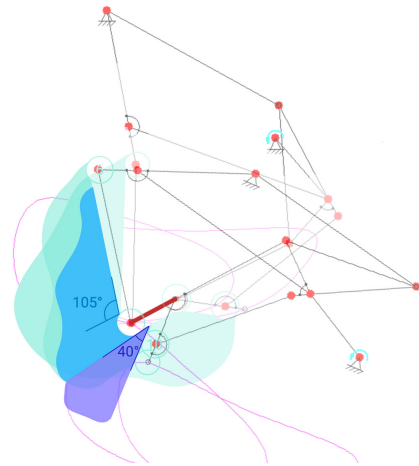
Figure C.4: The combined free spaces was divided into the toe free space (blue, 105°) and joined free space (purple, 40°).

joint 6 maximum
joint 10 maximum

joint 6 minimum
joint 10 minimum
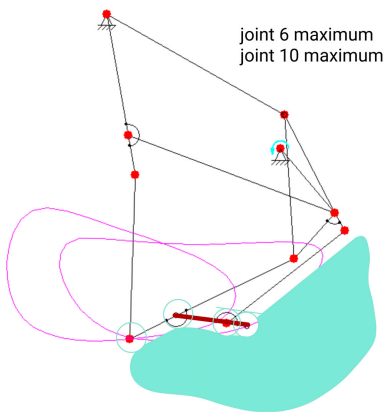
Figure C.5: The configuration of the leg, in which joint 6 and 10 are at its maximum angle, resulting in an individual heel free space at the back of the leg and below the feet.
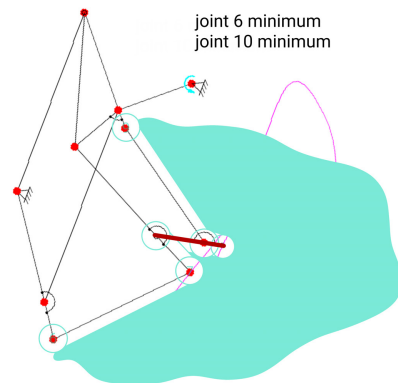
Figure C.6: The configuration of the leg, in which joint 6 and 10 are at its minimum angle, resulting in an individual heel free space at the front and back of the leg and below the feet.
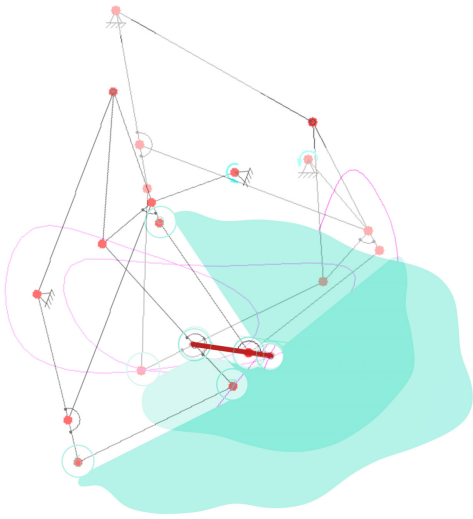
Figure C.7: Combining the individual free spaces of the maximums of joint 6 and 10 resulted in a combined heel free space.
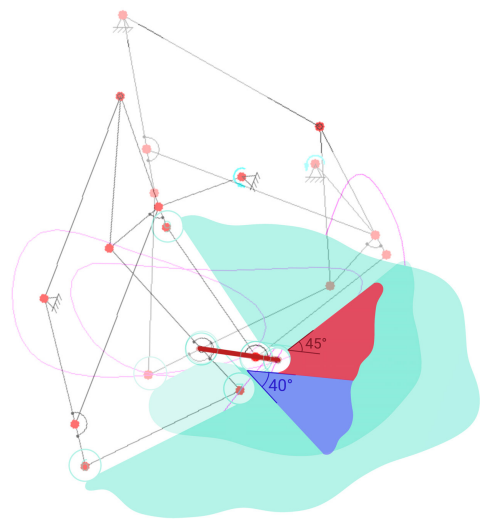
Figure C.8: The combined free space was divided into the heel free space (red, 45°) and joined free space (purple, 40°).

C.2   Feet design

(a)

(b)

(c)
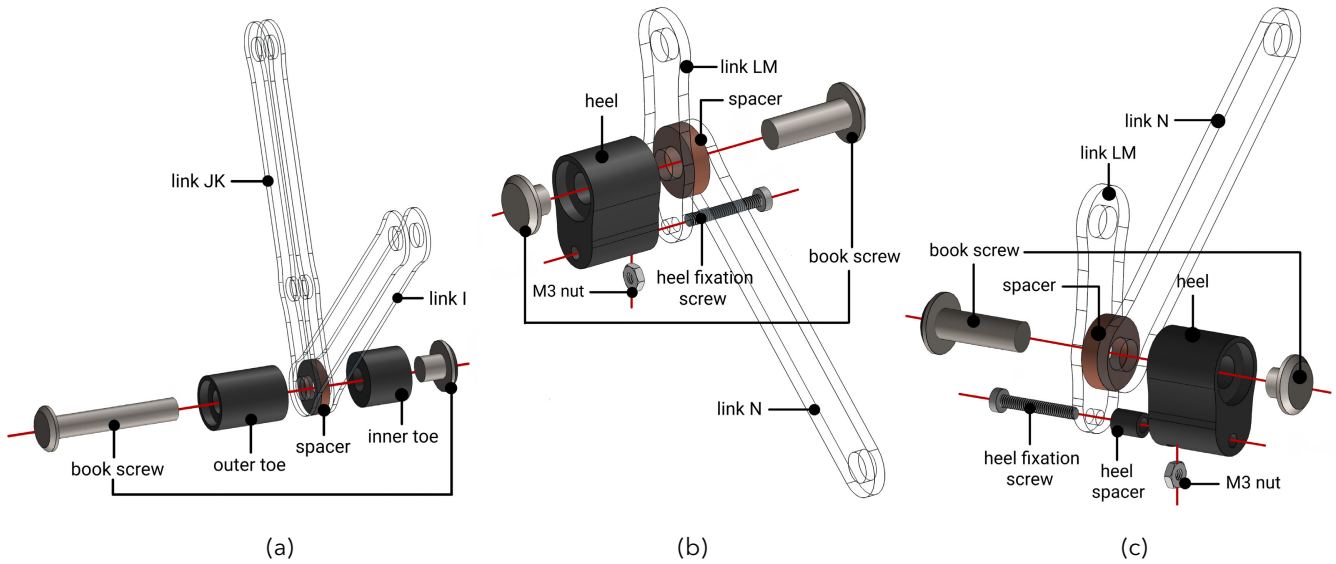
Figure C.9: Exploded views of the foot design, in which (a) the exploded view of the foot design of the toe; (b) the exploded view of the foot design of the inner leg heels; and (c) the exploded view of the foot design of the outer leg heels.

C.3   Motor torque MATLAB script

```matlab
%% Total Motor Torque Calculation %% ---------------------------------------------
%% Parameters %% -------------------------------------------------------------
m_ev = 6; % Predicted total mass, incl. payload and excl. legs [kg]
p = 1.21; % Air density [kg/m2]
g = 9.81; % Gravitational constant [m/s2]
Cd = 1.05; % Air drag coefficient [-]
v = 0.6; % Maximum speed [m/s]
u_k = 0.261; % Kinetic friction coefficient [-]
theta = deg2rad(28); % Maximum climbing slope [rad]
WC_width = 0.233; % EPWW widht [m]
S_height = 0.173; % Chair height [m]
B_height = 0.140; % Body/chassis height [m]
% Surface area: simplified to rectangle [m2]
Af = WC_width*(S_height+B_height);

%% Traction Force %% ---------------------------------------------------------
Fg = m_ev*g*sin(theta); % Force due to gravity [N]
Fsurf = u_k*m_ev*g*cos(theta); % Force due to surface resistance [N]
Fair = 0.5*p*Cd*v^2; % Force due to air drag resistance [N]
% total traction force [N]
Ft = Fg + Fsurf + Fair;

%% Torque Motor %% -----------------------------------------------------------
r = 34*10^-3; % Lenght of the crank, Trotbot leg mechanism [m]
% Assume 1 actuator only needs to subject to half of the traction force [N]
Traction_torque = r*0.5*Ft;
% Torque due to mass and inertia of leg mechanism [Nm]
max_torque_leg_sam = 0.116; % Determined via SAM Artas
% Total motor torque [Nm]
M_torque = Traction_torque + max_torque_leg_sam %Nm
```

Appendix D Prototyping
D.1   Final prototype

Figure D.1: Front view of the OctoWalker.

Figure D.2: Side view of the OctoWalker.

Figure D.3: Back view of the OctoWalker with joystick attached to chair using velcro.

Figure D.4: Back view of the OctoWalker with the joystick de-attached from the chair.

Figure D.5: The switch box and control box of the OctoWalker.

Figure D.6: The belt tensioner of the OctoWalker.
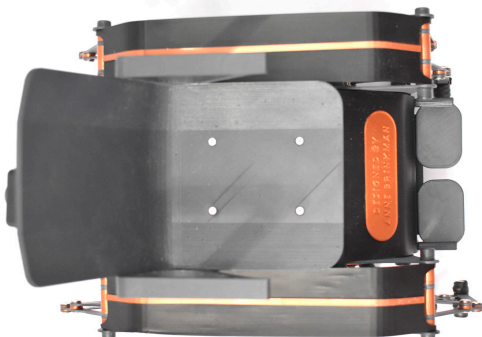
Figure D.7: Top view of the OctoWalker with mudguards.
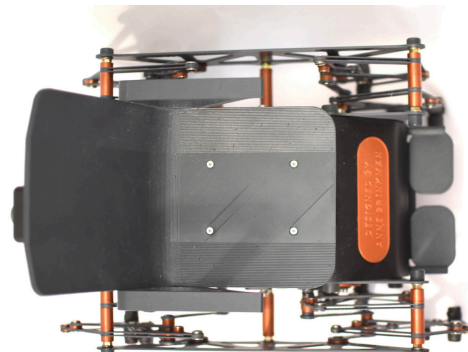
Figure D.8: Top view of the OctoWalker without mudguards.

D.2   Arduino code

```cpp
#include "CytronMotorDriver.h"

// Configure the motor driver.
CytronMD motor1(PWM_DIR, 6, 7);   // PWM 1A = Pin 6, DIR 1B = Pin 7. front
CytronMD motor2(PWM_DIR, 3, 4); // PWM 2A = Pin 3, DIR 2B = Pin 4. back

// Variables
float vmax = 255; // maximum speed (PWM signal)
float vmin = 150; // maximum speed (PWM signal)
float a1 = 1; // minimum variable smooth turn
float a2 = 0.75; // maximum variable smooth turn
float j1 = 400; // Y positive minimum
float j2 = 500; // X negative minimum
float j3 = 700; // X positive minimum
float j4 = 150; // Y positive maximum
float j5 = 220; // X negative maximum
float j6 = 600; // Y negative minimum
float j7 = 980; // X positive maximum
float j8 = 890; // Y negative maximum

// The setup routine runs once when you press reset.
void setup() {
}

// The loop routine runs over and over again forever.
void loop() {
  int xAxis = analogRead(A0); // Read Joysticks X-axis
  int yAxis = analogRead(A1); // Read Joysticks Y-axis

  // 1) Y-axis forward -----------------------------------
  if (yAxis < j1 && xAxis > j2 && xAxis < j3){
  motor1.setSpeed(map(yAxis,j1,j4,-vmin,-vmax));
  motor2.setSpeed(map(yAxis,j1,j4,-vmin,-vmax));
  }

  // 2) Y-axis forward left ------------------------------
  else if (yAxis < j1 && xAxis < j2){
   // speed motor 1 decreases or increases due to change in X-axis
  int DF = map(xAxis, j2, j5, -a1*vmax, -a2*vmax);
  motor1.setSpeed(map(yAxis,j1,j4,-vmin,DF));
  motor2.setSpeed(map(yAxis,j1,j4,-vmin,-vmax));
  }

  // 3) X-axis forward spin left -------------------------
  else if (xAxis < j2 && yAxis > j1 && yAxis < j6){
  motor1.setSpeed(map(xAxis,j2,j5,vmin,vmax));
  motor2.setSpeed(map(xAxis,j2,j5,-vmin,-vmax));
  }

  // 4) Y-axis forward right -----------------------------
  else if (yAxis < j1 && xAxis > j3){
  int DF = map(xAxis, j3, j7, -a1*vmax, -a2*vmax);
   // speed motor 2 decreases or increases due to change in X-axis
  motor1.setSpeed(map(yAxis,j1,j4,-vmin,-vmax));
  motor2.setSpeed(map(yAxis,j1,j4,-vmin, DF));
  }
```

```
// 5) X-axis forward spin rechts -----------------------------------
else if (xAxis > j3 && yAxis > j1 && yAxis < j6){
motor1.setSpeed(map(xAxis,j3,j7,-vmin,-vmax));
motor2.setSpeed(map(xAxis,j3,j7,vmin,vmax));
}

// 6) Y-axis backward -----------------------------------
else if (yAxis > j6 && xAxis > j2 && xAxis < j3){
motor1.setSpeed(map(yAxis,j6,j8,vmin,vmax));
motor2.setSpeed(map(yAxis,j6,j8,vmin,vmax));
}

// 7) Y-axis backward left -----------------------------------
else if (yAxis > j3 && xAxis < j2){
int DF = map(xAxis, j2, j5, a1*vmax, a2*vmax);
  // speed motor 1 decreases or increases due to change in X-axis
motor1.setSpeed(map(yAxis,j3,j8,vmin,DF));
motor2.setSpeed(map(yAxis,j3,j8,vmin,vmax));
}

// 8) Y-axis backward right -----------------------------------
else if (yAxis > j3 && xAxis > j3){
int DF = map(xAxis, j3, j7, a1*vmax, a2*vmax);
  // speed motor 2 decreases or increases due to change in X-axis
motor1.setSpeed(map(yAxis,j3,j8,vmin,vmax));
motor2.setSpeed(map(yAxis,j3,j8,vmin,DF));
}

else {
motor1.setSpeed(0);
motor2.setSpeed(0);
}
}
```

Appendix E Evaluation results
E.1   Test 1: Static walking
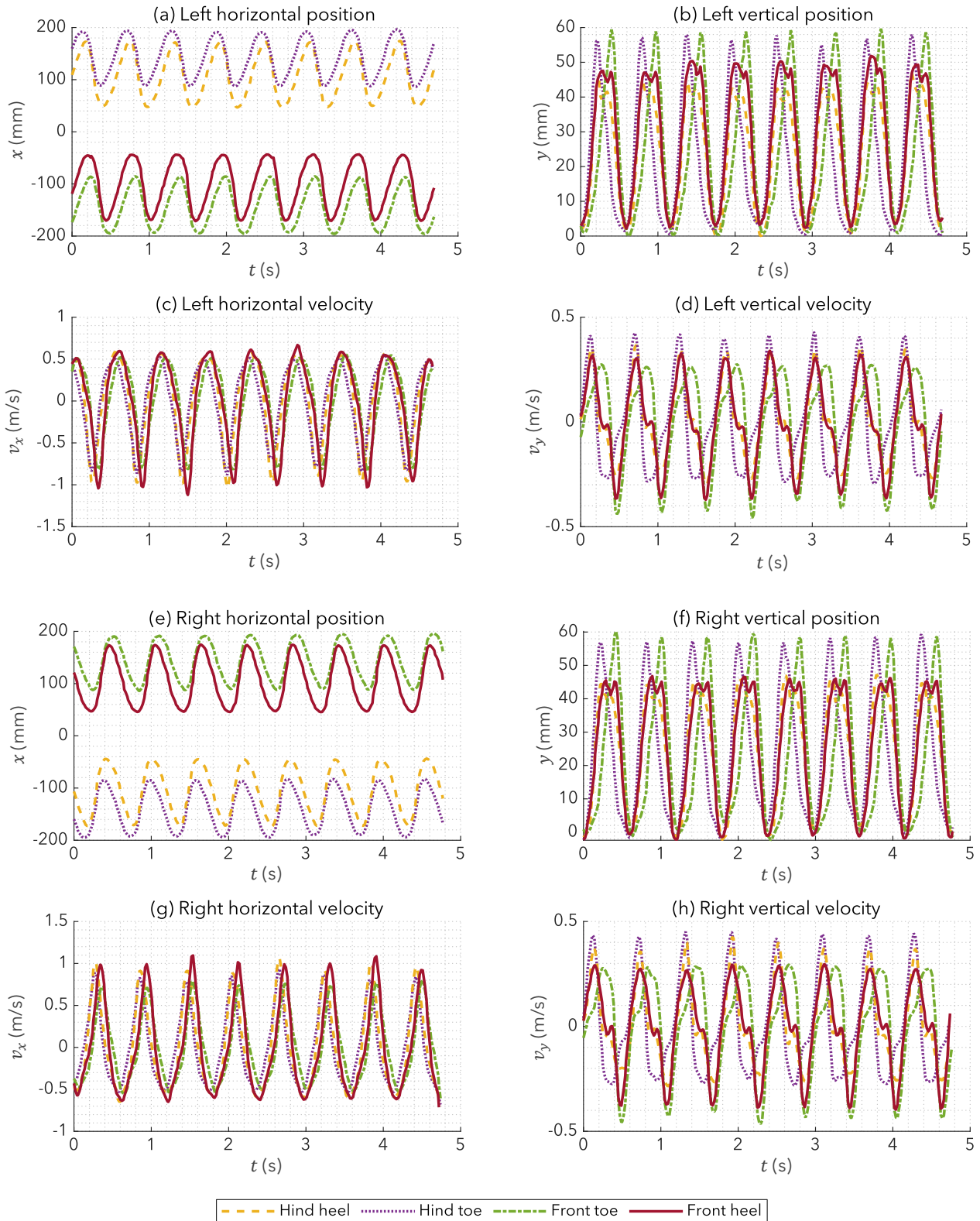
Figure E.1: Foot trajectory and velocity results of the static walking test (T1) of the outer hind heel, hind toe, front toe and front heel with respect to time; with (a)-(d) describing the results of the left side of the OctoWalker; and (e)-(h) describing the results of the right side of the OctoWalker.
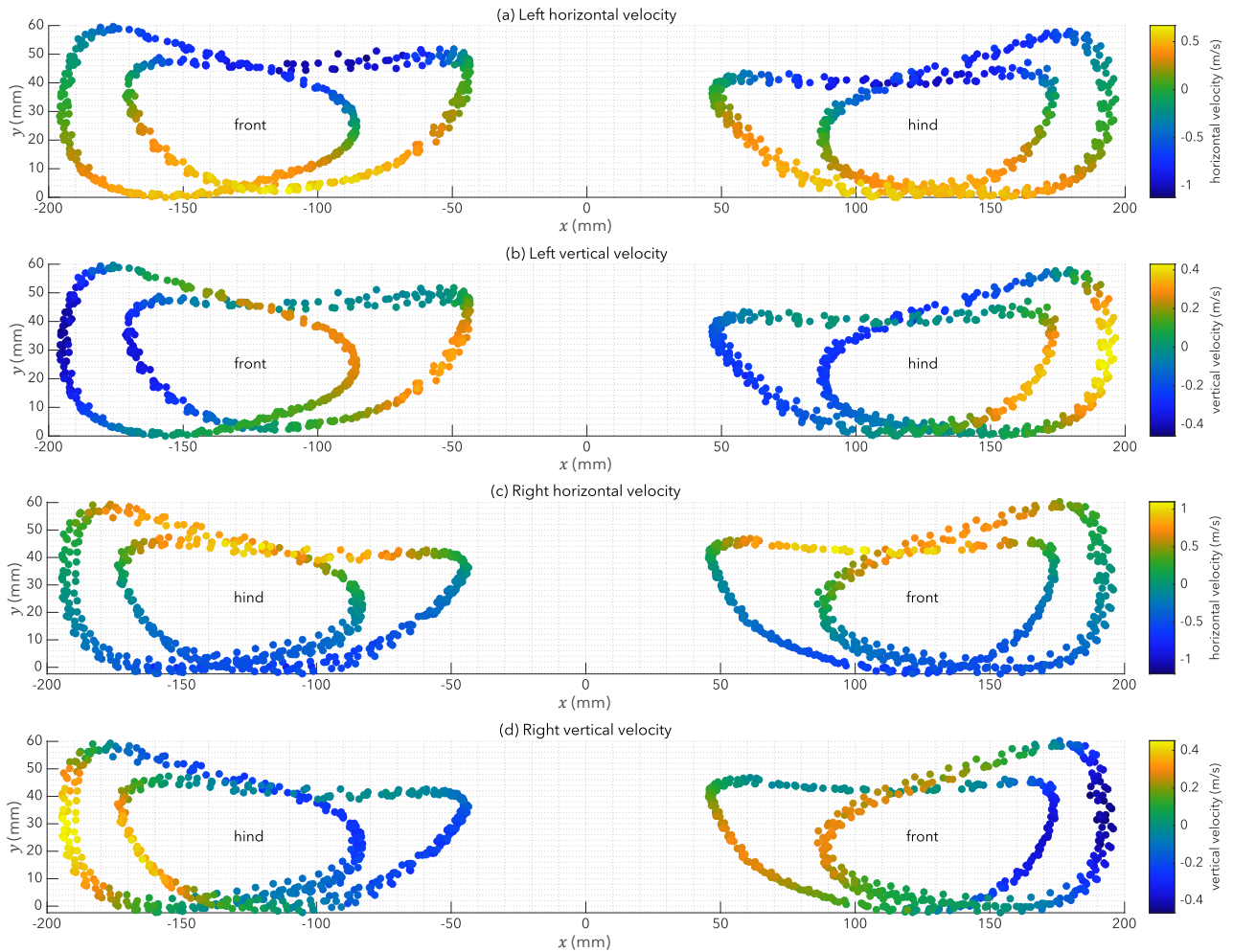
Figure E.2: Horizontal and vertical velocity results of the static walking test (T1) with respect to the feet positions; with (a) and (b) the left outer feet of the OctoWalker; (c) and (d) the right outer feet of the OctoWalker.

E.2   Test 2: Straight unloaded walking
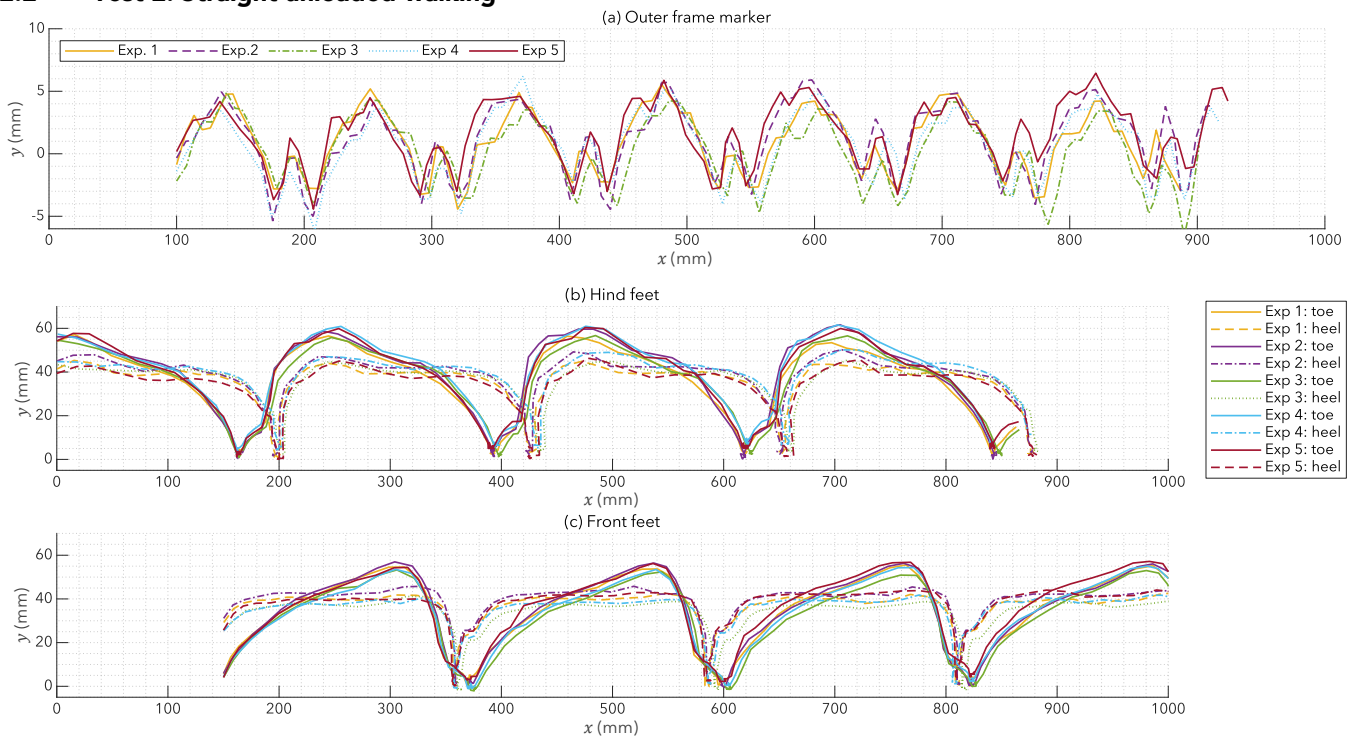
Figure E.3: Trajectory results of (a) the right outer frame marker, (b) hind feet and (c) front feet of the straight unloaded walking test (T2), in which all the results of all the five individual cycles are shown.
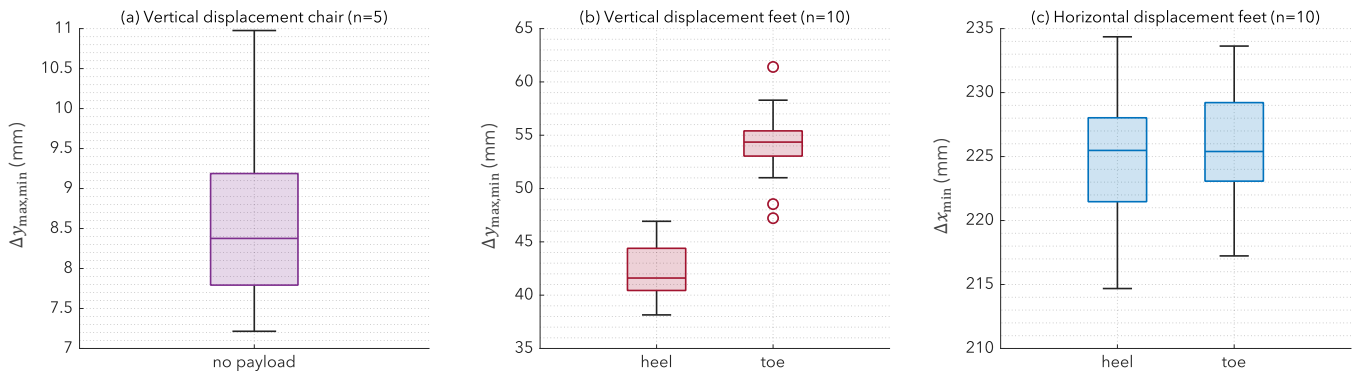
Figure E.4: Boxplot results of the straight unloaded walking test (T2), with (a) the right outer frame vertical displacement; (b) right heel and toe step height; (c) right heel and toe step length results of all the five cycles combined. In (b) and (c) the front and hind feet results were also combined.
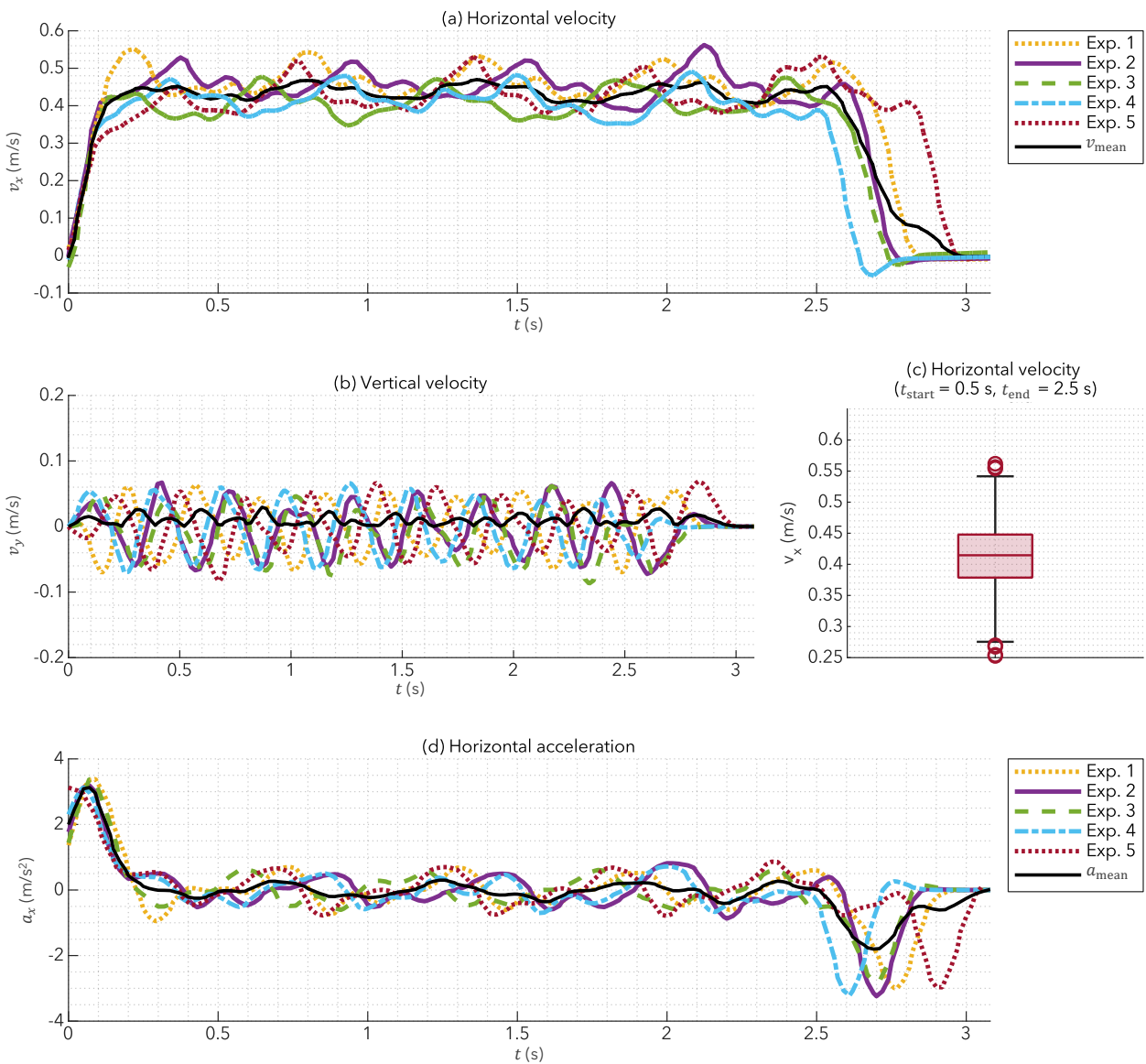
Figure E.5: (a) Horizontal velocity, (b) vertical velocity, (c) constant horizontal velocity and (d) horizontal acceleration results of the straight unloaded walking test (T2) of all the individual five cycles and the mean of all the five cycles combined (exp. 1-5).

E.3   Test 3: Steering
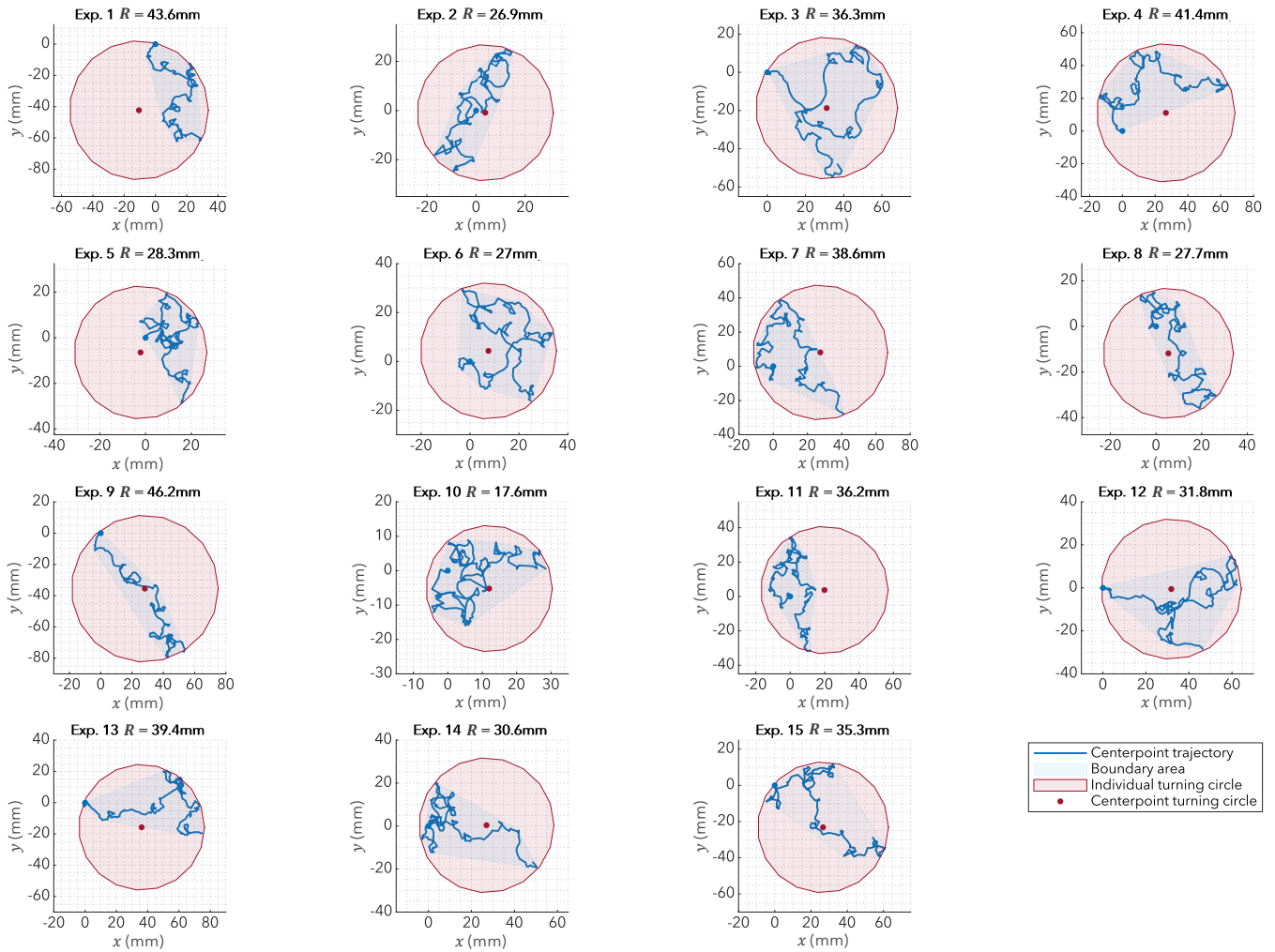
Figure E.6: Left steering results of the steering test (T3) of the maximum turning circle, turning radius (R) and center point of the turning circle results of all the 15 individual cycles, which all start at (0 mm, 0 mm).
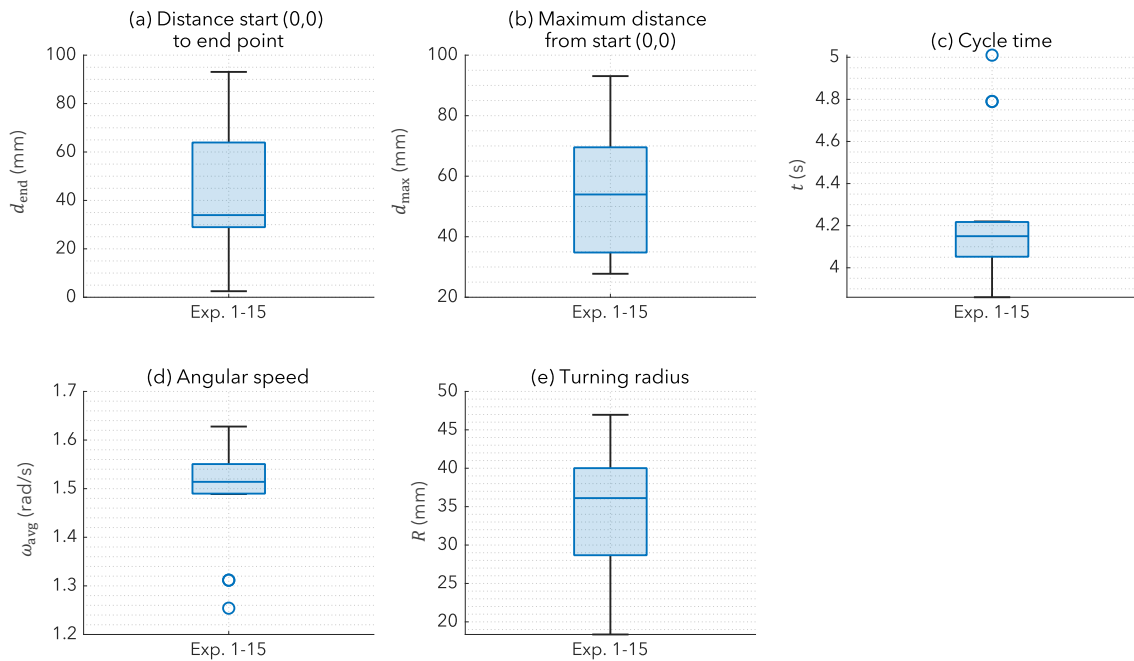
Figure E.7: Left steering boxplot results of the steering test (T3) of (a) the distance between the starting point (0,0) to the end point; (b) the maximum distance from the starting point; (c) the cycle time for one rotation; (d) mean angular speed and (e) the turning radii of all the 15 individual cycle results.
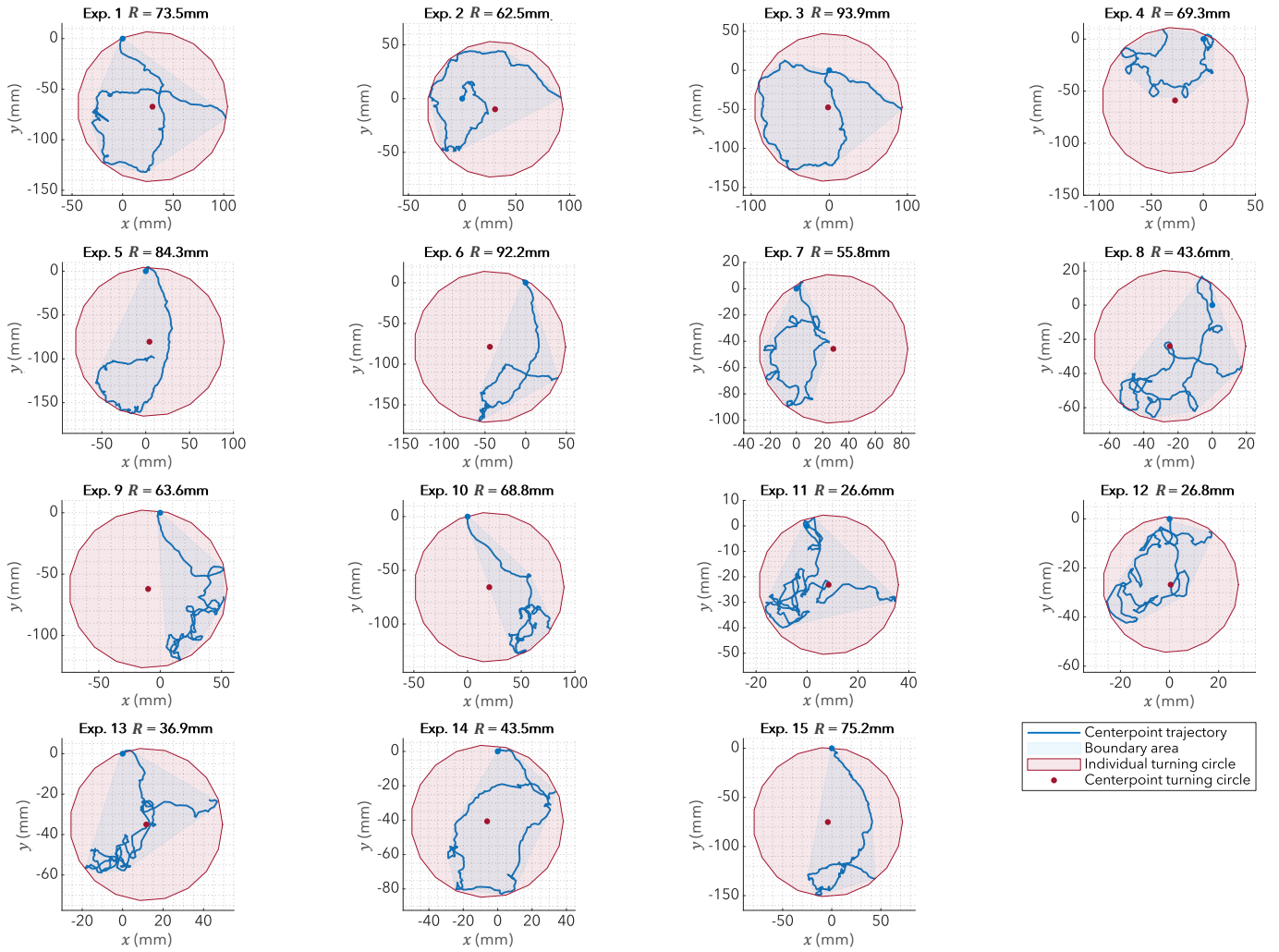
Figure E.8: Right steering results of the steering test (T3) of the maximum turning circle, turning radius (R) and center point of the turning circle results of all the 15 individual cycles, which all start at (0 mm, 0 mm).
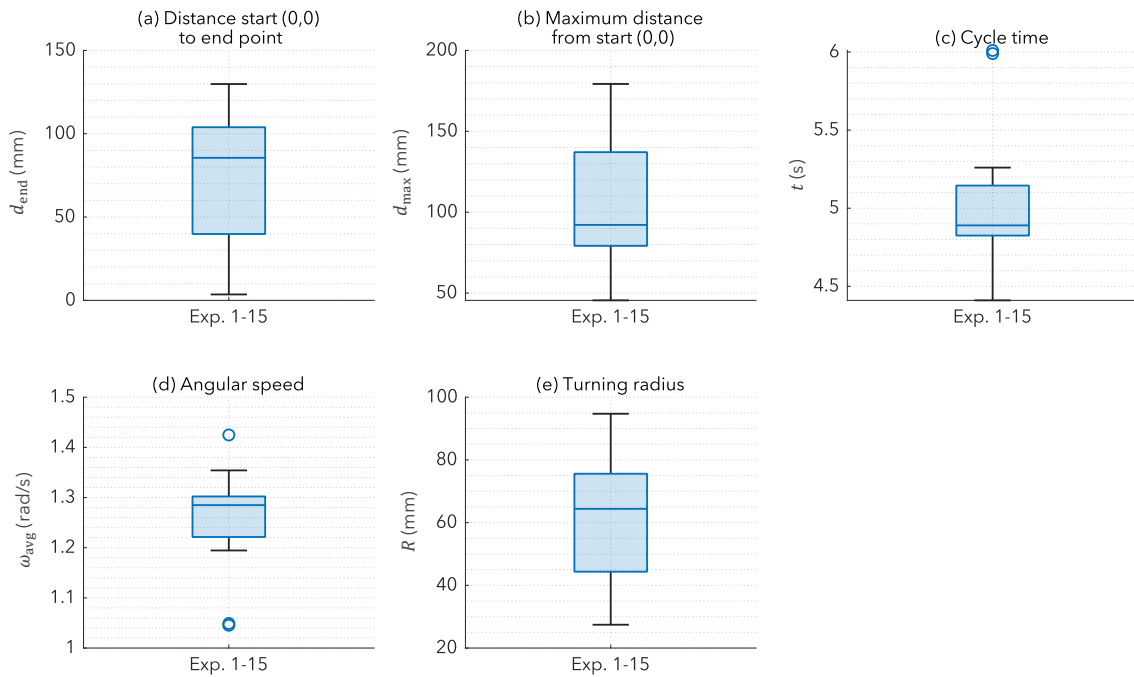
Figure E.9: Right steering boxplot results of the steering test (T3) of (a) the distance between the starting point (0,0) to the end point; (b) the maximum distance from the starting point; (c) the cycle time for one rotation; (d) mean angular speed and (e) the turning radii of all the 15 individual cycle results.

E.4   Test 4: Payload
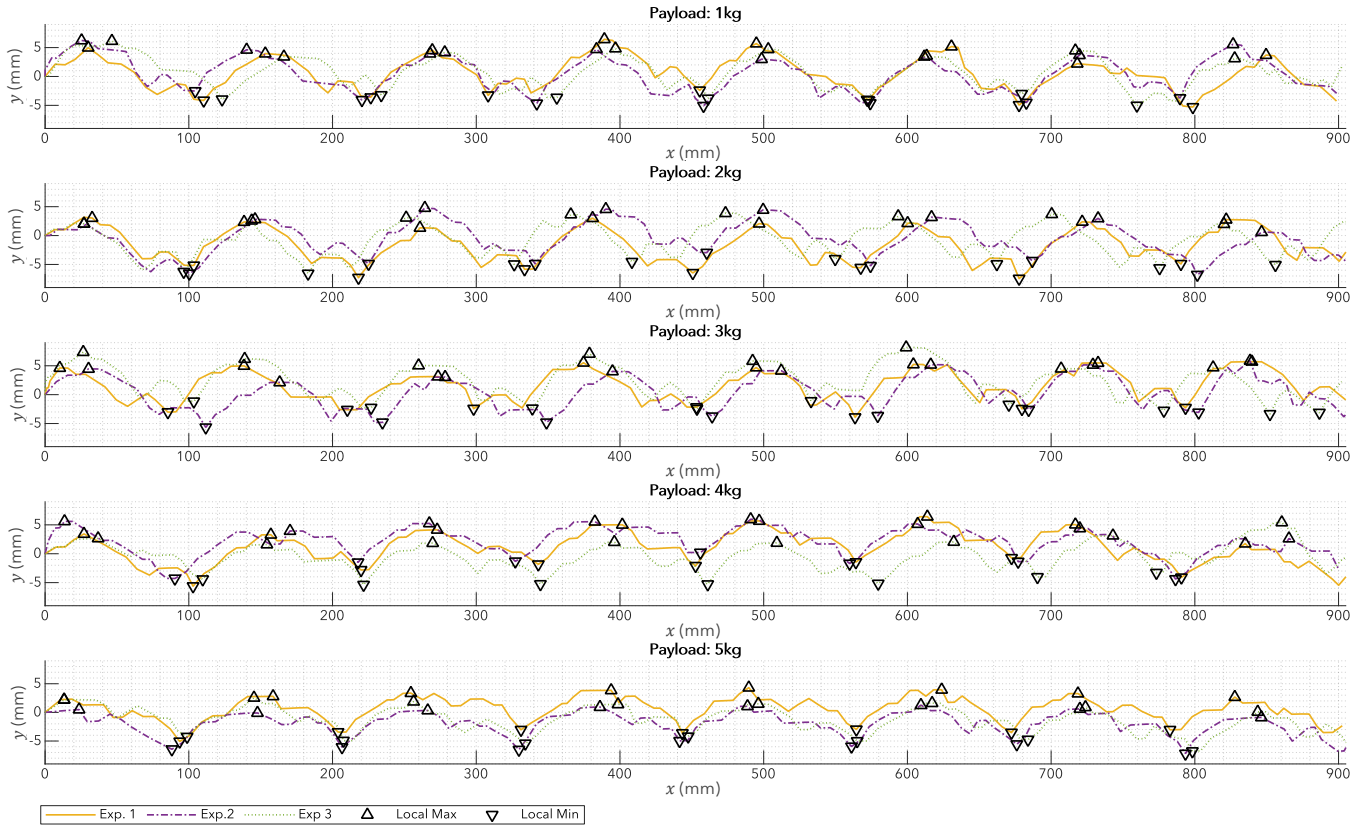
Figure E.10: The position results of the payload test (T4) with vertical fluctuations of the right outer frame marker at each payload.
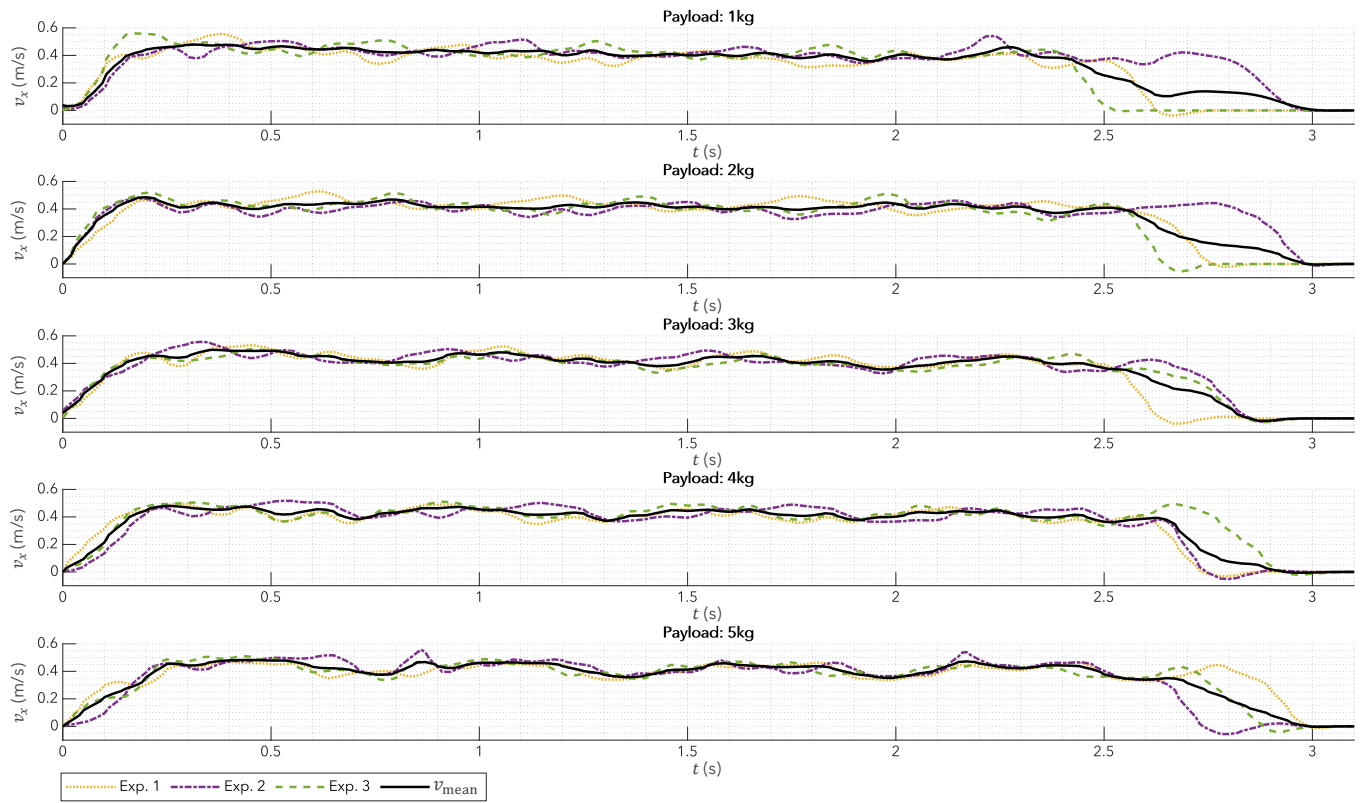
Figure E.11: The horizontal velocity results of the payload test (T4) of the right outer frame marker at each payload.